

---

# Nanometer scale description of electron transport and damage in condensed media using the TRAX Monte Carlo Code

---

**Beschreibung von Elektronentransport und resultierenden Schäden in Festkörpern auf Nanometerskalen mit Hilfe des Monte Carlo Codes TRAX**

Zur Erlangung des Grades eines Doktors der Naturwissenschaften (Dr. rer. nat.)

genehmigte Dissertation von M.Sc. Cathrin Gabriele Wälzlein aus Hanau

2014 — Darmstadt — D 17



TECHNISCHE  
UNIVERSITÄT  
DARMSTADT

Fachbereich Physik  
GSI Biophysik

---

Nanometer scale description of electron transport and damage in condensed media using the TRAX Monte Carlo Code

Beschreibung von Elektronentransport und resultierenden Schäden in Festkörpern auf Nanometerskalen mit Hilfe des Monte Carlo Codes TRAX

Vom Fachbereich Physik zur Erlangung des akademischen Grades Dr. rer. nat genehmigte  
Dissertation von M.Sc. Cathrin Gabriele Wälzlein aus Hanau

1. Gutachten: Prof. Dr. Marco Durante
2. Gutachten: Prof. Dr. Barbara Drossel

Tag der Einreichung: 15.10.2013

Tag der Prüfung: 16.12.2013

Erscheinungsjahr: 2014

Darmstadt - D17

---

---

# Contents

<b>Abstract / Zusammenfassung</b>	<b>5</b>
<b>1 Introduction</b>	<b>7</b>
<b>2 Motivation</b>	<b>9</b>
2.1 Radiation transport in solids . . . . .	9
2.2 Microscopic radiation damage . . . . .	10
2.3 Metallic nanoparticles in combination with particle therapy . . . . .	12
<b>3 Computational methods to describe radiation transport and damage</b>	<b>13</b>
3.1 Track structure Monte Carlo simulations . . . . .	13
<b>4 Extensions of the TRAX Code</b>	<b>17</b>
4.1 TRAX . . . . .	17
4.2 Cross sections for ion and electron interactions with matter . . . . .	18
4.2.1 Electronic excitation . . . . .	19
4.2.1.1 Carbon targets . . . . .	21
4.2.1.2 Various metallic targets . . . . .	24
4.2.1.3 Gold targets . . . . .	31
4.2.1.4 Water . . . . .	33
4.2.2 Plasmon excitation . . . . .	34
4.2.3 Ionization . . . . .	38
4.2.4 Elastic scattering . . . . .	46
4.3 Auger electrons . . . . .	54
4.4 Non-uniform targets . . . . .	57
<b>5 Simulations of Microscopic Radiation Transport</b>	<b>59</b>
5.1 Simulations to validate TRAX input . . . . .	59
5.1.1 Stopping Power . . . . .	60
5.1.2 Electron backscattering coefficients . . . . .	65
5.1.2.1 Backscattering from non-uniform targets . . . . .	70
5.1.3 Electron transmission . . . . .	73
5.2 Simulations for the Toroid experiment . . . . .	74
5.2.1 Electron yields and transmission spectra . . . . .	75
5.2.2 Electron stopping powers . . . . .	79
5.2.3 Secondary electron creation and Auger electrons . . . . .	80
5.2.4 Range of Auger electrons . . . . .	83
5.2.5 Electron emission cross sections for carbon projectiles . . . . .	88

---

<b>6</b>	<b>Microscopic radiation damage</b>	<b>93</b>
6.1	Choice of $r_{min}$ . . . . .	93
6.2	Elastic Scattering of Ions . . . . .	94
6.2.1	Validation simulations . . . . .	95
6.2.2	Effect on radial dose distribution . . . . .	99
6.3	Discrete interaction distances . . . . .	101
6.4	Gaussian diffusion of radicals . . . . .	102
6.5	Cut-off energy dependence . . . . .	104
6.6	Impact on RBE . . . . .	107
<b>7</b>	<b>Simulations on metallic nanoparticles</b>	<b>111</b>
7.1	Auger electron energy distributions . . . . .	112
7.2	Secondary electron spectra outside the NP . . . . .	114
7.3	Radial dose distributions . . . . .	114
7.4	Protons versus electrons . . . . .	115
<b>8</b>	<b>Summary and Outlook</b>	<b>123</b>
8.1	Description of radiation transport . . . . .	123
8.2	Microscopic damage . . . . .	124
8.3	Metallic nanoparticles in combination with ion beam radiotherapy . . . . .	125
<b>9</b>	<b>Appendix</b>	<b>127</b>
9.1	Radial dose calculations for TLDs . . . . .	127
9.1.1	Fluoride . . . . .	130
9.1.2	Lithiumfluoride . . . . .	131
9.1.3	Radial dose calculations . . . . .	132
9.2	Complete sets of electron cross sections . . . . .	133

---

---

# Glossary

BEA	Binary Encounter Approximation
BEB	binary-encounter-Bethe
BED	binary-encounter-dipole
DDCS	double-differential cross section
DNA	deoxyribonucleic acid
ELF	Energy Loss Function
FBA	First Born Approximation
LEM	Local Effect Model
LET	linear energy transfer
MC	Monte Carlo
MFP	mean free path
NP	nanoparticle
OOs	optical oscillator strengths
PWA	partial wave analysis
RBE	relative biological effectiveness
SDCS	single differential cross section
SRCS	screened Rutherford cross sections
TCS	total cross section
TLD	thermoluminescence dosimeter
TPS	treatment planning system



---

## Abstract

The single interaction Monte Carlo code TRAX has been extended to describe low-energy electron creation and transport in solids. Electrons with energies below 1 keV have ranges in solids on the nanometerscale. Complete sets of electron interaction cross sections for energies below 1 keV down to 1 eV have been compiled and assessed for various target materials. The applicability of the cross sections has been validated by comparisons with experimental data as far as available. The code has further been extended to handle the production of Auger electrons and cascades. Furthermore, the capability to handle non-uniform targets has been added. With the extended TRAX code, experimental data from GSI's Toroid electron spectrometer have been reproduced using thin solid state foils of carbon, nickel, silver and gold as targets. Furthermore, the radial dose distribution around ion tracks has been investigated on the nanometer scale. The explicit consideration of Auger electron cascades has been used to evaluate whether metallic nanoparticles can locally enhance the dose in combination with proton or electron irradiation.

## Zusammenfassung

Der Monte Carlo Code TRAX, der auf der Simulation von einzelnen Interaktionen basiert, wurde erweitert, um die Erzeugung und den Transport von niederenergetischen Elektronen in Festkörpern zu beschreiben. Die Reichweite von Elektronen mit Energien unterhalb 1 keV liegt auf der Nanometerskala. Es wurden komplette Sammlungen von Wirkungsquerschnitten für Elektronen mit Energien unterhalb 1 keV, bis hin zu 1 eV, für verschiedenste Target Materialien zusammengetragen und beurteilt. Die Anwendbarkeit und Gültigkeit der Wirkungsquerschnitte wurde anhand von experimentellen Daten überprüft, sofern vorhanden. Der Code wurde zudem im Hinblick auf die Erzeugung von Augerelektronen und -Kaskaden erweitert. Weiterhin wurde die Berücksichtigung inhomogener Targets ermöglicht. Mit Hilfe des erweiterten TRAX Codes konnten Daten des Toroid-Elektronenspektrometers der GSI reproduziert werden, bei dem als Targets dünne Festkörperfolien aus Kohlenstoff, Nickel, Silber und Gold verwendet wurden. Weiterhin wurde die Radialdosis um eine Teilchenspur auf der Nanometerskala berechnet. Die Berücksichtigung von Augerelektronen-Kaskaden ermöglichte es zu untersuchen, ob metallische Nanopartikel in Kombination mit Protonen- oder Elektronenbestrahlung zu einer lokalen Dosiserhöhung führen können.





---

# 1 Introduction

Radiotherapy with swift light ions (protons and/or carbon) is one of the most promising approaches for cancer treatment. This method offers significant physical and radiobiological advantages compared with conventional photon therapy. It allows to deliver a high dose to the target volume while the exposure of healthy tissue can be kept to a minimum [Schardt2010]. By now, about 30 clinical sites around the world apply ion beams for the purpose of radiotherapy. Several more are planned or already under construction. Treatment planning systems (TPS), such as GSI's TRiP98 [Kraemer2000, KrSch2000] are used to obtain acceptable patient treatment plans. Although they have been used clinically as well as for research purposes for the past 15 years, several open problems still exist. One of the most challenging problems in ion beam radiotherapy is an accurate description of the relative biological effectiveness (RBE) of ion irradiation. The RBE depends on a large variety of parameters like the type and energy of the particle as well as the irradiated cell type and its radiosensitivity. To predict the biological effectiveness in radiotherapy with ion beams, the microscopic damage from ion irradiation is of particular importance [LoDu2013].

The description of microscopic damage from ion or electron irradiation is directly linked to the generation and transport of secondary electrons with low energies. When passing matter, ions transfer a huge amount of their energy to secondary electrons. Considering the total energy deposition of ions, about two thirds of the ion energy is not directly deposited but transferred into kinetic energy of released electrons [Paretzke1988, Bethe1930]. Most of these electrons have energies below 1 keV and the yields are increasing for lower electron energies. The mean kinetic energy of created secondary electrons is on the order of 100 eV [KrKr1994]. Electrons with energies from 1 keV down to a few electron Volts are stopped inside a liquid or solid material after a travelling length of a few nanometers. Depositing all their energy within a small volume results in a high local damage. Detailed knowledge about the interactions of these low-energy electrons is necessary to explain radiation action at the micrometer or even nanometer scale providing important insights into the basic nature of radiation action at a very low level. This thesis is focussed on improvements in the description of low-energy electron interactions.

To predict biological effects due to particle irradiation, a radial dose is evaluated inside water, which serves as a tissue equivalent material. The Local Effect Model (LEM) [SchKr1997, SchKr2004] allows to describe the RBE for usage in commercial as well as research treatment planning systems. The radial dose is used as an input parameter for radiobiological modelling and relies on an accurate description of the track core, where local doses are highest. LEM uses radial dose profiles relying on amorphous track structure to calculate RBE factors. The predictions of the biological model might benefit from improvements in the physical input data. Microscopic dose distributions with more physical details, in particular at nanometer distances from the ion path could change resulting RBE values as the model is highly sensitive to that region.

The radial dose distribution can further be used to estimate the possible effectiveness of metallic nanoparticles (NPs) which have raised recent interest as it has been shown that they can increase cell killing while acting as dose enhancers in combination with photon irradiation for

---

radiotherapy [Hainfeld2004, Hainfeld2008]. High energetic X-rays can be absorbed by gold NPs and enhance the dose in a small local volume around the NP through absorption and subsequent emission of Auger electrons. The effect is expected to be smaller for ion beam irradiation, but so far only a few experiments [Polf2011] have been performed. Evaluations concerning the portion of damage related to Auger electron creation could provide further insight if NPs have the potential to act as dose enhancer in combination with ion beam irradiation.

Furthermore, detailed track structure description is important for dosimetry, as it allows the calculation of condensed phase detector responses with an approach similar to RBE estimations. Detection systems such as thermoluminescent dosimeters (TLDs) [Horowitz1984, Geiss1999] and radiographic films [Spielberger2002] are commonly used due to their high spatial resolution and non-disturbance of the radiation field. These devices are susceptible to the high dose levels found in the track core as the dose response usually saturates at doses of a few gray up to a few thousand gray. To describe their nonlinear response, a radial dose distribution on the nanometer scale is necessary.

---

---

## 2 Motivation

---

### 2.1 Radiation transport in solids

---

One of the aims of this thesis is an improved description of low-energy electron creation and transport in solids. A correct description is a necessary prerequisite to describe microscopic damage. Measurements using solid state targets are difficult to perform and to analyze. In contrast to experiments using gaseous targets, single collision conditions are not fulfilled. Secondary electron spectra show the energetic and/or angular distribution of electrons after ions or electrons have travelled through a target with a certain thickness, suffering several collisions. These collisions can be elastic (without energy losses) or inelastic (leading to energy losses). Secondary electron energy spectra can be used as benchmarks for the combined description of electron creation and transport.

Secondary electron spectra from solid state targets of a few nanometer thickness have been measured in experiments using GSI's Toroid spectrometer [Lineva2008, Lineva2009]. These experiments are unique as it has been possible to measure low energy (50 eV-1 keV) electron creation and transport systematically in solid state targets. Experimental data on electrons in that energy range are extremely scarce and especially for solids in which nanometer distances are hard to measure. Further details about the Toroid experiments are given in section 5.2. Within the framework of this thesis, one major goal has been a better understanding of the Toroid experiments through improved calculations to reproduce experimental data. Special focus has been given on the description of electron creation and transport in carbon, nickel, silver and gold, target materials which have been used in the Toroid experiments.

In the framework of the Toroid experiments, it has been intended to use Auger electrons as probes to study electron emission from inside as they are produced in ionization processes with discrete energies and emitted isotropically. Auger electrons contribute significantly to secondary electron yields at low energies which is why they have to be considered for nanoscale calculation. In secondary electron energy spectra Auger electrons can be observed as a peak with a sharp edge at the initial Auger electron energy and a tail towards lower energies. The tail is stemming from Auger electrons which have lost already a part of their energy in collisions inside the target. Detailed evaluations of creation and transport of Auger electrons are necessary for the Toroid experiments as their range is smaller than the used target thicknesses. Many Auger electrons have been absorbed already inside the targets and most detected Auger electrons were stemming from the target surfaces.

Furthermore, the Toroid experiments have shown that thin solid state targets can be non-uniform which affects the secondary electron spectra significantly. This aspect has to be considered in the description of radiation transport in solids.

---

## 2.2 Microscopic radiation damage

---

Being able to handle low-energy electron creation and transport allows to calculate microscopic damage on the nanometer scale. A common quantity to describe the microscopic damage of ion- or electron irradiation is the radial dose distribution. Ions and electrons do not deposit their energy homogeneously inside the medium. In contrast, photons show an almost uniform distribution of interaction events on the nanometer scale. Low-energy electrons contribute most to local radiation damage in solid and liquid state targets due to their range in the micrometer or nanometer scale. Radiation transport of charged particles and the resulting damage is of interest for several applications ranging from biological damage relevant for particle therapy to detector efficiencies and radiation protection.

The formulation of the radial dose distribution was introduced by Butt, Katz, Kobetich and coworkers [BuKa1967, KoKa1968, KoKa1969]. The radial dose  $D(\mathbf{r})$  describes the deposited energy at a certain radial distance from the center of an ion track. It is defined as the average deposited energy per unit mass within a concentric cylindrical shell between the radii  $r$  and  $r+dr$ ,  $r$  being the radial distance from the path of the charged particle. See Fig. 2.1 for an illustration.

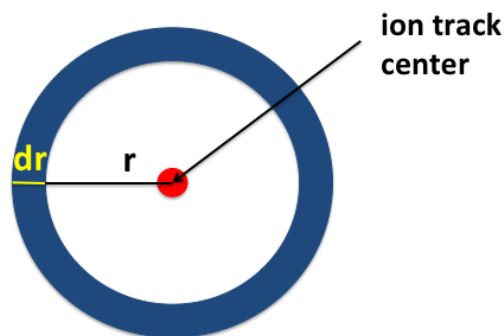


**Figure 2.1:** A cylindrical shell with radial distances from the center of the ion track between  $r$  and  $r+dr$ . In this shell, the radial dose  $D(r)$  is defined.

The radial dose is depending on the projectile (ion type and energy) as well as on the target material. Inelastic collisions like excitations and ionizations caused by the primary ions lead to dose depositions along the ion track at  $r=0$ . Secondary electrons deposit their energy farther away from the ion track core. The maximum radius, at which radial dose distributions are present, is limited by the maximum range of the secondary electrons. Usually, the track radius

---

---

increases with ion energy.

To obtain the radial dose distribution, one can distinguish between conceptual different approaches. It can be derived from analytical models, semi-empirical models, Monte Carlo (MC) simulations and experiments. All methods more or less agree in their results for intermediate radial distances. Differences can be observed at large radial distances as well as at radial distances below a few nanometers. Fig. 2.2 shows an evaluation for the radial dose of 2.57 MeV/u oxygen ions in H<sub>2</sub>O as an example to illustrate differences at small radii.

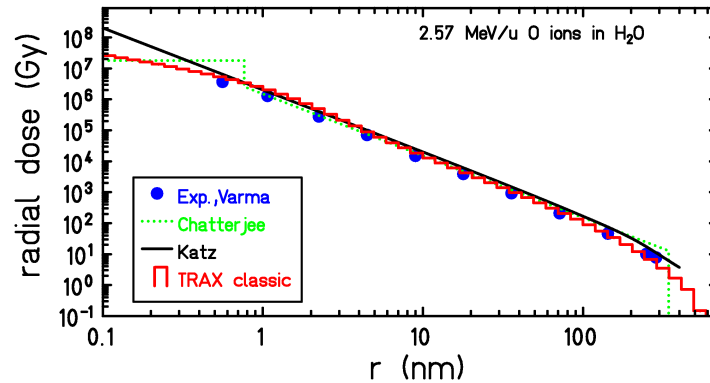


**Figure 2.2:** Radial dose distribution of 2.57 MeV/u oxygen ions in H<sub>2</sub>O evaluated by different methods. Experimental data [Varma1993] is shown with blue dots. Below a radius of about 1 nm, the results from different theoretical approaches differ. The black line shows analytical results according to [BuKa1967] and the dotted green line semi-empirical results according to [ChSch1976]. TRAX results are shown for the classic version of the TRAX Monte Carlo code.

In the analytical model of Katz et al. [BuKa1967], the radial dose is evaluated from a two body Coulomb interaction. Assumptions include no deflections of electrons, all electrons emitted perpendicular to the particle trajectory and a continuous slowing down of the projectile. The energy dependence of the electron range and therefore the resulting maximum radius, at which a radial dose is present, is approximated empirically. Assuming a constant energy loss for electrons leads to a linear dependency between electron energy and range. The dose is evaluated to be proportional to  $1/r^2$  up to a maximum range  $r_{max}$ ,  $r$  being the radial distance from the core of the ion track. The problem resulting from this approach is that the dose at  $r=0$  would be infinite, which is unphysical.

The semi-empirical core-penumbra model of Chatterjee et al. [ChSch1976, MaCh1979, ChHo1991] solves the problem of an infinite dose at  $r=0$  by introducing a core region in which the dose remains constant. A constant or energy dependent minimum cut-off radius  $r_{min}$  defines the core from  $r=0$  to  $r=r_{min}$ . Their assumption is that excitation events only occur inside a core around the ion track and lead to a locally high energy deposition. Ionizations on the other hand lead to the production of delta electrons which energy dissipated inside a track halo which is frequently called penumbra. The dose in the penumbra falls off with  $1/r^2$ . To calculate the dose inside the core, the energy is equally distributed between the core and the penumbra, having 50% of the total dose deposited in the core. Different variations of this models have either a constant core radius which is independent of the ion energy, or an energy-

---

---

dependent core size. In the case of an energy dependent core size, the diameters of core and penumbra increase with particle energies. The sizes of core and penumbra are based on empirical range relations. No details of elementary collision processes are considered.

The radial dose distribution can be obtained experimentally by measurements with gaseous targets. Usually the ionization current is measured within an ionization chamber which is filled with gas at a low pressure. The ionization currents are converted to dose values by multiplication with constant W-values. Radial dose values in tissue (or liquid water with  $\rho = 1\text{g/cm}^3$  as tissue equivalent material) can be calculated from the gaseous targets by density scaling. The procedure is explained in detail in a review article [Varma1989]. By variations of the gas pressure, the density changes and different measurement values for radial distances in tissue/liquid water can be achieved. Several experiments exist for radial dose measurements in gases. For solids, measured radial doses on the nanometer scale are not available.

Monte Carlo simulation codes can describe the tracks of ions and electrons and directly evaluate the radial dose distribution. The MC method is further described in chapter 3. Within this thesis, the TRAX MC code has been used to obtain a physically realistic description of the radial dose inside the track core. Details about TRAX are given in chapter 4. Calculations for the radial dose are presented in chapter 6.

---

### **2.3 Metallic nanoparticles in combination with particle therapy**

---

The goal of radiotherapy is to deliver a high dose to the tumour tissue while minimizing the dose delivered to the normal tissue. Metallic nanoparticles (NPs) are recently discussed as a possible dose enhancer. For gold NPs it has been shown that the approach works in combination with photon radiotherapy [Hainfeld2004, Hainfeld2008]. The effect is enhanced due to the selective uptake of NPs by tumour cells which can be much larger than for normal tissue. Energetic X-rays can be absorbed by the gold NPs and lead to subsequent emission of low-energy electrons which deposit their energy within a small volume around the NP, inducing a more complex biological damage, which is more difficult to repair. While an advantage of using gold NPs in combination with conventional photon radiotherapy in enhancing cell killing has been already proven [Hainfeld2008], and can be partially explained by microscopic mechanisms [McMahon2011], a benefit for ion or proton radiotherapy is not directly obvious. With ion beam irradiation the advantage of producing a large number of secondary electrons of low energies and therefore short ranges which lead to locally enhanced dose depositions is already given. Apart from a few experiments [Polf2011] the effect for ions has not yet been studied in detail. A recent computational study [Chow2012] for electron irradiation has not found a real benefit for electrons in combination with gold NPs. The most promising source for additional creation of secondary electrons are Auger cascades, which can be large in the case of high Z (atomic number) materials. On the other hand, dense materials with a high Z have also a high stopping power for low-energy electrons. So it has to be determined how many electrons which are created inside the NP actually escape and deposit their energy in the surrounding tissue. Besides gold, NPs made of Gd [Robar2002], Pt [Porcel2010, Usami2007] and Fe [Kim2012], respectively have also been discussed to be used in radiotherapy.

Calculations concerning the creation of secondary electrons in metallic nanoparticles have been performed in the framework of this thesis, including Auger electron cascades. Results for Auger electron yields and the radial dose around metallic NPs after proton or electron impact are presented in chapter 7. Further details about Auger electrons are given in section 4.3.

---

---

## 3 Computational methods to describe radiation transport and damage

Radiation transport of charged particles and the resulting damage can be described with Monte Carlo (MC) simulations as they can deal with the stochastic nature of electron interactions like electron emission and transport. The method has been described extensively in [Berger1963]. One has to distinguish between MC simulations relying on condensed history and track structure MC codes relying on the single interaction approach. The approach based on condensed random walk and multiple scattering is the basis for many conventional simulation packages as introduced in [Berger1963]. MC simulations based on the continuous slowing down approximation rely on stopping powers as input parameters to determine the energy losses of particles traversing matter and apply additional multiple scattering theories to obtain the angular distribution of projectiles after a certain travelling pathlength. In [Berger1963] the condensed history approach is favoured as to that time it was computationally not feasible to calculate all single interactions separately. He also claims that even though the number of collision is high, most of them will only lead to small energy losses and deflections [Berger1963]. He notices the limitations of this condensed history approach for the case of electron backscattering from foils [Berger1963].

However, codes relying on condensed histories are perfectly suited to describe radiation action at high energies and large scales but are inappropriate for calculations concerning low-energy electrons and the (sub) micrometer scale. The continuous slowing down approximation is only justified if the number of collision processes to stop a projectile is large. For low-energy electrons ( $E < 100$  eV), which might suffer only a few collisions, this is not the case. Therefore, to describe the tracks of electrons with energies of a few electron Volts, track structure MC simulations based on the single interaction approach, sampling each interaction individually, should be preferred. In a review article [Nikjoo2006], the differences between different types of MC simulations for radiation transport are discussed. Track structure codes are suited to investigate particle tracks of ionizing radiation for a huge variety of research fields. These include, e.g., space radiation and shielding, radiotherapy and biological modelling as well as solid state physics.

To evaluate the transport of ions and electrons in detail, cross sections are needed for basic interactions (elastic scattering, excitation and ionization) inside the target material. To provide further insights in the details of radiation action, shell-specific cross sections are needed for inelastic interactions like ionization and excitation.

---

### 3.1 Track structure Monte Carlo simulations

---

Monte Carlo (MC) track structure simulations provide a useful tool to describe the tracks of ions and electrons in various media [Nikjoo2006]. However, correct interaction cross sections are needed as input which are not easily accessible in the case of low energy projectiles. Most of the cross sections used for MC simulations are derived by combinations of experimental

---

data and model calculations as there is no model which could generate cross sections over the entire energy range starting from fundamental principles [Nikjoo2006]. Huge attention is given to describe cross sections for very low-energy electrons inside biological target materials like water and components of the DNA [Nikjoo2006, BoSa2002, BlGa2007, Dingfelder1999]. Biological damage is usually described considering water as a tissue-equivalent material and many codes exist to calculate radiation action in water down to very low energies like KURBUC [Uehara1993], PARTRAC [Friedland2003] and Geant4DNA [FrIn2011]. However, the situation is different for other target materials. Little knowledge exists about the interaction cross sections of low-energy electrons with energies below 1 keV. There is neither a comprehensive theory (free of any semi-empirical fitting parameters), nor there is a complete experimental database covering low-energy electron cross sections for all important interactions (elastic scattering, excitation and ionization) for a broad range of atomic or molecular target materials in a neutral charge state. Especially information about electronic excitation is extremely scarce. It is very difficult to measure electron excitation at low energies. Excitation channels can start at energies as low as a few electron Volts and below and there exist numerous different excitation channels which would be hard to distinguish.

Common theories describing the energy loss of electrons using the dielectric formalism [Lindhard1954, Hubbard1955] are only suitable for electron energies above 1 keV as they require the validity of the Born approximation [Penn1987]. Besides, calculations are based on experimentally obtained optical data (with zero momentum transfer) and have to be expanded for electron projectiles including momentum transfer. Another drawback of the dielectric formalism is, that the resulting cross sections are only given as total inelastic cross sections. No differentiation between shell-dependent ionization cross sections and channel-resolved excitations is provided.

Electrons in the energy range below a few 100 eV are of major importance in theoretical calculations as many secondary electrons are created at these energies. A correct description of their interactions leading to localized energy depositions is crucial. However, cross sections for this energy region remain very uncertain as there exists no model to explain deviations from the first Born approximations in a satisfactory way covering the whole range of energy loss and momentum transfer [Nikjoo2006].

Due to the limitation in cross sections, many track structure codes like PENELOPE [Salvat2003, Fernandez2012] or LEEPS [Fernandez1996] cannot perform calculations below a certain cut-off energy (50 eV or 100 eV or even higher for electrons). When the energy of electrons falls below a certain cut-off threshold they are usually removed from the calculation procedure. Setting the electron cut-off energy to values as high as 50 eV or even 100 eV neglects the ends of the electron tracks and therefore reduces the accuracy of simulation results on the nanometer scale. The cut-off energy should be set as low as possible, as long as reasonable cross sections are available.

Within this work, efforts were made to find reliable sets of cross sections for electron interactions at energies from 1 keV down to below 1-10 eV for several target materials of interest ranging from light materials as carbon to heavy materials like gold. Therefore, cut-off energy values for electrons could be set to values as low as a few electron Volts. These cross sections have been implemented to be used with the track structure MC code TRAX [KrKr1994, Kraemer1995, KrDu2010]. TRAX as a single-interaction track structure MC code provides a dedicated tool to describe the interaction of low-energy electrons on the micrometer or nanometer scale and is able to handle both electrons and ions as projectiles. Using

---



these low-energy electron cross sections with TRAX allows to follow electron transport and evaluate resulting damage down to the nanometer scale. The cross sections are presented in chapter 4. Simulations to validate their applicability are shown in chapter 5.

---

### Cross sections and the mean free path

---

Track structure MC simulations rely on total and differential cross sections for individual interactions as input parameters. To describe the transport of ions and electrons in matter, one has to know which interactions take place at which positions inside the target material. These interactions can be either elastic (with no energy loss) or inelastic (with energy loss of the projectile). In both kinds of scattering, the projectile can change its direction. Cross sections can be used to determine the tracks of the projectiles through the considered target as they provide a measure for the probability to undergo a certain type of collision. Interaction cross sections are strongly dependent on energy. The total interaction cross sections depend on the projectile type (electrons or ions (charge, mass)) and on the target material. For each interaction a cross section has to be provided. Cross sections can also have an angular dependency as well as a dependency on energy of a created secondary electron (released by ionization). Therefore, single differential cross sections (SDCS) or double differential cross sections (DDCS) can be needed. By integration, a total cross section (TCS) can be derived. In track structure MC codes, the track length for the next interaction is determined deriving a mean free path (MFP) from the given cross sections for a certain projectile energy. Each projectile is followed interaction by interaction. To determine the travelling length for the next interaction, cross sections for all possible interactions are summed to obtain a total interaction cross section:

$$\sigma_{\text{total}} = \sigma_{\text{elastic}} + \sigma_{\text{ionization}} + \sigma_{\text{excitation}} \quad (3.1)$$

The MFP  $\lambda$  is then derived using the total interaction cross section  $\sigma$  and the particle density  $n$  for a given target material:

$$\lambda = \frac{1}{n \cdot \sigma} \quad (3.2)$$

The particle density  $n$  and can be derived from the target material density  $\rho$  (in  $\text{g}/\text{cm}^3$ ) and the molar mass  $M_{\text{mol}}$  (in g):

$$n = \frac{N_{\text{A}} \cdot \rho}{M_{\text{mol}}} \quad (3.3)$$

where  $N_{\text{A}}$  is the Avogadro number.

In the simulation routine, after a MFP has been calculated from the given cross sections, an interaction distance  $d$  can be sampled using a random number  $R$  between 0 and 1:

$$d = -\lambda \cdot \ln(R) \quad (3.4)$$

After determination of the interaction length, the interaction type has to be determined. The interaction type is chosen by creating a random number between 0 and  $\sigma_{\text{total}}$  while each interaction is weighted according to their partial contribution to the total cross section. Interactions are then sampled and it is calculated whether the projectile suffers an energy loss and/or a change of direction. In case of an energy deposition event, the deposited energy and its location

---

---

is stored. The possible creation of secondary particles is considered in case of an ionization event and the secondaries are pushed on a particle stack to be followed later. The projectile is then sent back to the main routine with its current energy, position and direction vector and a new mean free path is sampled for the actual projectile energy. Projectiles (electrons, ions) are followed until they leave the target volume of consideration or until their energy drops below a certain cut-off energy which can be chosen as low as interaction cross sections are available.

---

### Cut-off value

---

In MC simulations, a cut-off value has to be chosen which determines the low-energy threshold when an electron is finally absorbed and its track is no longer followed. It is usually the energy below which no further inelastic cross sections are available. Considering the ionization threshold, this value lies is of the order of 10 eV. The range of electrons with 10 eV is extremely small (can be below 1 nm depending on the target material) which might justify the choice of this cut-off value. However, reducing this cut-off value to the energy corresponding to the minimum energy loss provided by an excitation channel might better reflect reality. Certain interactions like the production and recombination of radicals are linked to individual excitation transitions or ionization of certain sub shells and could in principle be followed as long as these interactions are sampled. Impacts of the choice of the electron cut-off value while calculating radiation damage are discussed in chapter 6.

---

## 4 Extensions of the TRAX Code

The track structure MC code TRAX has been developed over several years at GSI by Michael Krämer [KrKr1994, Kraemer1995, KrDu2010]. It has been extended extensively in the framework of this thesis which will be discussed in this chapter. Further details about the TRAX code are presented in section 4.1. The most important input parameters on which the calculations are based are suitable interaction cross sections. The extended cross section database is presented in section 4.2. Details about the extension to follow the creation of Auger electrons are discussed in section 4.3. Section 4.4 deals with the handling of non-uniform targets, another new feature which has been developed.

---

### 4.1 TRAX

---

---

#### Input

---

TRAX is designed for the single interaction approach and can handle electrons and ions of any charge state as projectiles. In the previous TRAX version, which is labelled as "TRAX classic" within this thesis, interactions considered for electrons are elastic scattering and ionization for all target materials and excitation for only a few materials ( $\text{H}_2\text{O}$ , O,  $\text{O}_2$  and  $\text{N}_2$ ). For ion projectiles, only ionization and excitation (covering  $\text{H}_2\text{O}$ , O,  $\text{O}_2$  and  $\text{N}_2$ ) have been taken into account. Excitation cross sections for ions can be obtained by scaling the cross sections for electrons. Elastic scattering has been neglected. Hard-coded internal cross section calculations are provided as fall-back estimations but are intended to be extended or replaced by external tables if improved cross sections are available for a certain material.

Internal cross section calculations rely on parameters for properties of the medium, like the density and shell structure information (including binding energies, number of electrons in a specific shell and their kinetic energy). This information is stored in external targetfiles which are read in at the start-up of the code. As far as possible, parameters are described by experimental values. A database of external target files exists, which covers various target materials which can be atomic, molecular, compounds or a mixture. The database includes predefined materials like e.g. air or plastics. This database can easily be extended to consider additional target materials. For simulations in living systems, water is considered as a tissue equivalent material.

The availability of excitation and ionization cross sections defines the lower energy limit for electron calculations. Due to the scarce database for excitation cross sections, the lower limit in TRAX classic has been of the order of the ionization threshold which lies around 10 eV, depending on the material. For most target materials with unavailable excitation cross sections, the ionization threshold has therefore been the limiting factor which had to be taken as cut-off energy. For carbon, e.g., this has been 11.26 eV. Furthermore, with unavailable excitation cross sections for many atomic materials, a significant contribution to the stopping power below 100 eV has been neglected. The higher energy limit of TRAX lies for ions at a few hundred MeV/u and for electrons at a few MeV. Currently TRAX does not follow nuclear fragmentation

---

and does not account for energy losses due to bremsstrahlung. However, for nuclear fragmentation the cross section is several orders of magnitude lower than for elastic scattering, excitation and ionization which justifies this neglect.

Simulation geometries have to be defined and can be chosen as a combination of cylinders, spheres or boxes and consist of any material which is present as targetfile in the database. Calculation time is much larger using the single interaction approach rather than condensed random walk. Therefore, although possible, it is not recommended to perform simulations for high energies or volumes exceeding cm dimensions.

---

## Output

---

TRAX follows the trajectories of ions and electrons interaction by interaction through the target material of consideration. Positions and energy depositions of each interactions can either be evaluated immediately "on the fly" or be stored as binary listmode files for analysis at a later stage. TRAX allows to extract various radiation quantities directly from the track structure simulations. Electron backscattering and transmission coefficients, radial and depth dose distributions, microdosimetric data like y- and z-distributions, electron spectra (energy and angular resolved) as well as ionization distributions can be obtained.

---

## 4.2 Cross sections for ion and electron interactions with matter

---

The quality of the simulations for a certain target material depends on the used cross section inputs, of course. Within this section, the standard input cross sections for TRAX classic and their theoretical background are explained as well as cross section extensions that have been performed in the framework of this thesis. Cross section models used in TRAX classic as hard-coded fall-back estimations are usually valid for a large range of target materials while for specific targets of interest, advanced methods or empirical corrections are used to obtain improved cross sections. In the framework of this thesis, focus has been laid on describing interactions for low energy electrons. Therefore, besides including elastic scattering for ions, cross sections for ions have been left unchanged. For electrons, almost all cross sections have been improved or extended. Covered interactions are electronic excitation, plasmon excitation, ionization and elastic scattering. Complete sets of electron cross sections have been compiled and assessed for C, Ni, Ag, Au, Al, Fe, Gd and Pt. Details are given in the following subsections. Used cross sections allow the differentiation between ionization of certain sub-shells and handle excitation as a separate interaction rather than using a complete description for inelastic scattering. This allows to follow what happens after these events in more detail. The creation of Auger electrons, e.g., is dependant on the shells which have been ionized. To be able to correctly reproduce their creation, a shell specific ionization cross section is mandatory. In the framework of this thesis, the handling of Auger electron has been implemented in TRAX and is described in section 4.3. For extensions at a later stage, like the direct sampling of radical production and recombination, knowledge is needed about the concrete type of ionization or excitation.

---

---

## 4.2.1 Electronic excitation

---

Information about individual electron or ion induced electronic excitation transitions is extremely scarce. In the classic TRAX version, electron induced excitation has been considered only for H<sub>2</sub>O according to [PaBe1978] and for O, O<sub>2</sub> and N<sub>2</sub> according to [GrSt1972]. Green and Stolarski provide a semi-empirical model to obtain excitation cross sections with parameters from experimental data. In principle, their model could be applied to other materials as well but only if the corresponding experimental information is available. Excitation plays a major role in energy losses for electrons at energies lower than 100 eV. Therefore, to improve the transport description of low energy electrons, consideration of excitation is mandatory for all target materials of interest. From experimental results for electron induced excitation of N<sub>2</sub> [Trajmar1983] it can be deduced that the angular distribution of electrons exciting molecular levels is strongly peaked forward. Therefore it can be assumed that in electronic excitation, deflection is negligible. In TRAX, excitation is therefore handled as an interaction where only an energy loss occurs, while the projectile remains its propagation direction.

If one is not interested in the details after an excitation event, excitation can be considered as accumulated cross sections of several possible excitation transitions, with an energy dependent mean energy transfer. Using the approach with a mean kinetic energy transfer, the excited state of a target molecule is not clearly defined and it cannot be followed what happens after a certain excited state is created. However, the sampling of an excitation event in its simplest form, does consider only a transfer of a discrete amount of energy and the summation of different excitation channels is therefore justified when following radical production and recombination in detail is not required.

In the framework of this thesis, research has been done to assess low energy electron excitation cross sections for separate channels and a broad range of target materials. Focus has been given on assessing cross sections for individual transitions for single electron transitions from one sub-shell to another.

As consideration of single excitation channels have not been important so far, an accumulated excitation cross section for  $n$  channels was calculated. The resulting average energy loss, which is the same as a mean kinetic energy transfer, can be calculated from the specific energy losses  $\Delta E_i$  (for the  $i$ -th transition channel) with corresponding cross sections  $\sigma_i(T)$  as a function of the kinetic energy  $T$  of the incoming projectile:

$$\sigma_{total}(T) = \sum_{i=1}^n \sigma_i(T) \quad \Delta E_{average}(T) = \sum_{i=1}^n \frac{\Delta E_i \cdot \sigma_i(T)}{\sigma_{total}(T)} \quad (4.1)$$

This approach can be justified as the different excitation channels do only differ in the amount of energy needed for the excitation. There is no qualitative difference which could be considered as long as the de-excitation process is not handled explicitly. However, to be able to follow radical production in the future, cross sections for different excitation transitions have been compiled separately to provide the information if needed.

For each atomic target material, the ground state electron configuration has been considered to identify possible electron transitions through excitation events. To describe these transitions, the state of the target atom before and after the excitation transition is defined in terms of the electron configuration which describes the states of the electrons. In a multielectron atom, the

---

---

quantum state of an individual electron can be described with a set of four quantum numbers  $n, l, m_l$  and  $m_s$  [HaReWa2005].  $n$  is the principal quantum number,  $l$  the orbital quantum number,  $m_l$  the orbital magnetic quantum number and  $m_s$  the magnetic spin quantum number [HaReWa2005].  $l$  can be an integral number between 0 and  $n-1$  and for  $m_l$  values between  $-l$  and  $l$  are allowed [HaReWa2005]. The spin of an electron can be either up or down and  $m_s$  can have values  $-1/2$  or  $1/2$  [HaReWa2005]. All quantum states having the same quantum numbers  $n$  and  $l$  form a subshell [HaReWa2005]. In usual subshell notations, the orbital quantum number  $l=0$  is labelled as s,  $l=1$  as p,  $l=2$  as d,  $l=3$  as f and higher quantum numbers are replaced alphabetically. Due to the Pauli exclusion principle it is not possible, that electrons located in a certain subshell of the target atom have the exact same set of quantum numbers [HaReWa2005]. Therefore, transitions due to electron excitation are only possible to subshells which are not already filled and therefore closed. For a p shell, e.g., possible  $m_l$  values are  $-1, 0, 1$  and  $m_s$  can be  $-1/2$  or  $1/2$ . Therefore, up to 6 electrons can be located in a p shell. As only single electron transitions are considered, only the quantum numbers for the single electron changing its subshell (and therefore its quantum numbers) are needed to label the transition of consideration. For individual electron excitation, the transition is usually labelled only with quantum numbers  $n$  and  $l$ . So a single electron transition could be something like  $2s-2p$  or  $3s-4s$ . As also  $m_l$  and  $m_s$  can change, transitions through excitation can also be something like  $2p-2p$ , if the electron subshell is not already filled.

Some excited states can lead to the emission of a target electron in their relaxation process. This process is called auto-ionization. Many of these states lie above the first ionization potential [GrSt1972]. The process is difficult to describe in terms of the kinetic energy of the electron created by auto-ionization.

A database covering reliable low-energy electron excitation cross sections for a broad range of atomic or molecular target materials in a neutral charge state does not exist. NIST [NIST] provides in its database "Electron-Impact Cross Sections for Ionization and Excitation" only excitation cross sections for H, He and Li and covers only a few transitions (like single electron transitions from  $1s$  to  $2p, 3p, \dots, 10p$  for H, the same for He, and excitations from  $2s$  to  $2p, 3p, \dots, 10p$  for Li). Therefore, required excitation cross sections have been compiled and assessed from different approaches. As far as possible, experimentally measured cross sections have been preferred rather than theoretical descriptions. In the case where various theoretical descriptions existed, their results did not agree and validation is complicated or impossible. It has been found that in general, electron-impact cross sections based on different theoretical methods show poor agreement [SuKa2006].

For carbon, description of electron excitation is extensively discussed in a review of Suno et al. [SuKa2006] which has been considered to calculate suitable cross sections. Further details are described in section 4.2.1.1. For gold, experimental data exist to describe electron excitation [Maslov2008, Zatsarinny2008]. Descriptions for electronic excitation of gold are discussed in section 4.2.1.3. For water, electron excitation is mentioned in a review by Nikjoo [Nikjoo2006] and information about sub-excitations are given by Michaud [Michaud2003]. Cross sections for electronic excitation of water are discussed in section 4.2.1.4. For all other target materials of interest, as no further detailed information has been available, calculated excitation cross sections have been extracted from the ACE (Another Collisional Excitation) code [Clark1988], which is based on distorted-wave methods and allows calculation of excitation cross sections for atomic targets up to  $Z=74$  down to the lowest

---

possible incident energies to induce an electron transition. Further details about calculations using the ACE code are discussed in section 4.2.1.2.

---

#### 4.2.1.1 Carbon targets

---

For atomic neutral carbon, cross sections for electron-impact excitation have been assessed using the formula and parameters given in a review by Suno and Kato [SuKa2006] to obtain a calculated set of collision strengths. Calculations using the R-matrix method [Burke1971, BuDu1994] provide cross section calculations for a large number of transitions between electron subshells with  $n=2$  and  $n=3$  [Dunseath1993]. Parameters are provided in [SuKa2006] for 21 individual transitions from the ground state with energy losses between 1.26 eV for the  $1s^2 2s^2 2p^2 \ ^3P - 2s^2 2p^2 \ ^1D$  transition and 14.9 eV for the  $1s^2 2s^2 2p^2 \ ^3P - 2s 2p^3 \ ^1P$  transition. These parameters have been obtained by a fit to collision strengths from [Dunseath1993]. The channels are listed in table 4.1. The R-matrix method has been used for electron-atom collisions by Burke [Burke1971]. Results from this method are recommended as they are best suited for low energy electrons [SuKa2006, Burke1971]. However, the method is supposed to be computationally expensive. To obtain cross sections from collision strengths, the following relation between the collision strength  $\Omega$  and the corresponding cross section  $\sigma$  from a state  $i$  to a state  $f$  can be used [SuKa2006]:

$$\sigma_{if} [cm^2] = 1.1969 \cdot 10^{-15} \cdot \frac{\Omega_{if}}{\omega_i \cdot E_e [eV]} = 1.1969 \cdot 10^{-15} \cdot \frac{\Omega_{if}}{\omega_i \cdot V_{if} [eV] \cdot X} \quad (4.2)$$

The reduced energy  $X$  is the ratio of the energy of the incident electron  $E_e$  divided by the excitation energy  $V_{if}$ .  $\omega$  is the statistical weight of the initial target atom state and can be derived from the quantum numbers  $L$  and  $S$  of the atomic level (described by  $^{2S+1}L_J$ ):

$$\omega = [(2L + 1)(2S + 1)] \quad (4.3)$$

As the ground state of carbon can be described with the atomic level  $^3P_0$ , the statistical weight  $\omega$  for transitions from the ground state yields 9. Energy losses for all excitation channels have been experimentally obtained by Moore [Moore1970] and are listed in the parameter table by Suno and Kato [SuKa2006]. The excitations are all considered from the ground state of carbon which is  $1s^2 2s^2 2p^2$ .

Another publication [Ganas1981] provides different theoretical cross sections for electron-impact excitation of carbon based on the Born approximation and using generalized oscillator strengths. Transitions are considered from the ground state to subshells 3s, 4s, 5s, 3p, 4p, 3d, 4d and 5d [Ganas1981]. As the Born approximation is not valid for low energies, the cross sections from Ganas have not been considered. For energies below a few keV, cross sections from [SuKa2006] are supposed to be more accurate. A comparison shows, that cross sections mentioned in [Ganas1981] and [SuKa2006] agree in their energy dependency, but not in their absolute values which can be seen in Fig. 4.1.

---

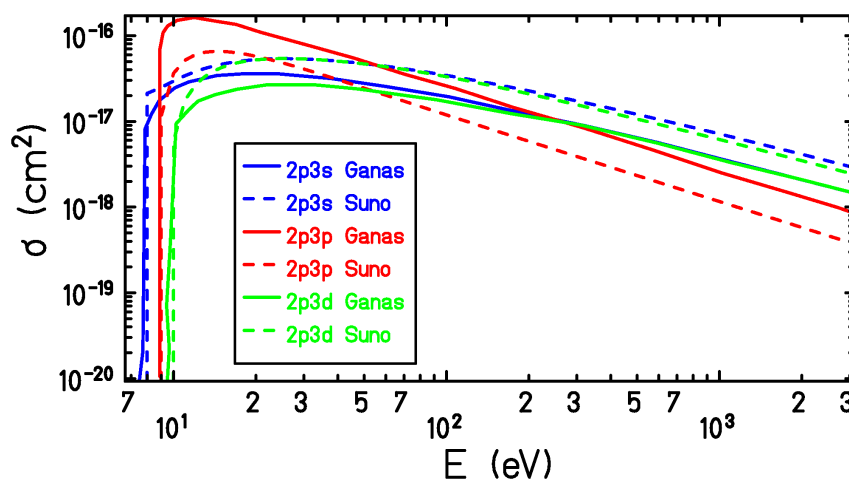


**Figure 4.1:** Cross sections for 2p-3s, 2p-3p and 2p-3d excitations are compared for the results mentioned in [Ganas1981] (which have been digitized) and for the results calculated according to [SuKa2006].

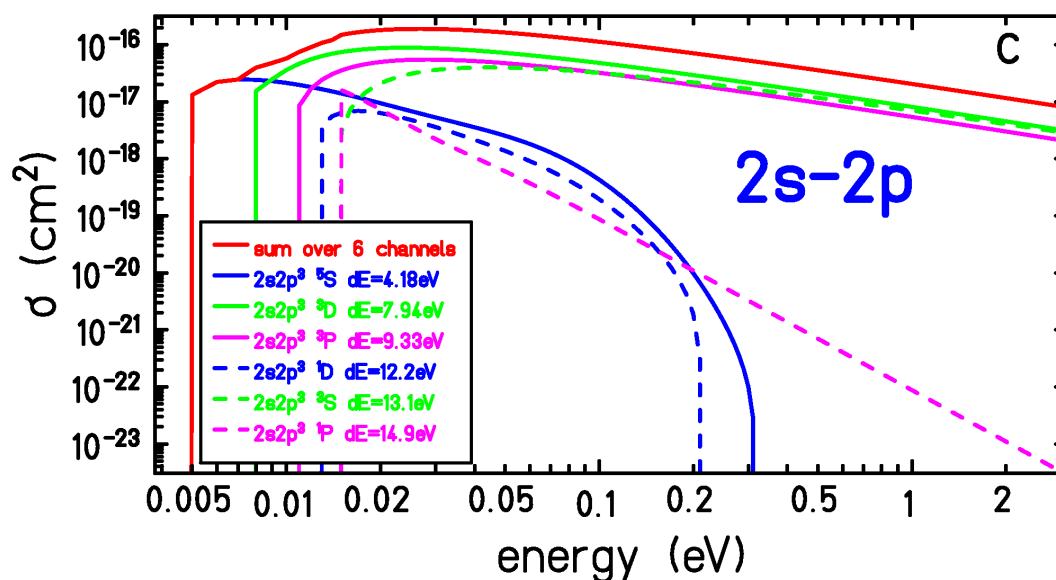


**Figure 4.2:** Summed cross section from six 2s-2p excitation channels are shown as a function of incident electron energy. Energy losses from these channels vary from 4.18 eV to 14.9 eV. The energy dependencies are differing as well.

Fig. 4.2 shows exemplarily the cross sections derived for six individual electron transitions that can be summed to describe the 2s-2p transitions in carbon. Fig. 4.3 shows the sum for all 21 transitions as well as the contributions from different types of electronic excitation, like 2s-2p, 2p-2p, 2p-3s, 2p-3p and 2p-3d excitations. Fig. 4.4 shows the final sum of cross sections and the corresponding mean energy transfer which has been derived as a function of the incident electron energy  $T$ . The energy dependent energy loss for excitation has been calculated as an average value of energy losses from all channels which has been weighted by the individual cross sections according to formula 4.1.



Two of the 21 considered excitation transitions (channel 19 and channel 20) are considered to be leading to auto-ionization [KiDe2002]. In Fig. 4.19 cross sections for these two excitation channels are shown which are added to the direct ionization cross section to reproduce experimental ionization cross sections.

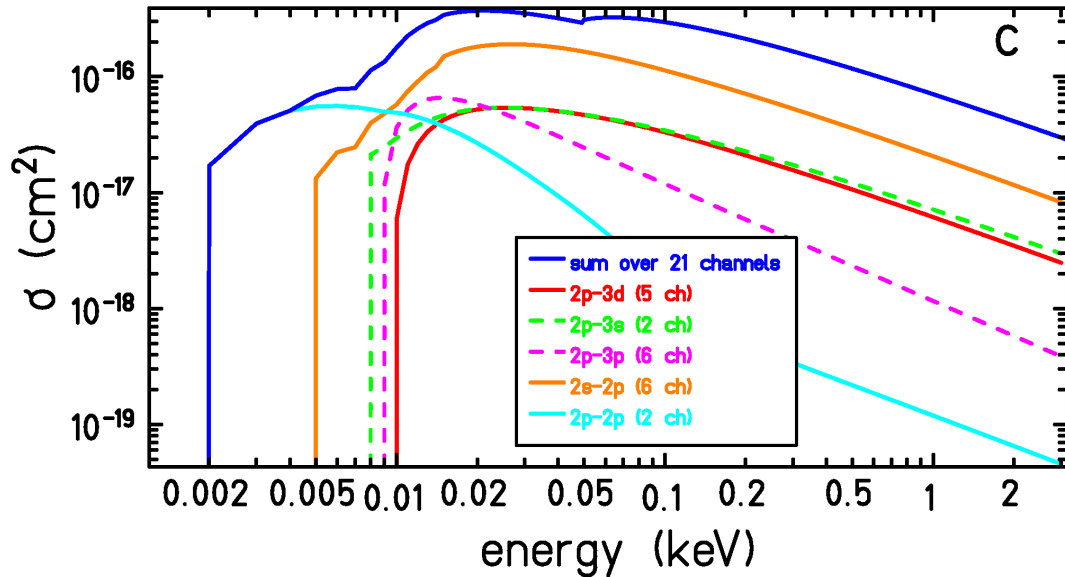


**Figure 4.3:** The sum over all 21 excitation channels is shown as well as the contributing sums over certain channels for the different types of electron transitions.

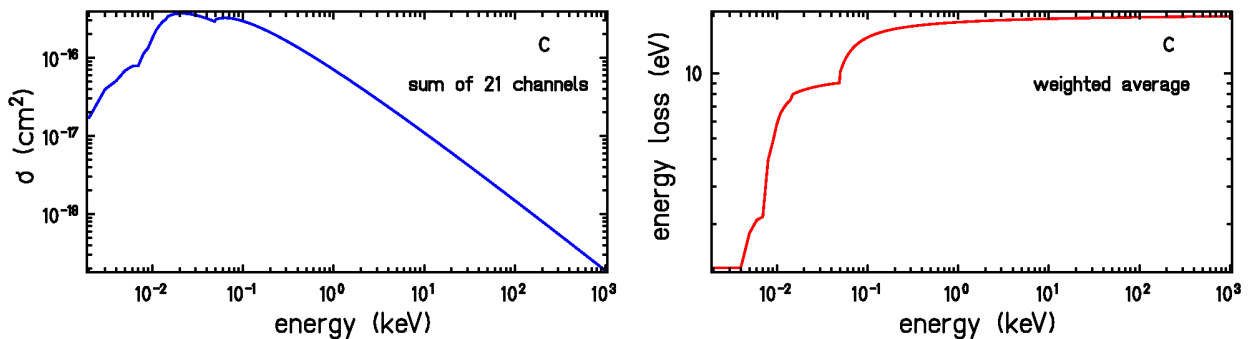


**Figure 4.4:** On the left hand side, the summed cross section of all 21 excitation channels as a function of incident electron energy is shown. On the right hand side, the corresponding mean energy loss is shown which has been calculated as an average value from energy losses for all transitions weighted by the cross sections of the individual channels.

channel number	transition to state	type	energy loss (eV)
1	$2s^2 2p^2 \ ^1D$	2p-2p	1.26
2	$2s^2 2p^2 \ ^1S$	2p-2p	2.68
3	$2s 2p^3 \ ^5S$	2s-2p	4.18
4	$2s^2 2p^1 3s \ ^3P$	2p-3s	7.48
5	$2s^2 2p^1 3s \ ^1P$	2p-3s	7.68
6	$2s 2p^3 \ ^3D$	2s-2p	7.94
7	$2s^2 2p^1 3p \ ^1P$	2p-3p	8.53
8	$2s^2 2p^1 3p \ ^3D$	2p-3p	8.64
9	$2s^2 2p^1 3p \ ^3S$	2p-3p	8.77
10	$2s^2 2p^1 3p \ ^3P$	2p-3p	8.85
11	$2s^2 2p^1 3p \ ^1D$	2p-3p	9.00
12	$2s^2 2p^1 3p \ ^1S$	2p-3p	9.20
13	$2s 2p^3 \ ^3P$	2s-2p	9.33
14	$2s^2 2p^1 3d \ ^1D$	2p-3d	9.63
15	$2s^2 2p^1 3d \ ^3F$	2p-3d	9.69
16	$2s^2 2p^1 3d \ ^3D$	2p-3d	9.71
17	$2s^2 2p^1 3d \ ^1F$	2p-3d	9.73
18	$2s^2 2p^1 3d \ ^3P$	2p-3d	9.83
19	$2s 2p^3 \ ^1D$	2s-2p	12.2
20	$2s 2p^3 \ ^3S$	2s-2p	13.1
21	$2s 2p^3 \ ^1P$	2s-2p	14.9

**Table 4.1:** 21 excitation channels considered by Suno 2006. All transitions are considered from the ground state  $1s^2 2s^2 2p^2 \ ^3P_0$ . Information taken from Suno et al. [SuKa2006]. For improved readability the  $1s^2$  part has been left out in the description of the final state.

#### 4.2.1.2 Various metallic targets

For the target materials Al, Fe, Ni, Ag and Gd, where no detailed information about excitation cross sections has been available, excitation cross sections could be extracted from the ACE (Another Collisional Excitation) code [Clark1988] from the Los Alamos Laboratory which provides theoretical cross sections for excitations describing single electron transitions between different subshells. The ACE code uses distorted wave Born approximations according to [Mann1983]. Theoretical excitation cross sections based on distorted wave methods are considered to be reasonable accurate at energies about two to three times higher than the ionization threshold [Maslov2008]. The ionization threshold typically lies in the order of about 6-12 eV.

To obtain cross sections from the ACE code, the electron configurations before and after the transition have to be chosen by the user. For wave functions of the ground states as well as excited states, ACE calculations are based on the self-consistent Hartree-Fock approach with relativistic corrections for each orbital of each input configuration according to [Cowan1981]. Incoming and outgoing free-electron continuum functions each "see" different potentials, those of the spherically averaged initial and final target ion configurations.

ACE allows to choose between calculations in fine structure or configuration mode. The con-

figuration mode uses the term-to-term transition energy and sums over all transitions for the same subshells involved, e.g. 2p-3p excitations. The fine-structure mode allows to distinguish between several possible final states for the target atom which differ in energy and quantum numbers using the level-to-level transition energy [Clark1988].

Using the ACE code, excitation transitions have to be defined by the user itself. All excitation channels which have been compiled and assessed within this thesis are considered as transitions from the ground state of a target atom. Therefore, single electron transitions to the nearest lying upper electron subshells have been calculated. According to the standard order of filling of subshells for electron configurations, higher lying electron subshells have been determined. The usual subshell order has been considered to be 1s-2s-2p-3s-3p-4s-3d-4p-5s-4d-5p-6s-4f-5d-6p-7s-5f-6d-7p...

To determine which excitation transitions are possible, the ground state configuration of the target material of consideration has to be known. The ground state of an iron atom, e.g., is  $1s^2 2s^2 2p^6 3s^2 3p^6 3d^6 4s^2$ . As a s-subshell can hold 2 electrons, a p shell 6 and a d shell 10 electrons, the first 5 subshells and the 7th subshell are closed while the 6th subshell 3d is not. Excitation transitions which are supposed to be strongest, involve transitions from the outermost subshells 3d and 4s to higher lying subshells. As the 3d subshell can hold 4 additional electrons, transitions from the 4s subshell to 3d have to be considered as well. As 4s is closed, transitions from 3d can not go to 4s. The groundstate electron configuration of Fe does not have a  $3d^8$  part in the electron configuration as  $3d^6 4s^2$  contribution lies energetically below  $3d^8$ . For Fe, using the ACE code, cross sections have been obtained for 20 excitation channels including 12 excitation channels from the 4s shell and 8 channels from the 3d shell.

Where feasible, calculations have been performed using the fine-structure mode. For atoms with low or intermediate Z values like Al, Fe and Ni, numerous channels are available, which can exceed 100 transitions. In these cases the configuration mode has been preferred. Usually, transitions have been considered to upper lying subshells until they contributed much less than 1% to the total excitation cross section at 100 eV. The contributions from the nearest lying upper subshells are most significant. The energy loss for each excitation channel is provided by ACE through the energetic difference between the initial and final state of the target atom. In the following, tables and plots are given for excitations of each material of interest.

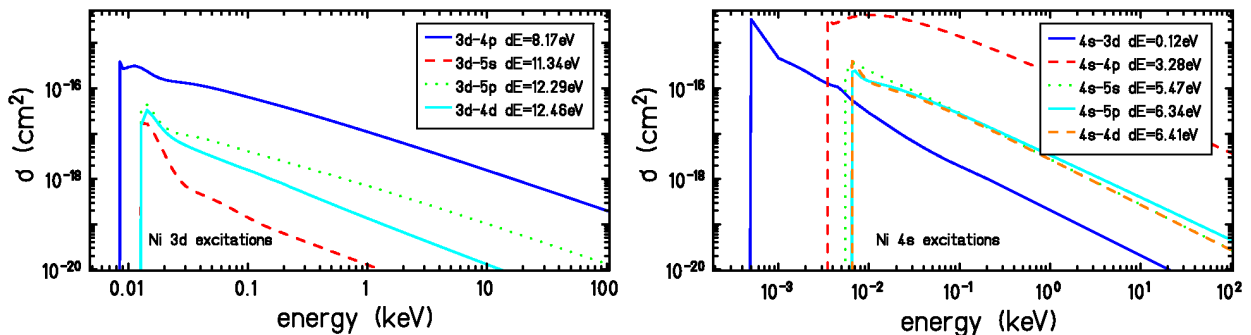


**Figure 4.5:** Electronic excitations from the outermost electrons levels 3d and 4s of Ni. The cross sections were obtained using the ACE code with distorted wave approximation. Four channels for excitations of electrons from the 3d subshell have been considered as well as five channels for transitions for 4s electrons. The cross sections are dominated by transitions to the (energetically) nearest lying electron subshells.

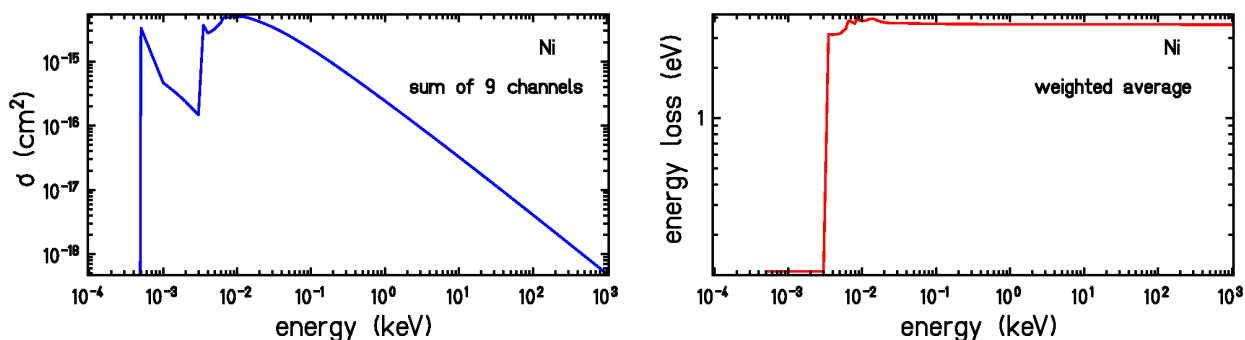


**Figure 4.6:** On the left hand side, the summed cross section of all considered excitation channels as a function of incident electron energy is shown for nickel, calculated using the ACE code. On the right hand side, the corresponding mean energy loss is shown which has been calculated as an average value from energy losses for all transitions weighted by the cross sections of the individual channels.

channel number	transition type	energy loss (eV)
1	4s-3d	0.12
2	4s-4p	3.28
3	4s-5s	5.47
4	4s-5p	6.34
5	4s-4d	6.41
6	3d-4p	8.17
7	3d-5s	11.34
8	3d-5p	12.29
9	3d-4d	12.46

**Table 4.2:** 9 excitation channels for electrons incident on Ni considered from ACE calculations [Clark1988] using distorted wave methods and the configuration mode. All transitions were calculated from the ground state  $1s^2 2s^2 2p^6 3s^2 3p^6 3d^8 4s^2$   $^3F_4$  [webelements].

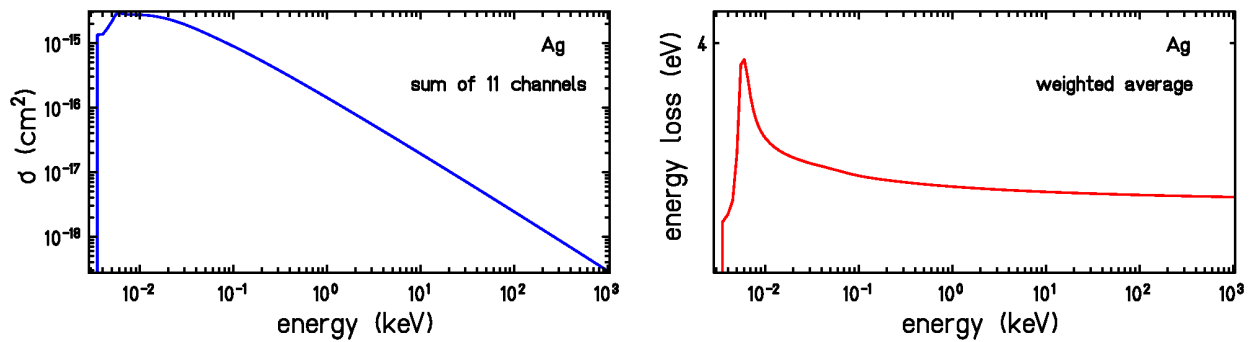


**Figure 4.7:** On the left hand side, the summed cross section of all considered excitation channels as a function of incident electron energy is shown for silver, calculated using the ACE code. On the right, the corresponding mean energy loss is shown which has been calculated as an average value from energy losses for all transitions weighted by the cross sections of the individual channels.

channel number	transition to state	energy loss (eV)
1	5s-5p	3.28
2	5s-5p	3.36
3	4d-5s	3.78
4	4d-5s	4.32
5	5s-6s	4.78
6	5s-5d	5.45
7	5s-5d	5.45
8	5s-6p	5.46
9	5s-6p	5.48
10	5s-4f	6.13
11	5s-4f	6.13

**Table 4.3:** 11 excitation channels for electrons incident on Ag silver considered from ACE calculations using distorted wave methods and the fine structure mode. All transitions were calculated from the ground state  $1s^2 2s^2 2p^6 3s^2 3p^6 3d^{10} 4s^2 4p^6 4d^{10} 5s^1 \ ^2S_{1/2}$  [webelements].

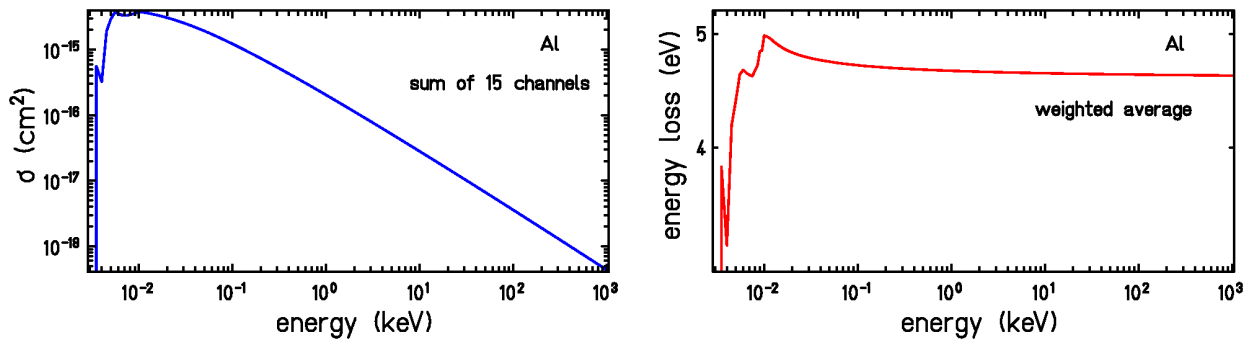


**Figure 4.8:** On the left hand side, the summed cross section of all considered excitation channels as a function of incident electron energy is shown for aluminium, calculated using the ACE code [Clark1988]. On the right hand side, the corresponding mean energy loss is shown which has been calculated as an average value from energy losses for all transitions weighted by the cross sections of the individual channels.

channel number	transition type	energy loss (eV)
1	3p-3d	4.42
2	3s-3p	4.68
3	3p-4s	3.30
4	3p-4p	4.27
5	3p-5s	4.84
6	3p-4d	5.21
7	3p-4f	5.29
8	3p-5d	5.56
9	3p-5p	5.16
10	3p-6s	5.39
11	3s-4s	7.92
12	3s-4p	8.88
13	3s-5s	9.53
14	3s-4d	9.87
15	3s-4f	9.98

**Table 4.4:** 15 excitation channels for electrons incident on Al considered from ACE calculations [Clark1988] using distorted wave methods and the configuration mode. All transitions were calculated from the ground state  $1s^2 2s^2 2p^6 3s^2 3p^1 \ ^2P_{1/2}$  [webelements].

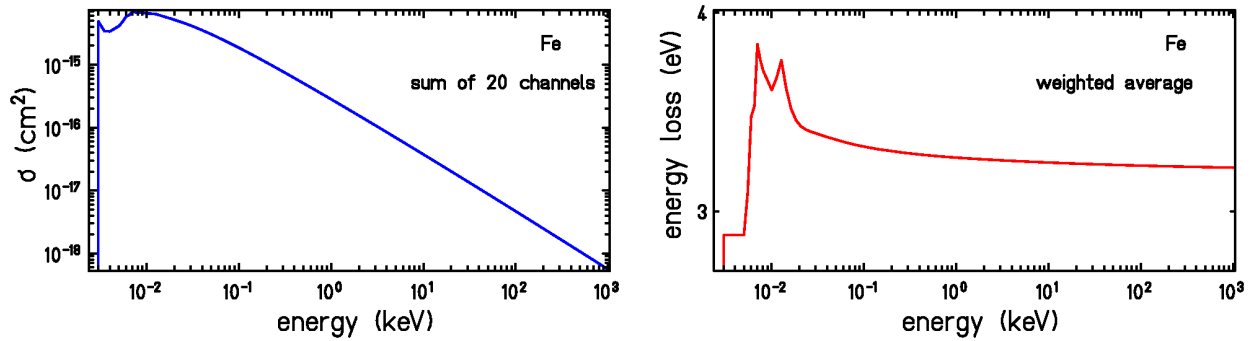


**Figure 4.9:** On the left hand side, the summed cross section of all considered excitation channels as a function of incident electron energy is shown for iron, calculated using the ACE code. On the right hand side, the corresponding mean energy loss is shown which has been calculated as an average value from energy losses for all transitions weighted by the cross sections of the individual channels.

channel number	transition type	energy loss (eV)
1	4s-4p	2.9
2	4s-5s	5.1
3	4s-4d	5.9
4	4s-5p	5.9
5	4s-6s	6.4
6	4s-4f	6.7
7	4s-5d	6.7
8	4s-6p	6.7
9	4s-7s	6.9
10	4s-5f	7.0
11	4s-6d	7.0
12	4s-7p	7.0
13	3d-4p	6.8
14	3d-5s	9.9
15	3d-4d	10.9
16	3d-5p	10.8
17	3d-6s	11.4
18	3d-4f	11.8
19	3d-5d	11.7
20	3d-6p	11.7

**Table 4.5:** 20 excitation channels for electrons incident on Fe considered from ACE calculations [Clark1988] using distorted wave methods and the configuration mode. All transitions were calculated from the ground state  $1s^2 2s^2 2p^6 3s^2 3p^6 3d^6 4s^2 \ ^5D_4$  [webelements].

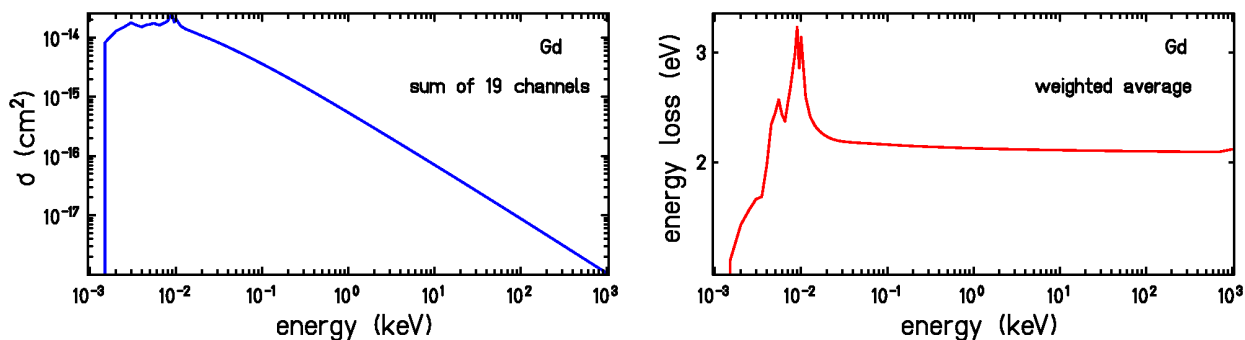


**Figure 4.10:** On the left hand side, the summed cross section of all considered excitation channels as a function of incident electron energy is shown for gadolinium, calculated using the ACE code. On the right hand side, the corresponding mean energy loss is shown which has been calculated as an average value from energy losses for all transitions weighted by the cross sections of the individual channels.

channel number	transition type	energy loss (eV)
1	6s-6p	1.99
2	6s-7s	3.73
3	6s-5f	4.94
4	6s-7p	4.37
5	6s-6d	4.40
6	6s-6f	5.26
7	6s-7d	5.03
8	6s-8s	4.77
9	6s-8p	5.01
10	5d-6p	1.50
11	5d-6d	4.53
12	5d-7s	3.77
13	5d-5f	5.13
14	5d-7p	4.47
15	5d-7d	5.20
16	6s-5d	1.39
17	4f-5d	6.39
18	6s-4f	1.52
19	4f-6p	8.84

**Table 4.6:** 19 excitation channels for electrons incident on Gd considered from ACE calculations [Clark1988] using distorted wave methods and the configuration mode. All transitions were calculated from the ground state  $1s^2 2s^2 2p^6 3s^2 3p^6 3d^{10} 4s^2 4p^6 4d^{10} 5s^2 5p^6 4f^7 5d^1 6s^2 \ ^9D_2$  [webelements].



---

### 4.2.1.3 Gold targets

---

For electron impact excitation of gold, measurements exist which provide cross sections for the three most important electron transitions. Experimental data are preferred rather than theoretical results. For three transitions, experimental cross sections are available and these are transitions from the ground state to the  $(5d^{10}6p)^2P_{1/2}$  state with an energy transfer of 4.6 eV, from the ground state to the  $(5d^{10}6p)^2P_{3/2}$  state ( $\Delta E=5.1$  eV) and from the ground state to the  $(5d^96s^2)^2D_{3/2}$  state with an energy loss of 2.7 eV [Maslov2008, Zatsarinny2008]. Measurements have been performed at incident electron energies from the threshold up to 577 eV for the transitions to P states [Maslov2008] and up to 5.8 eV for the transition to the D state [Zatsarinny2008]. As experimental values for the excitation cross sections are only given up to certain energies, the cross sections have to be extrapolated to higher energies. For higher energies the Bethe-Born approximation is valid and the cross sections can be described by atomic units [BrJo1983, Maslov2008]:

$$\sigma E = 4\pi f_0 \ln(E) \quad (4.4)$$

$f_0$  denotes the optical oscillator strength for the considered individual transition. From this relation, a dependency of the cross section proportional to  $\ln(E)/E$  can be derived (energy E given in Ry). For the transition to the D state, another dependency has to be considered. The transition to the D state is optically forbidden and seen as a second order effect with an energy dependency of  $\sigma \propto 1/E^2$  at higher energies [Maslov2008]. Cross sections for forbidden transitions show an early maximum (at less than two times the excitation threshold) and have a rapid fall off with increasing energy [GrSt1972]. Transitions to P states are optically allowed, stronger and the cross sections are therefore less rapidly decreasing with an energy dependency of  $\sigma \propto \ln(E)/E$ . These dependencies have been applied to extrapolate the excitation cross sections and the results are shown in Fig. 4.11. The authors of the experimental cross sections consider an uncertainty of their results of  $\pm 20\%$  for the transitions to P states and a factor of 2 for the D state transition [Maslov2008, Zatsarinny2008].

Theoretical approaches for excitations in Au exist as well [Maslov2008, Zatsarinny2008] but it has been found, that these cross sections describe the measured energy dependency for energies above 100 eV, but not the absolute values. Theoretical approaches for further transitions have therefore been neglected as they would disagree with the used experimental cross sections. For the experimentally determined resonance transitions, theoretical cross sections are too large by a factor of about 2 [Maslov2008]. The neglect of further transitions than the three available from experiments is further justified, as from ACE calculations for other materials, a general trend can be conducted, that transitions to higher lying electron shells than those just above those included in the ground state configuration, do not contribute significantly to the total excitation cross section. Therefore it is not expected that excitation cross section would drastically increase when considering additional transitions like 6s-7s or 5d-6p. As ACE does only provide excitation cross sections up to  $Z=74$ , it is not possible to get excitation cross sections for heavy atoms like Au and Pt. Validations for the used excitation cross sections are performed indirectly by reproducing experimental data, e.g. for the stopping power of electrons in gold (Fig. 5.4).

---

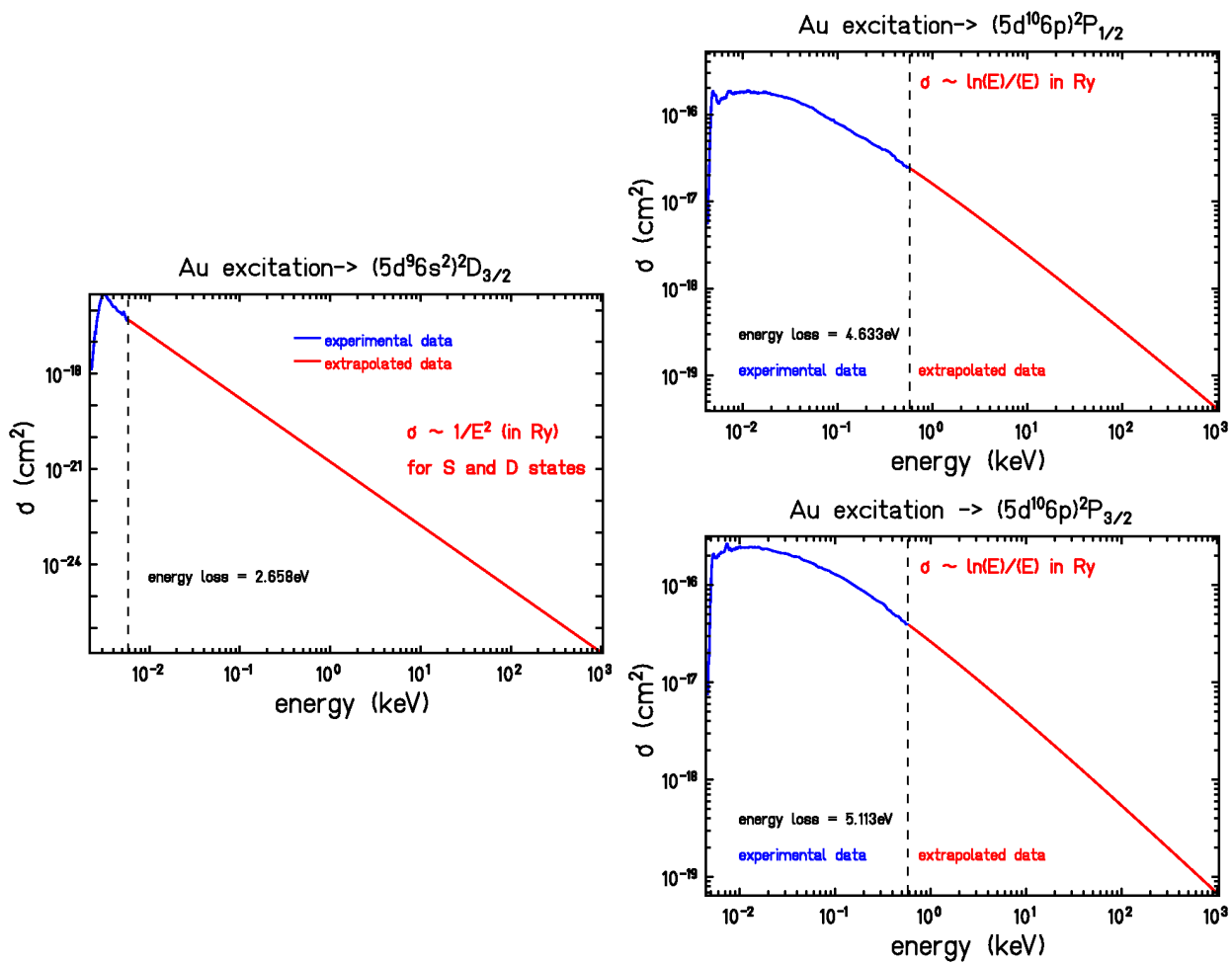


**Figure 4.11:** Experimental excitation cross sections have been extrapolated using theoretically known energy dependencies to obtain values for higher incident electron energies. The cross sections on the left hand side of the dashed lines are measured.

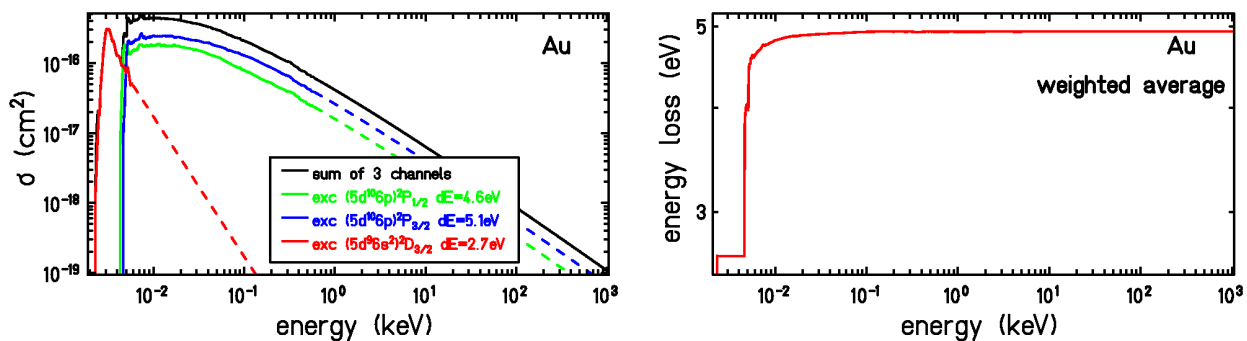


**Figure 4.12:** On the left hand side, the summed cross section of all considered excitation channels as a function of incident electron energy is shown for gold, obtained from experiments. On the right hand side, the corresponding mean energy loss is shown which has been calculated as an average value from energy losses for all transitions weighted by the cross sections of the individual channels.

---

channel number	transition to state	energy loss (eV)
1	6s-6p ( $^2P_{1/2}$ )	4.63
2	6s-6p ( $^2P_{3/2}$ )	5.11
3	5d-6s ( $^2D_{3/2}$ )	2.66

---

**Table 4.7:** 3 excitation channels for resonance transitions from the ground state of Au which is  $1s^2 2s^2 2p^6 3s^2 3p^6 3d^{10} 4s^2 4p^6 4d^{10} 5s^2 5p^6 4f^{14} 5d^{10} 6s^1 \ ^2S_{1/2}$  [webelements]. Data taken from [Maslov2008, Zatsarinny2008].

---

#### 4.2.1.4 Water

---

Excitation cross sections for electrons incident on water are discussed in a review of Nikjoo [Nikjoo2006]. TRAX classic cross sections for electronic excitation of water are based on parametrizations from Paretzke and Berger [PaBe1978, KrKr1994]. The corresponding mean kinetic energy transfer rises from about 8 eV to 13 eV for incoming electron energies between 10 eV and 100 keV. TRAX classic cross sections for electrons incident on H<sub>2</sub>O have been replaced by a more detailed set of cross sections from the same author, in which single excited states are distinguished. According to [Paretzke1988] and [GrSt1972], 8 excitation transitions for electrons incident on H<sub>2</sub>O should be considered. The energy losses to reach these possible excited states range from 7.4 eV to 21.0 eV. The description used in the classic TRAX version, includes a fit to these various excitation modes with fitting parameters determined by [BeWa1988]. For the extended TRAX version, the cross sections for the excitation modes have been calculated separately as described in [Nikjoo2006] and summed to compare with previous cross sections. Formula 4.1 has been used to obtain an accumulated cross sections with corresponding mean energy transfer.

Differences between the descriptions according to [PaBe1978] and [Paretzke1988] are minor, except below the threshold of 7.4 eV and are displayed in Fig. 4.13. The TRAX classic excitation cross section description seemed unrealistic for energies below the threshold.

In addition to the 8 channels for excitation, 9 channels for sub-excitation cross sections down to very low energies have been considered according to measurements in amorphous ice [Michaud2003]. These cross sections allow to consider sub-excitation channels down to 1.7 eV and allow to reduce the electron cut-off energy in simulations as without these channels, the lowest possible energy transfer would be 7.4 eV. The cross section data for amorphous ice is considered to have an uncertainty of 30-40% [Nikjoo2006]. The excitations considered as sub-excitations are not electronic excitations, where an electron changes its subshell position, but excitations leading to a certain vibrational, librational, translational, bending or stretching mode of the molecule. The impact of including these sub-excitation cross sections to the existing 8 channels for excitation are shown in Fig. 4.14. The overall cross section increases slightly up to 100 eV and the mean energy loss reduces correspondingly, as sub-excitation modes lead to very low energy losses ranging from 0.01 eV to 0.835 eV [Michaud2003]. They do not contribute much to the total electron stopping power and an uncertainty in the cross section data does not have a severe impact. However, for a complete description of low energy electron interactions they should be included. Even though energy losses down to 0.01 eV are described, cross sec-

---

tion data have only been measured down to 1.7 eV which is the limiting factor for the minimum possible cut-off value. The impact of a reduced cut-off energy will be discussed in chapter 6.

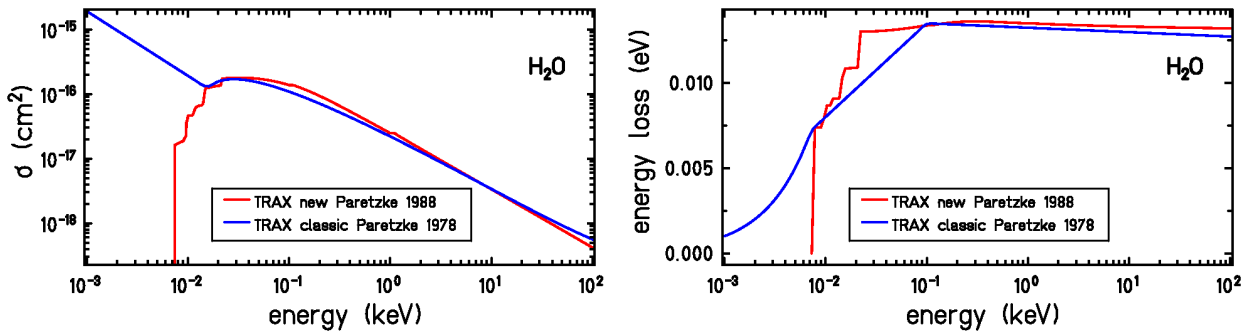


**Figure 4.13:** On the left hand side, the summed cross section of all considered excitation channels as a function of incident electron energy is shown for water, while the parametrization used in TRAX classic is compared to summation of 8 channels according to [Paretzke1988]. On the right hand side, the corresponding mean energy transfer is shown which is obtained by a parametrization in the case of TRAX classic, while it has been calculated as an average value from energy losses for all transitions weighted by the cross sections of the eight individual channels for the new cross sections.

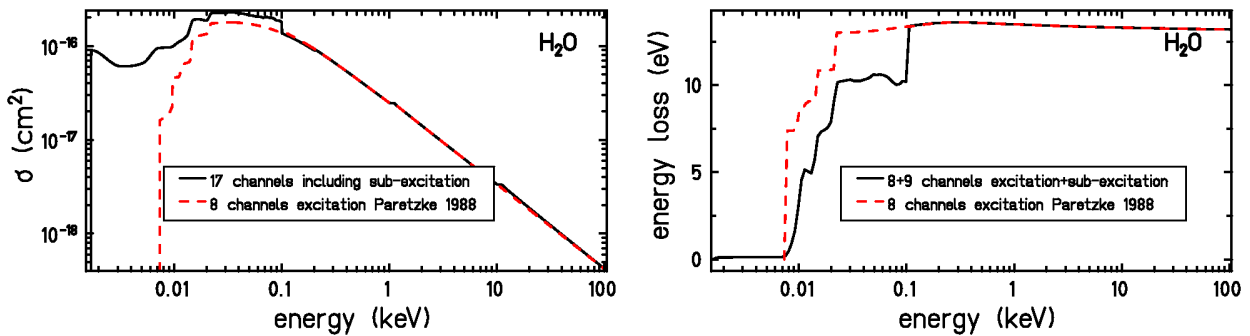


**Figure 4.14:** On the left hand side, the summed cross section of all considered excitation channels as a function of incident electron energy is shown for water. On the right hand side, the corresponding mean energy transfer is shown which has been calculated as an average value from energy losses for all transitions weighted by the cross sections of the individual channels. Including sub-excitation decreases the mean energy loss while the cross sections increase.

#### 4.2.2 Plasmon excitation

Plasmon excitation is a collective excitation of the valence electrons which is important for solids. The strength of the volume plasmon excitation depends on the number of valence electrons of the target material. Plasmon excitation has not been considered in the TRAX classic version and belongs to the extensions performed within the framework of this thesis.

Formulas to calculate the plasmon energy loss and the mean free path for plasmon excitation

---

for metallic targets are given by Quinn [Quinn1962]. The formula has been considered for Al, Fe, Ni, Ag, Gd, Au and Pt. Applying the given formulas allows to calculate cross sections and corresponding energy losses for volume plasmon excitation for electrons incident on metallic targets. Volume plasmon excitation describes the excitation of plasma oscillations by an excited electron. The description allows only calculations for a very simple type of volume plasmon excitation but it provides a method to obtain separate cross sections for plasmon excitation. The plasmon frequency  $\omega_p$  and the plasmon energy  $E_p$ , which is the energy loss for plasmon excitation are dependent on the valence electron density  $n$  and can be calculated via:

$$E_p = \hbar \cdot \omega_p = \frac{h}{2 \cdot \pi} \cdot \sqrt{\frac{n \cdot e^2}{\epsilon_0 \cdot m}} \quad (4.5)$$

$e$  is the elementary charge and  $m$  the mass of an electron,  $\epsilon_0$  being the electrical field constant. The contributing valence electron density  $n_v$  can be calculated using the density of the target material  $\rho$ , its molar mass  $M_{mol}$ , the number of valence electrons  $N_v$  and the Avogadro number  $N_A$  via:

$$n_v = \frac{\rho \cdot N_A \cdot N_v}{M_{mol}} \quad (4.6)$$

For materials with an enhanced number of valence electrons, the plasmon energy is higher. For atoms with only one valence electron, like Ag and Au, the plasmon energy is small (9.0 eV for both). For atoms with more valence electrons, the plasmon energy loss increases (2 valence electrons in Ni result in a  $E_p$  of 15.9 eV). Resulting plasmon energies for metallic target materials considered here can be found in table 4.2.2. Sometimes plasmon excitation is described for differing numbers of valence electrons for the same material. E.g., electrons from the two outermost electron shells can be involved in plasmon excitation. Within this thesis, plasmon excitation has been considered only for the "real" valence electrons from the outermost shell. Target valence electrons responsible for plasmon excitation are considered to be acting like a sea of conduction electrons interacting with the electron projectile [Quinn1962] and therefore approximated with a quasi-free electron gas for which a Fermi energy can be defined. In metals, the Fermi energy describes the highest occupied level at a temperature of 0 K. Fermi energies for metals are given by [AMe1976] and can also be calculated via:

$$E_F = \frac{h^2}{8 \cdot m} \cdot \left( \frac{3 \cdot n}{\pi} \right)^{2/3} \cdot \frac{1}{e} \quad (4.7)$$

Fermi energies for all considered metallic target materials are given in table 4.2.2. The Fermi momentum can be derived from the Fermi energy  $E_F$  via:

$$p_0 = \sqrt{2 \cdot m \cdot E_F} \quad (4.8)$$

The same formula (replacing  $E_F$  with  $E_{proj}$ ) can be applied to obtain the relativistic momentum from the projectile energy. The Fermi momentum  $p_0$  of the target electrons, the projectile energy  $E_{proj}$  and the projectile momentum  $p$  are needed to calculate the mean free path for

---

plasmon excitation which is according to [Quinn1962] (in SI units):

$$\lambda = \frac{2 \cdot a_0 \cdot E_{proj}}{\hbar \cdot \omega_p} \cdot \left[ \ln \left( \frac{(p_0^2 + 2 \cdot m \cdot \omega_p \cdot \hbar)^{1/2} - p_0}{p - (p^2 - 2 \cdot m \cdot \omega_p \cdot \hbar)^{1/2}} \right) \right]^{-1} \quad (4.9)$$

$a_0$  is the Bohr constant and  $\omega_p$  the plasmon frequency. From the mean free path  $\lambda$ , the cross section  $\sigma$  can easily be calculated via:

$$\sigma = \frac{1}{n \cdot \rho} \quad (4.10)$$

Here  $n$  is the particle density (number of atoms per unit volume) and  $\rho$  the density of the target material.

To handle plasmon excitation in the simulation, it is assumed that the electron projectile does not change its direction while undergoing plasmon excitation and the energy  $E_p$  is lost. Plasmon excitation is treated as an additional channel for excitation and is added to the channels for individual electronic excitation. The corresponding energy loss for an excitation as a function of incident electron projectile energy has been adapted to include this additional channel. At low energies, electronic excitations have much higher cross sections than plasmon excitation which is why the mean energy loss is almost not altered. At higher energies, plasmon excitation plays a bigger role and the energy loss is slightly modified. Fig. 4.15 shows cross sections for plasmon excitation and total excitation and explains the impact on the mean energy loss for excitation when plasmon excitation is added.

On an absolute scale, plasmon excitation contributes much less to the overall cross sections than individual excitations. Therefore, no significant uncertainties in the calculations are expected even though considering only the most simplest type of volume plasmon excitation.

element	# valence electrons	Fermi energy	plasmon energy
Al	3	11.7 eV	15.8 eV
Fe	2	11.1 eV	15.3 eV
Ni	2	11.74 eV	15.87 eV
Ag	1	5.49 eV	8.99 eV
Gd	3	7.36 eV	11.18 eV
Pt	1	5.90 eV	9.47 eV
Au	1	5.53 eV	9.00 eV

**Table 4.8:** Metallic elements with number of valence electrons that are involved in plasmon excitations. The Fermi energy is given by [AMe1976] or derived from formula 4.7. The plasmon energy has been calculated using formula 4.5.

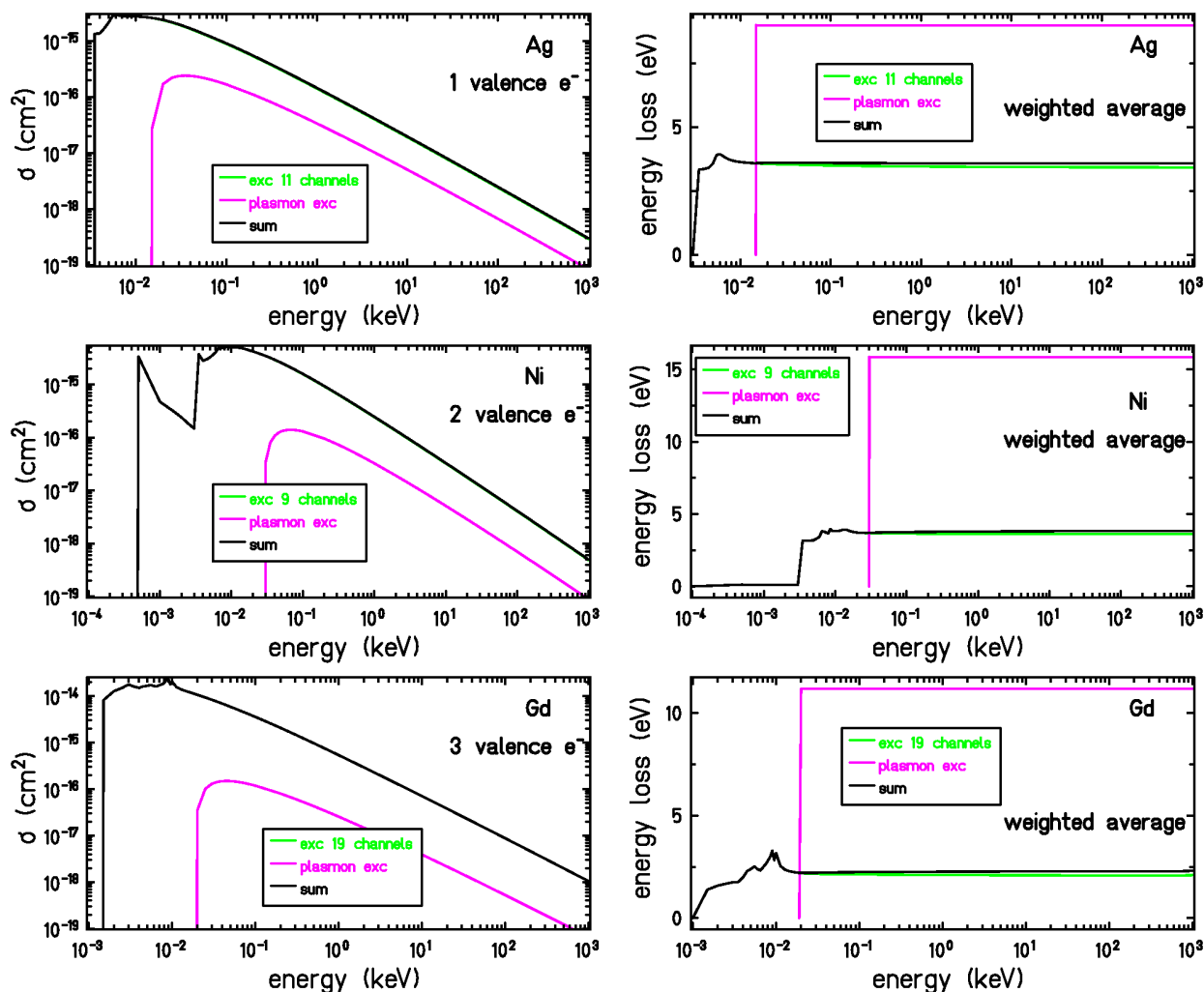


**Figure 4.15:** On the left hand side, the summed cross sections of all considered excitation channels as a function of incident electron energy is shown for electronic excitation, plasmon excitation and a sum of both. Exemplarily, Ag, Ni and Gd have been chosen (top to bottom). On the right hand side, the corresponding mean energy transfer is shown which has been calculated as an average value from energy losses for all transitions weighted by the cross sections of the individual channels. Including plasmon-excitation increases the mean energy loss slightly for higher projectile energies.

---

### 4.2.3 Ionization

---

In ionization events, the projectile scatters inelastically with a target atom and energy is transferred to a target electron which is removed from the orbital of a target atom. This removed electron will propagate as a secondary electron through the target medium and is treated in the simulation as an additional projectile. Secondary electrons can lead to damage far away from the track of the primary projectiles. The energy loss of the projectile is the sum of the binding energy, which is needed to remove the electron, and the kinetic energy which is transferred to the secondary electron. The binding energy of the outermost electron shell is the first ionization threshold. Below this threshold, ionization is not possible. Most of the energy deposited by ions is transferred indirectly by creation of secondary electrons after ionization events. Moreover, electrons can create further electrons through ionization. Accurate electron ionization cross sections are of high importance as ionization does not only contribute to the energy loss of electrons but also provides a source of secondary electrons.

---

#### Ionic projectiles

---

The standard cross sections for ion induced ionization, used in TRAX, rely on the Binary Encounter Approximation (BEA) [BoVr1970]. The cross sections can be calculated for all target and projectile combinations. For light and structureless projectiles it is reasonable to apply this theory [Kraemer1995]. The theory is based on a classic binary collision between a projectile with velocity  $v_p$  and a target electron with initial velocity  $v_{e-}$  and yields to a triple-differential cross section [KrKr1994]. The cross section is differential in the energy transfer  $\Delta E$ , the electron ejection angle  $\theta$  and the initial velocity of the target atom  $v_{e-}$  [KrKr1994]:

$$\frac{d^3\sigma}{d\Delta E d\Theta d v_{e-}} = F(\Delta E, v_p, v_{e-}, \theta) \quad (4.11)$$

By integration over the initial electron velocity distribution, the double-differential cross sections (DDCS) can be obtained. The DDCS are used to determine the energy and angular distribution of secondary electrons emitted in an ion induced ionization process. By integration over the distributions for energy transfer and ejection angles, a total cross section (TCS) is derived. The mean kinetic energy of the created secondary electrons is on the order of 100 eV [KrKr1994]. Binary collision kinematics determine the maximum energy transfer, which is maximal in forward scattering, where an electron obtains twice the velocity of the projectile ion. For an ion with 10 MeV/u, the produced electrons can have energies up to about 20 keV. A major deficiency of the BEA theory lies in the underestimation of backward emission at high energies [KrKr1994]. Besides, BEA is known to generally overestimate the emission of very low energy electrons. For ions incident on matter, an effective charge  $Z_{eff}$  according to Barkas [Barkas1963] is considered for heavy projectiles with nuclear charge  $Z_0$ :

$$Z_{eff} = Z_0 \left[ 1 - \exp \left( -125\beta Z_0^{-2/3} \right) \right] \quad (4.12)$$

with  $\beta = v/c$ ,  $v$  being the velocity of the ion and  $c$  being the speed of light. It is assumed that a charge equilibrium is reached after a few micrometer.

---



Another model implemented in TRAX is based on calculations according to Rudd [Rudd1988] with shell dependent empirical corrections. The Rudd approach relies on parameters fitted to experimental data and is therefore restricted to a few materials (He, Ne, Ar, Kr, H<sub>2</sub>, N<sub>2</sub>, O<sub>2</sub>, H<sub>2</sub>O, CO<sub>2</sub>, CH<sub>4</sub>, C<sub>3</sub>H<sub>8</sub>, C<sub>2</sub>H<sub>4</sub> and C). The Rudd model can be used to calculate improved ionization cross sections for ions incident on water which is necessary to reproduce ion ranges with high accuracy as needed for biological predictions.

---

### Electron projectiles

---

Total and single differential ionization cross sections for electrons incident on atomic or molecular targets can easily be calculated using a simple analytical formula which is based on the Binary-Encounter-Bethe (BEB) model [KiRu1994]. The advantages of the BEB model are, that it does not depend on empirical parameters, as the model is an ab initio theory. A simple analytical formula provides ionization cross sections for individual molecular orbitals and provides reliable cross sections at low and at high incident electron energies [KiRu1994]. BEB is mentioned as the method of choice for electron ionization in the NIST database [NIST]. It does not require substantial computational resources and can be used for multi-electron target atoms. The BEB model provides reliable cross sections not only for intermediate and high incident electron energies, but also for low energies down to the ionization threshold which is not given for most other theories [NIST]. Detailed information is needed to determine which electron shell has been ionized to simulate the production of Auger electrons in the relaxation process which is provided by the BEB model. TRAX classic uses cross sections for all atomic and molecular target materials, which are present in the target database, based on the BEB model. The BEB theory is based on Mott cross sections, considering the collision of two free electrons, and is combined with the high energy behaviour of the Born approximation [KiRu1994]. It is possible to compute the single differential cross section which is providing the energy distribution of ejected electrons as a function of the incident electron energy [KiRu1994]. This method is labeled binary-encounter-dipole (BED) model. By integration over the ejected electron energy, it is possible to calculate the total cross section [KiRu1994]. As the BED relies on optical oscillator strengths (OOSs) for individual orbitals, which are neither easily calculated nor measured, a simplified expression has been derived in the BEB model to directly provide total ionization cross sections [KiRu1994]. Necessary input parameters are the binding energy **B**, the orbital kinetic energy **U** and the electron occupation number **N**. The formula to obtain the contribution to the total ionization cross section from a certain electron shell is [KiRu1994]:

$$\sigma(T) = \frac{S}{t + (u + 1)/n} \cdot \left[ \frac{\ln(t)}{2} \left( 1 - \frac{1}{t^2} \right) + \left( 1 - \frac{1}{t} - \frac{\ln(t)}{t + 1} \right) \right] \quad (4.13)$$

**T** is the incident electron energy, **t**=**T/B**, **u**=**u/B** and **S** =  $4\pi\alpha_0^2 N(R/B)^2$  using the Bohr constant  $\alpha_0$ =5.2918 nm and the Rydberg constant **R**=13.6057 eV. The asymptotic behaviour predicted by the Born approximation for high projectile energies is **ln(t)/t** and is correctly provided by the BEB model [KiRu1994]. A relativistic extension of the BEB model has also been derived [Kim2000] and is considered in TRAX. As it does only affect the cross sections for incident electron energies at around 100 keV and higher, the importance for low energy electrons is low. The binding energies as well as the other parameters **U** and **N** are properties of the medium and can easily be derived from the ground state wave function. The cross sections

---

---

are strongly dependent on the values for the binding energy of the outermost orbitals. The maximum contribution to the total cross section comes from the outer electron shells as the cross section is increasing for decreasing binding energies. Summing over all orbital contributions leads to the total ionization cross section. For ionization, single differential cross sections (SDCS) are needed to determine the ejection energy of a secondary electron. The emission angles of primary and secondary electrons are sampled in TRAX according to Grosswendt and Waibel [GrWa1978, KrKr1994].

To obtain cross sections based on the BEB, the electron occupation of shells and shell-specific values of the binding energy and the kinetic energy are needed as input parameters. The information of shell-specific parameters for each atomic or molecular material is stored in external TRAX target files and the electron ionization cross sections are calculated using the parameters which have been read in at start-up of the code. In TRAX, as far as possible, experimental values are taken for the binding energies. Values for inner shells are widely known from experiments and values are usually taken from tables providing the information for a broad range of atomic materials [GwynWilliams, DanThomas, webelements]. For the outermost electron shell of each target material, the first ionization potential is chosen for which a collection of experimental values is given by [NIST]. For outer shells, just below the outermost shell, experimental values are not always provided. For these shells, target files in TRAX classic used the same binding energy as for the outermost electron shell. This approximation is extremely critical as the total ionization cross section depends crucially on correct values for the binding energy of the outermost electron shells. The impacts of this choice are discussed in the following. Within the framework of this thesis, binding energy values have been replaced which are summarized in table 4.9.

Experimental data exist for a few atomic target materials which could be used to validate the low-energy electron impact ionization cross sections. Furthermore, measured electron ionization cross sections are easily influenced by a variety of factors. Many experiments do not distinguish between different final states of the produced ions. The measured ionization can be a sum of single and multiple ionizations. Besides, experimental ionization cross sections can include contributions from excitation-autoionization while the BEB model does only provide direct ionization cross sections. Therefore, comparison with BEB cross sections have to be made with care. The impact of this neglect in the BEB model and ways to account for this additional source of secondary electrons is explained for certain individual atomic materials in [KiDe2002, KiSt2001].

Brook et al. [Brook1978] has measured the electron impact ionization of carbon using target atoms which have been generated by neutralizing positive ions through charge exchange. In a publication of the author of the BEB model [KiDe2002], the application of calculated ab initio electron ionization cross sections based on this model are discussed in the case of carbon and compared with the experimental data of Brook et al.. Comparison of the cross sections mentioned in this paper with TRAX calculations which are based on the same model revealed differences due to a different choice of binding energy values. The BEB is extremely sensitive on the choice of binding energy values and differences of a few electron Volts in binding energies have a huge impact on the resulting cross sections.

As experimentally determined ionization cross sections might include multiple and indirect ionizations, they can be higher than calculated cross sections for direct ionization but should not be lower. If calculations overestimate experimental ionization cross sections, as far as measurements are correctly normalized, this can be a hint for unsuitable input parameters. TRAX classic

---

cross sections for electron impact ionization of carbon have been higher than the experimental data from Brook et al. [Brook1978] which is suspicious. Besides, in the publication dealing explicitly with carbon ionization [KiDe2002], cross sections based on the BEB model using a calculated set of input parameters resulted in much lower cross sections. The differences can be seen in Fig. 4.16. In the case of carbon, the binding energy for the 2s electron shell was

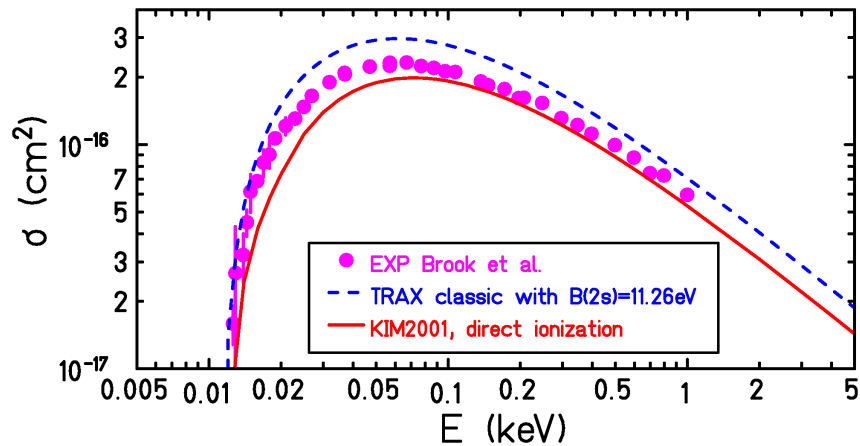
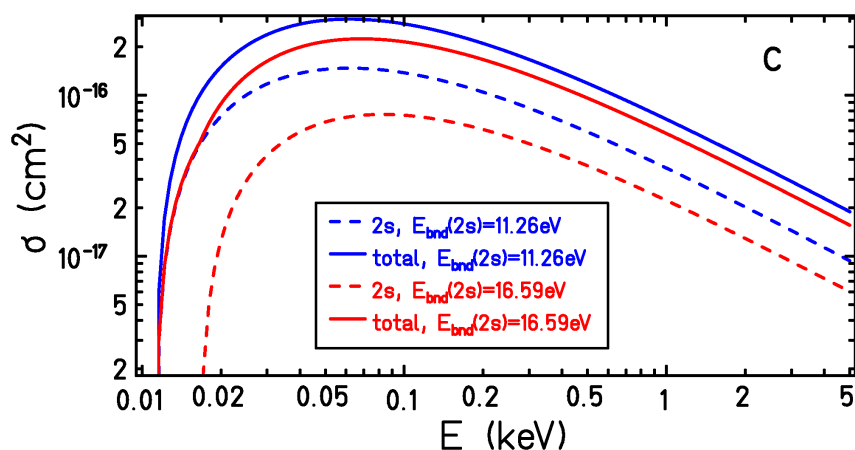


**Figure 4.16:** Comparison of cross sections for electron induced ionization of carbon. Purple dots represent the experimental data from Brook et al. [Brook1978]. The dashed blue line shows TRAX classic direct ionization cross sections according to the theory from [KiRu1994]. The same values have been taken for the binding energies of the 2s and 2p shell. The red line shows results according to [KiDe2002] using the same theoretical model to obtain direct ionization cross sections while deviations from experimental data are due to contributions from auto-ionization. The difference lies only in the choice of the input parameters, especially due to a different binding energy for the 2s shell. TRAX classic cross sections using the same binding energy values for the 2s and the 2p shell overestimate the experimental data.

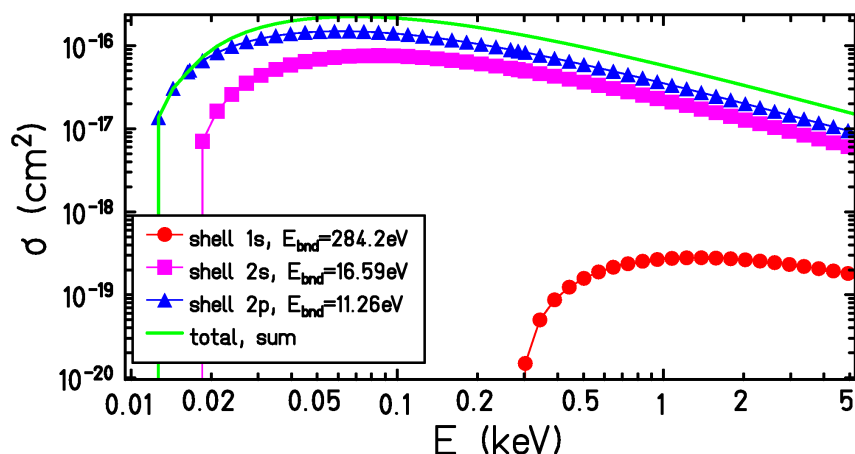
not available in the TRAX classic targetfile and so has been approximated to be equal to the binding energy for the 2p shell. In [KiDe2002] these values are different. As a binding energy value for the 2s shell of carbon is now available in one of the used binding energy data compilations [DanThomas], the value of 11.26 eV has been replaced for a value of 16.59 eV which is also mentioned in a recent paper [Simonetti2007]. Impacts of this choice on the resulting ionization cross sections are shown in figure 4.17.

Fig. 4.18 shows the relative contributions from the different electron shells to the total ionization cross section for electrons incident on carbon.

With the modified more realistic binding energy for the carbon 2s shell, TRAX calculations using the BEB resulted in a reduced ionization cross section which is not overestimating experimental results by Brook et al. [Brook1978]. The comparison can be seen in Fig. 4.19. The experimental data of Brook contained contributions from excitation-autoionization. As cross sections based on BEB do not include indirect ionization, these contributions have to be added to get the total ionization cross section that can be compared with experimental data [KiDe2002]. For carbon, only 2s-2p excitations contribute significantly to excitation-autoionization [KiDe2002]. In the publication by Kim et al. about ionization of carbon [KiDe2002], the transitions from the ground state to the  $2s2p^3\ ^3S$  and  $2s2p^3\ ^1D$  state are considered for contributions. For a compar-



**Figure 4.17:** Differences in total and shell dependent electron ionization cross sections for carbon due to different values for the 2s binding energy.



**Figure 4.18:** Shell dependent carbon cross sections showing the relative contribution of the electronic shells to the total ionization cross section. The total ionization cross section is dominated by contributions from the outermost shells.

ison of the cross sections used in TRAX, these two excitation channels, for which cross sections have been derived according to Suno [SuKa2006], have been added to the ionization cross sections. Fig. 4.19 shows the comparison of TRAX cross sections and experimental data. It can be seen that for carbon, excitation-autoionization does barely contribute to the total ionization cross section. It should be noted, that for the for the TRAX calculations in Fig. 4.19 a different set of parameters for **B** and **U** values has been used than in [KiDe2002]. TRAX calculations are based on experimental values for **B**, while Kim et al. have used a different theoretical set of parameters. As ionization cross sections for the parameters used in TRAX match experimental data, neglecting further handling of excitation-autoionization can therefore be justified.

The example of carbon shows that replicating binding energy values from the outermost electron shell to the second shell from the outside can be critical. As the information of shell-specific parameters for each atomic or molecular material is stored in external TRAX target files, replacing binding energies with more accurate values can easily be done. Improved values have been

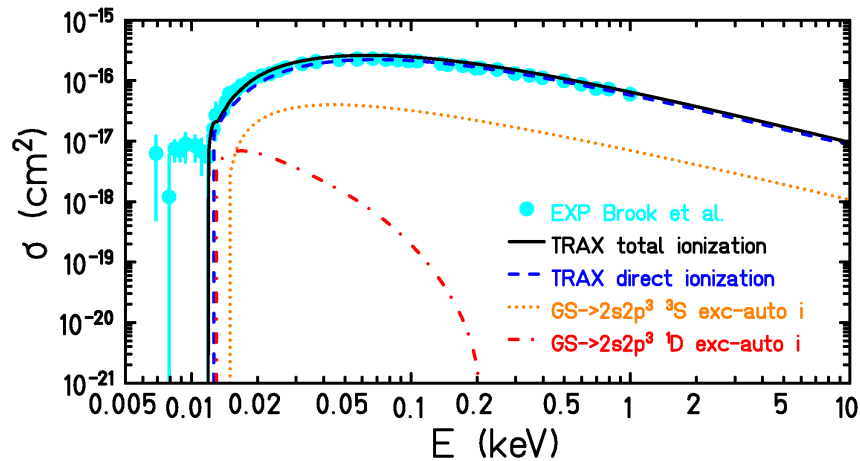


**Figure 4.19:** Comparison of cross sections for electron induced ionization of carbon. Lightblue dots represent the experimental data from Brook et al. [Brook1978]. The black solid line represents the total ionization from TRAX including direct ionization cross sections and two excitation channels leading to auto-ionization. The dashed blue line shows TRAX direct ionization cross sections according to [KiRu1994]. The dashed orange and red lines show TRAX excitation cross sections for two channels which were calculated from collision strengths according to [SuKa2006].

taken from [DanThomas] as far as available. If not otherwise provided, theoretical binding energy values from the EADL database [PeCu1991] have been considered. For Au, where the same binding energy has been taken for the  $5d_{3/2}$  and  $5d_{5/2}$  shells, the "classic" values have also been replaced by values from EADL [PeCu1991]. An overview about the changes in binding energy values is given in table 4.9.

Figures 4.20, 4.21 and 4.22 show exemplarily the effects of the changed values for other materials of interest, i.e. Ni, Ag and Au.

For aluminium, experimental data for electron induced ionization exists as well. But comparisons with calculations for aluminium is difficult as excitation-autoionization of the  $3s3p^2 \ ^2S$  and  $\ ^2P$  terms is of high importance because the contribution to total ionization is almost as high as from direct ionization of  $3s$  and  $3p$  electrons [KiDe2002]. For open-shell atoms, indirect ionization can be possible, e.g. by excitation-autoionization [KiDe2002]. Excitations from inner shells to the outermost orbital (in case it is not already fully occupied) can produce excited states below or above the first ionization threshold. If the excited state lies above, it either decays by emission of a photon or by auto-ionization while ejecting an electron. The cross sections for excitation-autoionization tend to be large in case of electron transitions from an inner orbital with the same principal quantum number as the outermost orbital [KiDe2002].

TRAX does not account for excitation-autoionization yet. In principle it would be possible, as the input cross sections for excitation can be provided separately for each excitation channel. The problem lies in the description of the kinetic energy for the secondary electrons to be emitted via autoionization. If an excitation occurs in the simulation process, the energy needed for the transition is deposited locally. While the energy needed for an excitation transition that will lead to autoionization will be only slightly higher than the ionization threshold, released electrons will have very low energies and therefore are supposed to be stopped immediately. For

element	subshell	previous $E_{bnd}$	new $E_{bnd}$	source
C	2s	11.26 eV = $E_{bnd}(2p)$	16.59 eV	[DanThomas]
Al	3s	6.00 eV = $E_{bnd}(3p_{1/2})$	10.62 eV	[DanThomas]
Fe	3d <sub>5/2</sub>	7.9 eV = $E_{bnd}(4s)$	12.91 eV	EADL [PeCu1991]
Fe	3d <sub>3/2</sub>	7.9 eV = $E_{bnd}(4s)$	12.74 eV	EADL [PeCu1991]
Ni	3d <sub>5/2</sub>	7.64 eV = $E_{bnd}(4s)$	14.66 eV	EADL [PeCu1991]
Ni	3d <sub>3/2</sub>	7.64 eV = $E_{bnd}(4s)$	14.92 eV	EADL [PeCu1991]
Ag	4d <sub>3/2</sub>	7.58 eV = $E_{bnd}(5s)$	11.86 eV	EADL [PeCu1991]
Ag	4d <sub>5/2</sub>	7.58 eV = $E_{bnd}(5s)$	12.47 eV	EADL [PeCu1991]
Au	5d <sub>3/2</sub>	11.66 eV = $E_{bnd}(5d)$	12.16 eV	EADL [PeCu1991]
Au	5d <sub>5/2</sub>	11.66 eV = $E_{bnd}(5d)$	10.46 eV	EADL [PeCu1991]

**Table 4.9:** Values for binding energies with respect to TRAX classic.

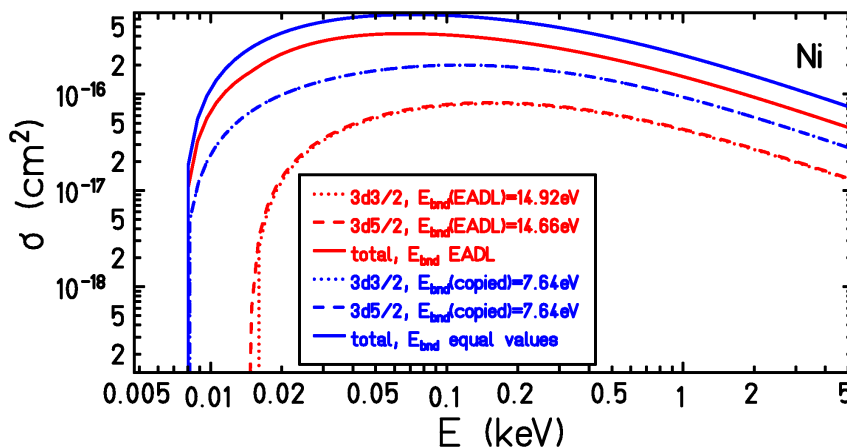


**Figure 4.20:** Differences in total and shell dependent electron ionization cross section for nickel and the 3d shells due to different values for the binding energies. Improved binding energy values reduce total ionization cross sections.

the two excitation transitions considered to be leading to auto-ionization in carbon, e.g., energy transfers are 12.2 eV and 13.1 eV, while the ionization threshold lies at 11.26 eV. Auto-ionized electrons therefore are expected to have very low energies. Neglecting the energy transfer to an autoionized electron and rather directly considering a local energy deposition by excitation should therefore be a suitable approximation. Therefore, the neglect of the explicit handling of excitation-autoionization is seen to be uncritical.

Experimental data for electron induced ionization of aluminium is provided by Freund et al. [FrWe1990]. Comparisons with theoretical cross sections are shown in [KiSt2001] where adding cross sections for the autoionizing excitation-transitions to the BEB ionization cross sections reproduced experimental results.

Very few experimental data for single ionization of neutral target atoms exist for comparison with theoretical ionization cross sections. Even though validation through experimental data is limited, electron ionization cross sections based on the BEB are seen to be the best possible

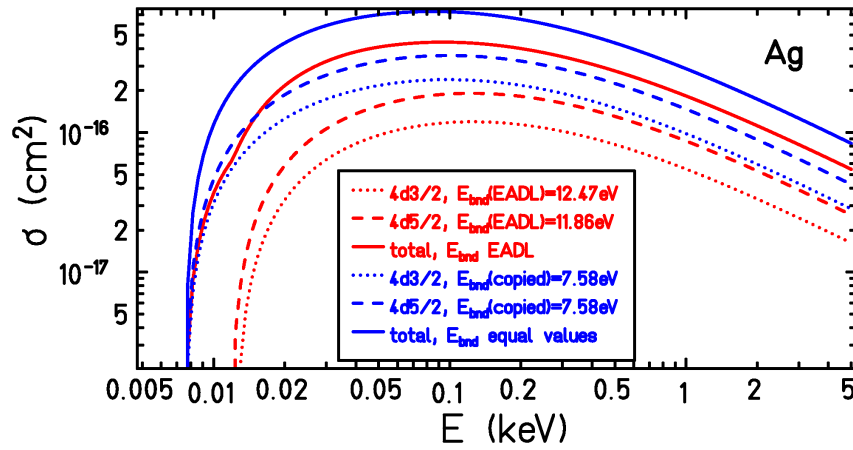


**Figure 4.21:** Differences in total and shell dependent electron ionization cross section for silver and the 4d shells due to different values for the binding energies.

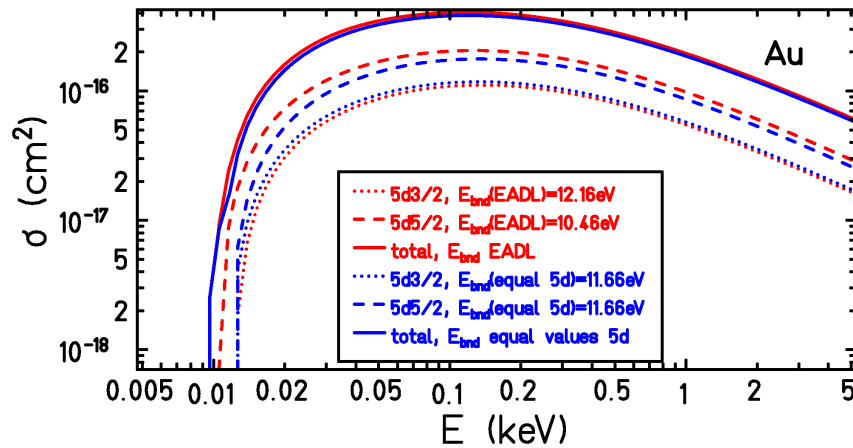


**Figure 4.22:** Minor differences in total and shell dependent electron ionization cross section for gold and the 5d shells due to different values for the binding energies.

choice to describe the effect for low energies down to the ionization threshold. In contrast to other theoretical approaches which are relying on the first Born approximation, the BEB model does also consider higher order effects like the distortion of the incident wave and the polarization of the target charge distribution [KiDe2002]. The BEB does contain elements of the first Born approximation but includes higher order effects by replacing the incident energy for a shifted value (considering binding and kinetic energy of the target electrons) [KiDe2002]. An uncertainty lies in the choice of binding energy values. These values have been chosen as accurate as possible. For further validation of the ionization cross section, experimental data for the electron stopping power can be used. Together with electron induced excitation, ionization makes up almost completely the total electron stopping power at low energies (where only electronic stopping plays a role). From the given energy losses per excitation channels, and the energy losses per ionization (binding energy plus kinetic energy of released secondary electrons), a stopping power or unrestricted LET value can be calculated. This procedure is used as a validation for the used excitation and ionization cross sections and shown in subsection 5.1.1.

---

In the high energy region above electron energies of about 1-10 keV, the stopping power values are known. As excitations dominate the stopping power at low energies and ionization at high energies, a mismatching stopping power at high energies can be an indication for inaccurate ionization cross sections due to inaccurate input parameters. This has been the case, e.g. for nickel, where a change in binding energies solved the problem of overestimating experimentally determined stopping powers at 10 keV. The effect can be seen in Fig. 5.2.

---

#### 4.2.4 Elastic scattering

---

Electrons or ions undergoing elastic scattering suffer no energy loss. Although elastic scattering does not contribute to radiation damage, it is important to be considered as it is responsible for the spatial diffusion in matter. Besides, elastic scattering for electrons is important to obtain correct backscattering and transmission factors.

---

##### Screened Rutherford cross sections

---

Elastic scattering for electrons is often described by Rutherford cross sections with screening corrections [Molière1948, Berger1963, GrWa1978]. This is a conventional method for elastic scattering and used as built-in standard in TRAX classic and is available for all kinds of target materials. For some materials like water, empirical corrections are used to improve these cross sections at low energies.

For elastic scattering, differential cross sections  $d\sigma/d\Omega(E, \theta)$  are needed to determine the angular distribution. The differential cross section for elastic scattering of a charged particle by a nucleus of charge  $Z \cdot e$  using the screened Rutherford approach is [Berger1963]:

$$\frac{d\sigma}{d\Omega}(E, \theta) = \frac{Z^2 \cdot e^4}{4 \cdot E^2(1 - \cos\theta + 2\eta)^2} \quad (4.14)$$

For electrons, the factor  $Z^2$  should be replaced by  $Z \cdot (Z + 1)$  using a correction to Molière's theory suggested by [Fano1954].

$\eta$  is a screening parameter which considers the screening of the nuclear charge by the orbital electrons [Berger1963]. This parameter can be derived from the theory of Molière [Berger1963]:

$$\eta = 1/4 \cdot \chi_a^2 = 1/4 \cdot a \cdot Z^{2/3} \left[ 1.13 + 3.76 \left( \frac{Z}{137 \cdot \beta} \right)^2 \right] \quad (4.15)$$

$a = 6.8 \cdot 10^{-5}$  for electrons and  $a = 6.8 \cdot 10^{-5} \cdot (m/M)^2$  for protons, with  $m$  being the (resting) mass of an electron and  $M$  the mass of the proton projectile [Berger1963]. Within this work, TRAX cross sections have been extended to account for the elastic scattering of ion projectiles which is often neglected in track structure MC codes. The implementation and results due to this interaction will be explained in chapter 6 of this thesis.

For some materials, semi-empirical adaptations for this screening parameter exist, varying  $\eta_c$  in the description of  $\eta$ , with velocity  $\beta = v/c$ :

$$\eta = \eta_c \cdot 1.7 \cdot 10^{-5} \cdot Z^{2/3} \cdot \left( \frac{1}{\beta^2} - 1 \right) \quad (4.16)$$


---



The method of varying  $\eta_c$  for a semi-empirical screening parameter is described in [Uehera1992], where for electrons with energies below 50 keV incident on water  $\eta_c$  is set to 1.198. For higher energies, the standard description of [Berger1963] is used:

$$\eta_c = 1.13 + 3.76 \left( \frac{Z \cdot \beta}{137} \right)^2 \quad (4.17)$$

By integration of the differential cross section over the full solid angle ( $d\Omega = 2\pi \sin(\theta) d\theta$ ), a total cross section can be derived:

$$\sigma(E) = \int 2 \cdot \pi \cdot \sin(\theta) \left( \frac{d\sigma}{d\Omega} \right) d\theta = \frac{Z^2 \cdot e^4}{4 \cdot E^2} \cdot \frac{\pi}{\eta(\eta + 1)} \quad (4.18)$$

For high Z materials, screened Rutherford differential cross sections (SRDCS) are usually restricted to medium ( $E > 500$  eV) and high ( $E > \text{few keV}$ ) energy regions, where the first Born approximation is valid. But for low Z materials they can be used also at lower energies. To check the validity of the Born approximation, the condition  $v/c \gg Z/137$  should be applied [Liljequist2012]. The condition gives  $E \gg 200$  eV for Be ( $Z=4$ ), but it has been found that the SRDCS is still usable down to about 100 eV. So as a first reasonable approach, for electrons incident on low Z-materials like carbon, the elastic scattering can be described by Rutherford cross sections with screening corrections, which is a conventional method for track structure calculations. The screening correction is obtained by applying the Born approximation to the Wenzel model for the atomic scattering potential [Liljequist2012]. Screened Rutherford cross sections e.g. ignore the spin of the incident projectile and therefore subsequent polarization effects.

The accuracy of the screened Rutherford cross sections is also connected to the choice of the screening parameter. Various approaches exist to improve the applicability of the screened Rutherford cross sections by changing the screening parameter to semi-empirical values [Nigam1959, Joy1995a, KyEm2013].

For water and electron energies above 500 eV, Rutherford cross sections can be applied [KrKr1994]. At lower energies, screened Rutherford cross sections underestimate backward scattering. Therefore, experimental data from experiments for H<sub>2</sub>O (and for H<sub>2</sub> and O<sub>2</sub> where no water data has been available) is used to replace these cross sections. Elastic scattering on molecules is treated using the additivity rule. Therefore, cross sections for water can be obtained by summing hydrogen and oxygen contributions.  $\sigma_{H_2O} = \sigma_{H_2} + 1/2 \sigma_{O_2}$ . Theoretical cross sections are replaced by a polynomial function which has been fitted to experimental data [KrKr1994].

TRAX classic has been used mainly for simulations in low Z target materials like carbon and water for which cross sections for elastic electron scattering could have been described using screened Rutherford calculations. However, simulations for higher Z materials have in principle been possible for TRAX classic, but were limited in precision due to available cross sections. For high Z materials, the screened Rutherford cross sections are less suitable for low energetic electrons and should be replaced by cross sections based on a more suitable model.

---

### Cross sections based on partial wave analysis

---

As a more sophisticated method, cross sections can be provided using partial wave analysis (PWA) or the partial wave expansion method (PWEM). These cross sections are often denoted as Mott cross sections. As far as the scattering potential is correctly described and

---

---

the summation over all terms up to infinity is provided, cross sections based on PWA should be in principle exact [Liljequist2012]. PWA based cross sections should provide a better reproduction of backscattering at low energies and for medium to high Z (Z: atomic number) materials. In the framework of this thesis, cross sections relying on PWA from the NIST ELAST database [JaSa2010] have been assessed for many target materials of interest. Considered in the framework of this thesis are cross sections from the ELAST code version 3.2. The ELAST input is described in the following sentences. Walker [Walker1971] describes the method of relativistic Dirac partial wave analysis which is the basis for the calculations. Further, a scattering and an exchange potential is needed to obtain the cross sections. The scattering potential is provided by self-consistent Dirac-Hartree-Fock electron densities for free atoms using the approach from [Desclaux1977]. The local exchange potential which is used for ELAST has been provided by Furness and McCarthy [FuMc1973]. An exchange potential takes into account that the incident electron is not distinguishable from the atomic electrons of the target [Liljequist2012]. The accuracy of the cross sections provided by ELAST is discussed in [JaSa2004]. Resulting cross sections are given for electron energies between 50 eV and 20 keV (in steps of 1 eV) with differential cross sections (in angle) for  $0^\circ - 180^\circ$  in steps of  $1^\circ$ . An extension allows to obtain different cross sections for energies above 20 keV up to 300 keV.

Within this thesis, full sets of differential cross sections for elastic scattering have been extracted from ELAST and formatted to be used as input files with TRAX. The code has been extended to assure correct read-in of the differential cross sections as well as calculation of total cross sections by integration over all possible scattering angles.

---

### Comparison of models

---

The cross sections from ELAST are considered to be more accurate for high Z materials and show significant differences to screened Rutherford cross sections, especially at low energies. To estimate possible errors of screened Rutherford cross sections and to observe the impact of changing the elastic scattering model in TRAX, both TCS and SDCS have been compared for low Z (carbon,  $Z=6$  and aluminium,  $Z=13$ ), medium Z (Fe,  $Z=26$  and Ni,  $Z=28$ ) as well as for high Z materials (Ag,  $Z=47$  and Au,  $Z=79$ ). The comparisons for the TCS can be seen in Fig. 4.23.

From the comparison of the TCS (Fig. 4.23) one can estimate the applicability of the screened Rutherford cross sections. As carbon is a very low Z material, screened Rutherford cross sections should be suitable even at low energies. Only minor deviations exist between the TCS based on screened Rutherford calculations or PWA. With increasing Z values, screened Rutherford cross sections differ a lot from those based on PWA, especially at low energies. As Au is a very high Z material, screened Rutherford cross sections are less suitable at low energies. For Au and incident energies of around 100 eV, the difference between the TCS of the two approaches is a factor of about 7. At higher energies, the cross sections for Au from the two models are approaching and eventually become equal at around 20 keV. As the cross section model for the TCS based on PWA changes at 20 keV, it is not clear which cross sections are more accurate at higher energies, after the intersection point of both TCS. Cross sections based on screened Rutherford calculations are supposed to be accurate at higher energies. Besides, even with the changed model, ELAST does only provide elastic scattering cross sections up to 300 keV. Therefore, in cases where cross sections for higher electron energies are needed for TRAX calculations, the intersection point of the elastic scattering TCS from both models has been used to combine cross sections relying on PWA for lower energies with cross sections relying on screened Rutherford

---

---

calculations for higher energies. This method had to be applied as the TCS for high Z materials differed largely below and above this intersection point. The intersection point of the TCS from both methods has been chosen at 2.7 keV for Fe, 7.4 keV for Ag, 7.4 keV for Gd, 15 keV for Pt and 20 keV for Au. As no cross sections from ELAST have been available at energies below 50 eV, and the TCS seem to reach a maximum at these energies (according to Fig. 4.23), constant SDCS and TCS have been assumed for energies below 50 eV.

The main difference between cross sections relying on screened Rutherford approximations or PWA, besides their absolute TCS values, lies in the shape of the differential cross sections. Significant differences are expected for the SDCS also for low Z materials. Cross sections based on PWA show details of the elastic scattering interaction which is resulting in lobes at certain angles. More or less pronounced lobes can be seen, as the scattering probability is enhanced at these angles. The lower the electron energy, the stronger this feature is. The number and position of these lobes depends on electron energy and the target material [VaNi1984]. Figure 4.24 shows SDCS for electrons incident on carbon while for cross sections based on PWA an enhanced scattering cross section is visible at around  $180^\circ$  for an incident energy of 50 eV. At higher energies, differences between screened Rutherford cross sections and those based on PWA vanish. At energies above 1 keV there are no significant differences which shows that for low Z materials, screened Rutherford cross sections can be used.

For higher Z materials, differences in the SDCS are also visible at higher energies. With increasing Z, the lobes at angles with enhanced scattering probabilities become more dominant at low energies. Fig. 4.25 shows the SDCS for electrons incident on nickel which has been chosen as an intermediate Z example. Fig. 4.26 shows the SDCS for electrons on gold, chosen as a high Z example. For such high Z materials, obvious differences in the SDCS are visible even at energies above 1 keV.

To validate the applicability of elastic scattering cross sections, simulations for the electron backscattering coefficient can be used. A correct description of the cross sections for elastic scattering is mandatory to reproduce experimentally determined backscattering coefficients. Simulations including the new extended cross sections for inelastic electron interactions but the previous elastic scattering cross sections based on the screened Rutherford approach, are supposed to be failing to describe the electron backscattering coefficients for high Z materials. Exactly this behaviour can be found in section 5.1.2 where TRAX with its current set of inelastic scattering cross sections and both methods for elastic scattering has been used to reproduce experimental data.

---

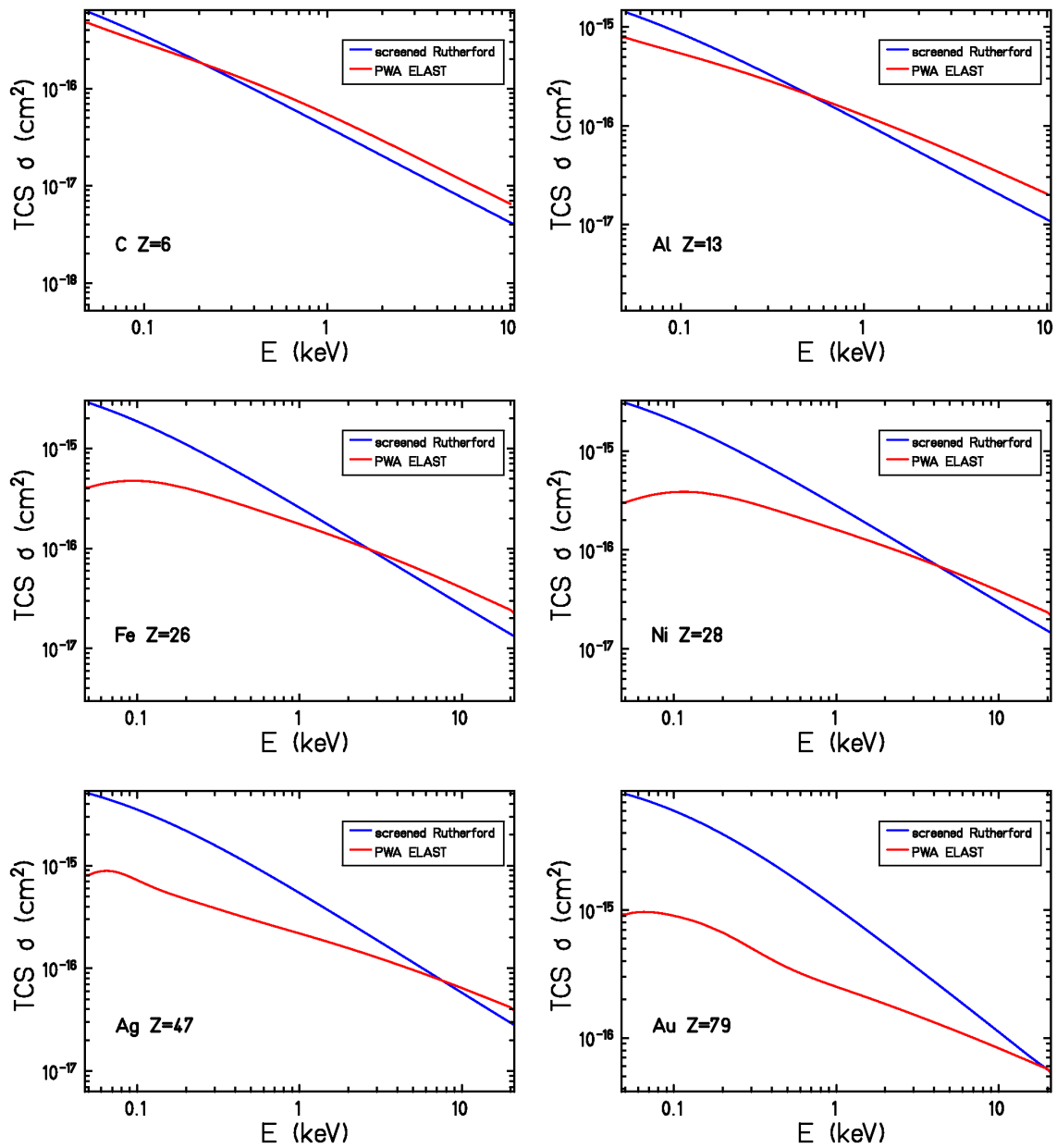


**Figure 4.23:** Total cross sections for elastic scattering of electrons incident on carbon, aluminium, iron, nickel, silver and gold. Screened Rutherford cross sections are compared with cross sections based on partial wave analysis which have been extracted from the NIST ELAST database.

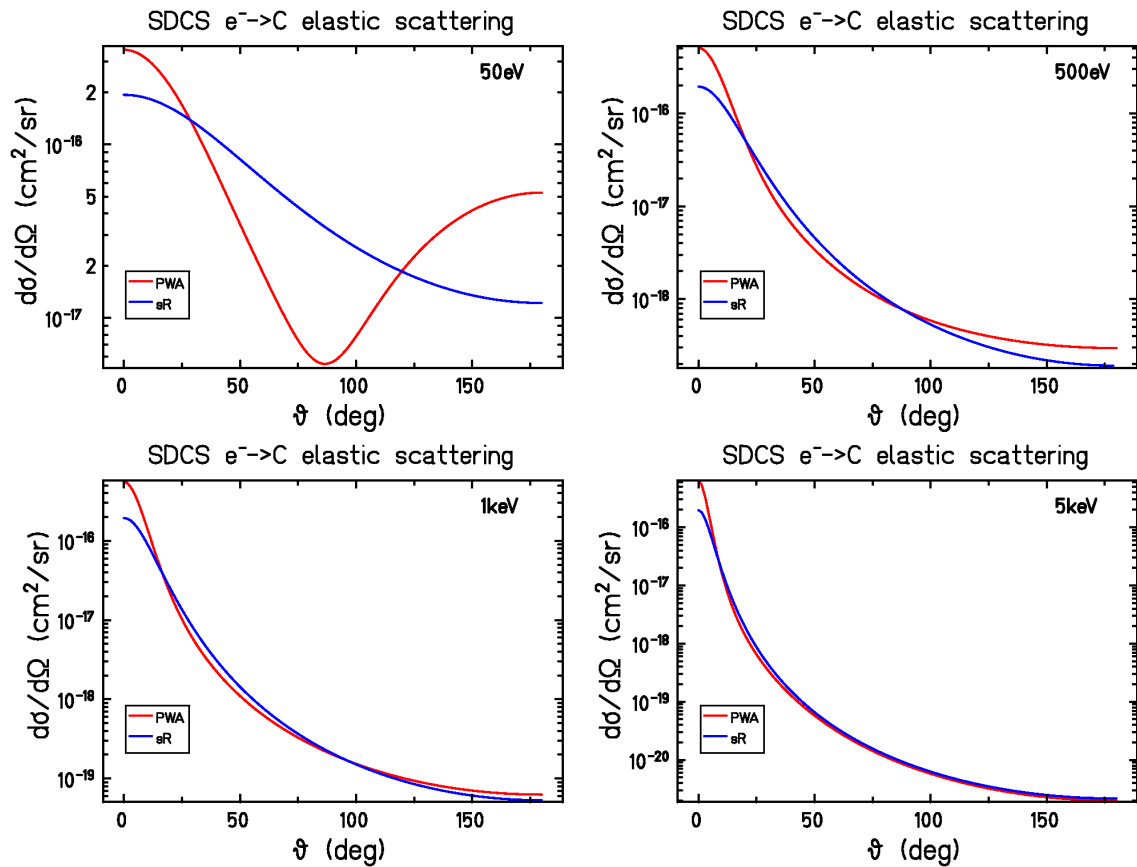


**Figure 4.24:** Differential cross sections for elastic scattering of electrons incident on carbon for four different energies (50 eV, 500 eV, 1 keV and 5 keV). Screened Rutherford cross sections show significant differences at 50 eV from cross sections based on partial wave analysis. At higher energies, the differences start to vanish and both differential cross sections are approaching each other.

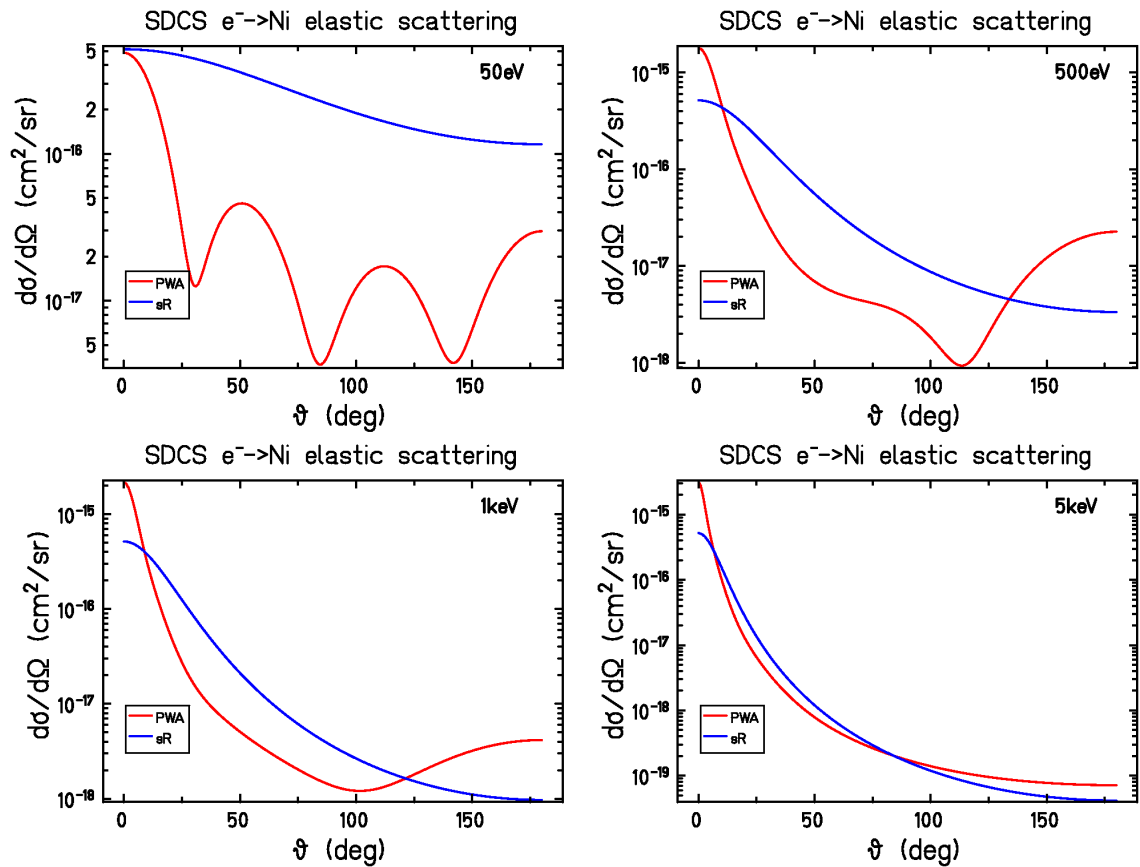


**Figure 4.25:** Differential cross sections for elastic scattering of electrons incident on nickel for four different energies (50 eV, 500 eV, 1 keV and 5 keV). Screened Rutherford cross sections show significant differences at low energies from cross sections based on partial wave analysis. At higher energies above 1 keV, the differences start to vanish and both differential cross sections are approaching each other.

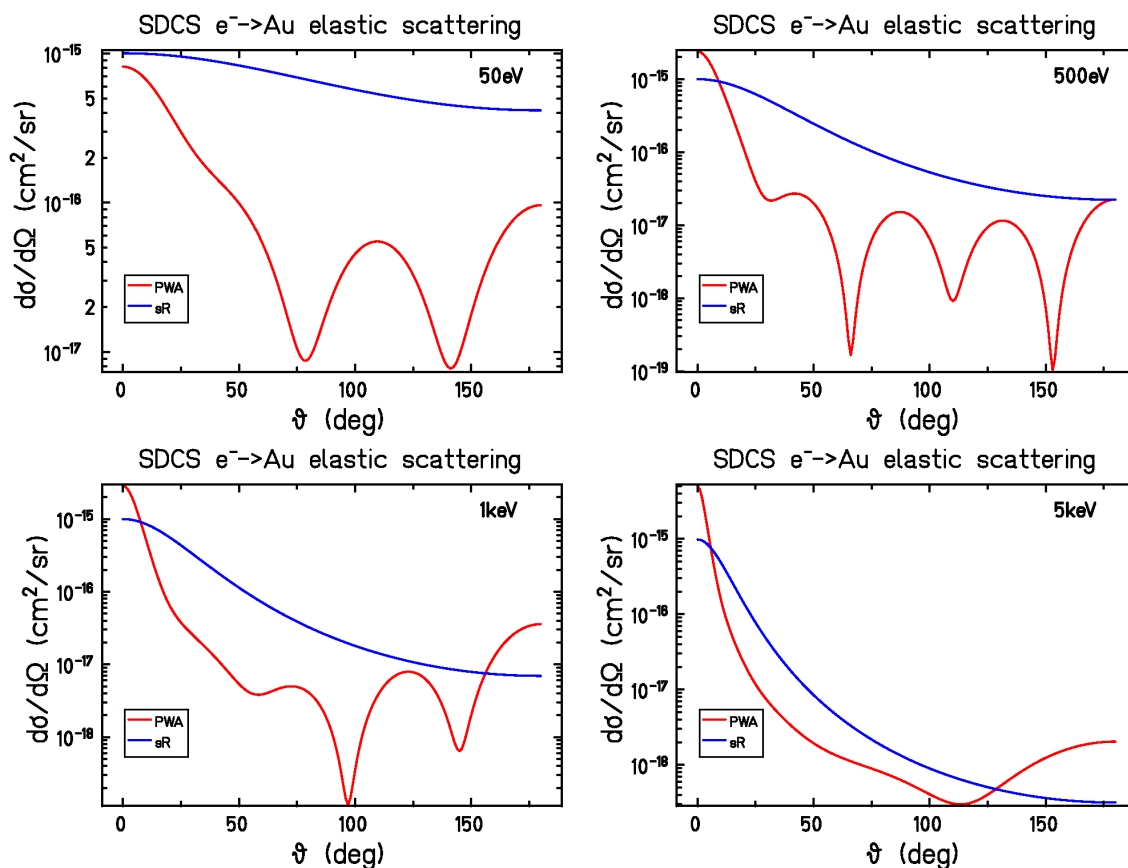


**Figure 4.26:** Differential cross sections for elastic scattering of electrons incident on gold for four different energies (50 eV, 500 eV, 1 keV and 5 keV). Screened Rutherford cross sections differ a lot from those based on partial wave analysis as they show no structure. Especially at low energies, partial wave analysis includes resonance effects, leading to an enhanced cross section at certain angles. At higher energies, these lobes flatten and the shapes of both differential cross sections are approaching each other. But even at energies as high as 5 keV, for a very high Z material like gold, significant differences persist.

---

### 4.3 Auger electrons

---

One major extension of the TRAX code that has been performed in the framework of this thesis has been the handling of the Auger effect which is mandatory for a correct description of low energy electron transport. As Auger electrons usually have energies below 1 keV, they have a crucial impact on secondary electron spectra (low-energy yields) as well as on microscopic or nanoscopic damage. In measured electron spectra, e.g. from the Toroid [Lineva2009] experiment, Auger electrons can be seen as a peak with a relatively sharp edge at the initial Auger electron energy and a longer tail towards lower energies. The tail is a result from Auger electrons undergoing inelastic interactions, losing energy while travelling through the target. To correctly describe the emission and transport of electrons and to reproduce corresponding experimental data with TRAX, Auger electrons cannot be neglected.

Auger electrons are low-energy electrons which can be emitted during the relaxation after an ionization event took place. If an inner shell of an atom is ionized, a secondary electron is emitted and creates a vacancy. The created vacancy can be filled with another electron from an upper shell of the ionized atom. The excess energy can then either be transferred to a photon or to another electron that will be emitted. The latter is called an Auger electron. The Auger process therefore produces a secondary electron additionally to that one released by the ionization process itself. Auger electrons are emitted isotropically. Besides, they have a discrete energy which is directly linked to the difference in binding energies of the involved shells. Auger electrons can be distinguished by the shells involved. A KL1L2 Auger electron is an electron, where the K shell has been ionized first and the vacancy has then been filled by an electron from the L1 shell. An electron from the L2-shell is then emitted as an Auger electron and carries away excess energy. Its kinetic energy is the difference in binding energies of the involved shells:  $E_{kin,KL1L2} = |E_K| - |E_{L1}| - |E_{L2}|$ . The process is illustrated in figure 4.27.

As the energy of an Auger electron depends on the difference in binding energies, which are a property of the target material, it is possible to identify materials through characteristic Auger electrons in their electron spectra.

The fluorescence yield  $\omega(Z)$  describes the probability to emit a photon after ionization of a certain electron shell. The fluorescence yield is dependent on  $Z$  and dependent on the electron shell. For the K-shell, the fluorescence yield depends on the atomic number approximately as  $Z^4$  [Wentzel1927, Bambynek1972]. Here, Auger emission competes with photon production and the probability to emit an Auger electron rather than a photon is  $1 - \omega(Z)$ . For low  $Z$  materials, the probability to create an Auger electron after K-shell ionization is high and photon production can almost be neglected. Probabilities to emit a photon rather than an Auger electron are only 0.2% for carbon and 0.58% for oxygen [Bambynek1972]. The fluorescence yield after K-shell ionization increases for high  $Z$ -materials and reaches about 97% for gold. For the L-shells and above, dependencies are different. A review about fluorescence yield dependencies for various shells is given by Hubbel et al. [Hubbel1994]. Even though the proportionality to  $Z^4$  is approximately valid also for  $\omega$  of the L and M shells, the absolute value of the fluorescence yield is much lower than for the K shell. For the L-shell and atoms with  $11 < Z < 36$ , the fluorescence yield is supposed to be about  $2 \cdot 10^{-8} \cdot Z^4$  [Hubbel1994], while for the M-shell and  $76 < Z < 92$ , the fluorescence yield can be parametrized as  $1.29 \cdot 10^{-9} \cdot (Z - 13)^4$ . For outer shells, absolute values of fluorescence yields decrease rapidly. Even for high  $Z$  materials, fluorescence yields for shells other than the K shell can therefore be much lower than the Auger electron

---



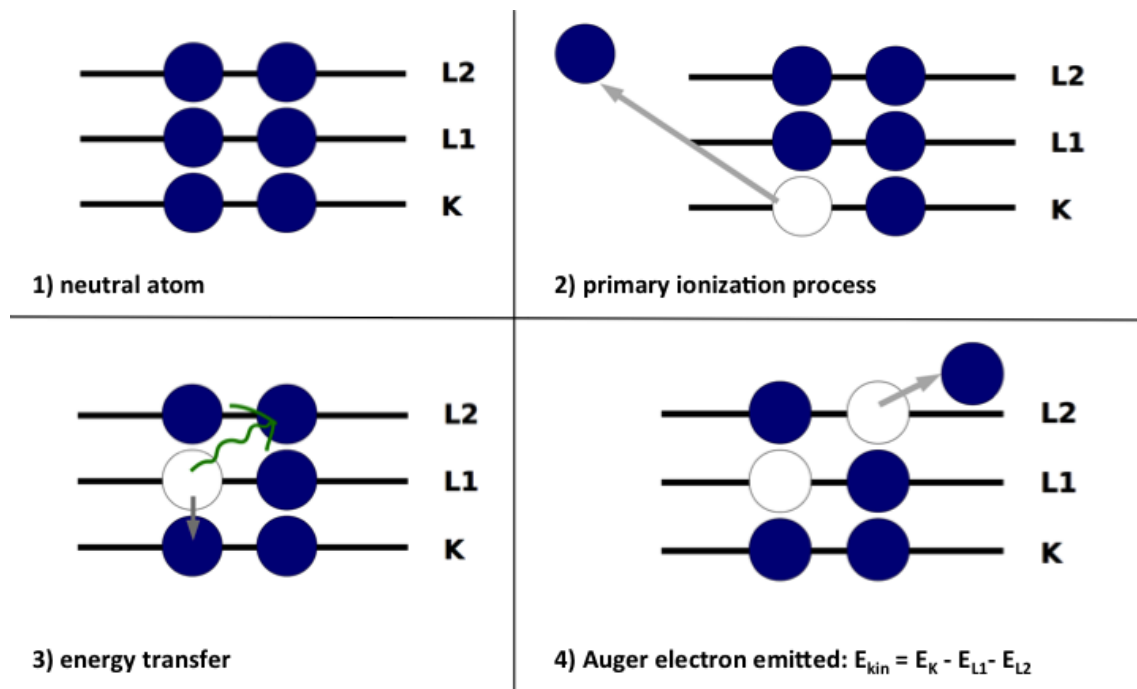


**Figure 4.27:** The Auger process is shown schematically for a K-L1-L2 transition. A neutral atom suffers a primary ionization event in the K-shell. An electron from the L1-shell fills the hole in the K-shell and energy is transferred to another electron in the L2-shell which is then ejected as an Auger electron.

probabilities. The average fluorescence yield for the L-shell of gold, e.g., is about 30%, which means that the probability to emit an Auger electron is 70% for the L shell. For outer shells, Auger electron emission probabilities are increasing and reach almost 100% for the outmost shells. Therefore it is possible to obtain a high number of emitted Auger electrons even for high Z materials where the K-shell fluorescence yield is high. Besides, outer shells are much more likely to be ionized than the K-shell which can be seen by consideration of shell dependent ionization cross sections according to [KiRu1994].

For high Z materials with complex electronic shells there is also the possibility of emission of Auger electron cascades (release of more than one Auger electron after one primary ionization event) as many electrons are present that can fill up holes in lower lying shells. If an inner shell of a high Z atom is ionized, many different Auger electron transitions are possible and for one primary ionization event, many Auger electrons can be released which can easily be more than 10. However, as inner shells are more difficult to be ionized by electron or ion projectiles, the total contribution of these "multiple" Auger electrons to all secondary electrons is expected to be rather small.

Within the framework of this thesis, the handling of Auger electrons and cascades in TRAX has been developed as a new feature. For the probabilities of different Auger electron transitions and shell dependent fluorescent yields, data has been compiled from the Sigma Database of BNL National Nuclear Database [BNL] which uses data from the Livermore Evaluated Atomic Data Library [PeCu1991]. For H<sub>2</sub>O, experimentally determined Auger transition probabilities after K-shell ionization have been considered according to [Siegbahn1975]. These data have been

---

included in TRAX target files. Among other specific atomic information like density and shell structure information, Auger transition probabilities and fluorescence yields are now included in the basic target material information.

The production of Auger electrons is not directly dependent on projectile energies. The Auger process occurs after ionization events and it does depend on the ionized shell of a certain target material. Therefore, to handle the Auger effect, the determination of the electron shells which are ionized is a necessary prerequisite. The Auger effect is handled in the TRAX simulation in the sampling function for ionization. The previous version of the function calculated the energy and angle of the emitted secondary electron and the change in energy and direction of the primary particle which caused the ionization. In the new version, possible Auger electrons are handled as additional secondary electrons which are evaluated in energy and angle and returned to the main simulation routine at the end of the function. As TRAX provides shell dependent ionization cross sections, the ionized shell can be checked. When the ionized shell is identified, a check is performed whether Auger electron data for the target material of consideration and the specific shell exists. If not, the Auger routine ends and returns only the secondary electron created by ionization itself as well as the primary projectile to the main routine. If Auger data exists, a transition is chosen by random numbers according to Auger electron probabilities and fluorescence yield for the shell of consideration. The energy of the Auger electron is calculated by the difference in binding energies of the involved shells. So if an Auger transition labelled 1-2-3 occurs, the kinetic energy is  $E_{bnd}(\text{shell } 1) - E_{bnd}(\text{shell } 2) - E_{bnd}(\text{shell } 3)$ . Auger electrons are always emitted isotropically and therefore their emission angle is chosen by two random numbers. The starting coordinates for the Auger electron are copied from the position of the primary projectile.

The correctness of the sampled Auger electron energies also depends on correct electron binding energies. Depending on the chosen energy resolution, Auger transitions at similar energies can appear as discrete lines or a broader peak in the electron spectra.

While for low Z materials, like carbon and oxygen, known Auger transitions lead to the emission of single Auger electrons, for high Z materials with many electron shells, Auger cascades have to be considered. The sampling of Auger electron cascades is performed after the sampling of a primary Auger electron. Created holes in electron shells are followed and stored in an array. The innermost electron shell with a hole is considered to sample the next possible Auger electron creation. If an Auger electron is created, the hole is filled by an electron from an outer electron shell in which a new hole is created. By emission of an Auger electron, a second hole is created as the Auger electron leaves a hole in the shell of its origin. It is always assured that Auger transitions are only possible involving shells that are not empty. If a transition is sampled, which is not possible, a new possible transition is chosen by random numbers and if no transition is possible, the routine ends. Holes are handled from inner to outer shells until no more Auger transitions are possible, due to empty outer electron shells. For each created Auger electron, a random direction is calculated. At the end of the ionization routine, all created Auger electrons are returned to the main simulation routine along with the projectile and the initial secondary electron from the ionization process.

A difficulty in the correct sampling of Auger electron creation lies in the consideration of energy conservation. Without the production of Auger electrons it is assumed in the ionization process that the full binding energy needed to remove the secondary electron is deposited locally. Considering the emission of an Auger electron, a part of this energy is not locally deposited but transferred to the Auger electron in terms of its kinetic energy.

---

---

## 4.4 Non-uniform targets

---

Solid state targets can be non-uniform or inhomogeneous. This can be a geometrical or a compositional non-uniformity. A geometrical non-uniformity means that the target has pinholes or irregular surfaces. Fig. 4.28 shows an electron microscope picture of a thin carbon foil target which has a rough surface consisting of several "rocks" with slits and holes in between. Production of a thin solid state target with a thickness of a few nanometer is very difficult. Polishing of the rough surface might destroy the target. In the analysis of experiments using thin solid state targets, the non-uniformities have to be considered as they affect the measurement results.

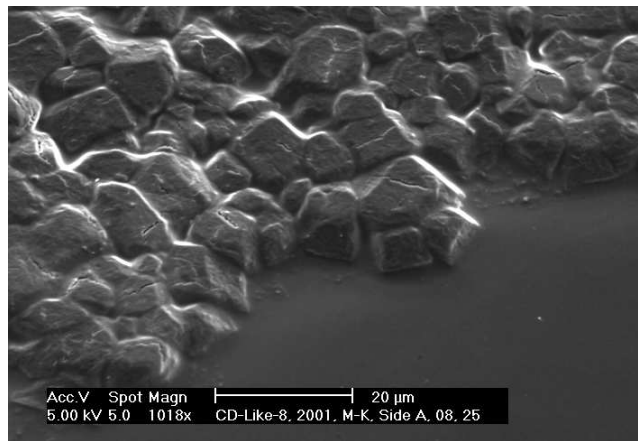


**Figure 4.28:** Electron microscope picture of an unpolished carbon foil with a thickness of around 20 nm which has been used in the Toroid experiment [Lineva2009].

Most MC codes treat the target as an uniform volume of one material. On the macroscopic scale this assumption might be justified but on the microscopic scale deviations might occur. Within this thesis, methods have been developed to describe non-uniformities of solid state targets in a simple way while accounting for the resulting effects from the non-uniformities.

TRAX was designed to be able to handle a target consisting of several sub-volumes which are defined in the geometry file which is read in at start-up of the code. This method is not standard for MC track structure codes. The defined sub-volumes can consist of different materials (atomic, molecular, mixtures or compounds), and each sub-volume can have a different density and a different cut-off energy for a certain particle type (electron or ion). The sub-volumes can be placed anywhere in the coordinate system while dimensions can be chosen freely for a cuboid, cylindrical or spherical volume. It is also possible to define cylindrical or spherical shells or incomplete cylinders or spheres, covering only a partial angular range.

To create an artificial non-uniform target, several sub-volumes are defined which are chosen to be rectangular blocks. Block arrangements are generated by a dedicated script which creates a geometry file. Different types of non-uniformities can be introduced. The first non-uniformity feature is that the individual blocks can be placed in a way to leave holes or slits in between which is then treated as a vacuum. Slits allow the projectiles to pass through the target without undergoing any kind of interaction. Projectiles passing slits do not lose energy and do not change their propagation direction. They can also cross a slit on their way through the

---

target which results in a reduced energy loss compared to projectiles propagating through a solid target without holes. A second possibility to create a non-uniformity, is to change the thickness of some of the sub-volumes. As the thickness of targets with a rough surface might be non-uniform, some projectiles passing the targets will experience a lower target thickness than others resulting in different energy losses. A third non-uniformity feature is to rotate the sub-volumes which is possible around any axis. Rotating the surfaces will alter the incidence angle. Backscattering coefficients depend on the angle of incidence. A non-perpendicular angle of incidence will increase the amount of projectiles being backscattered instead of propagating through the target. Simulations for backscattering coefficients are shown in section 5.1.2.1. A restriction which has to be assured for geometries using TRAX, is that the volumes cannot touch or overlap. This is due to the fact that the volume in which the particle transport is followed is determined by crossing the volume's surfaces. The minimum space that has to be left between the centers of two rotated blocks to avoid touching is  $a/\cos \alpha$  with  $a$  being the edge length and  $\alpha$  the angle of rotation. By packing blocks as closely together as possible considering an equal rotation with angle  $\alpha$ , the surface increases by a factor of  $1/\cos \alpha$  independent on edge length. Fig. 4.29 shows a sketch for a simple non-uniform target in contrast to an uniform target which is standard in MC simulations.

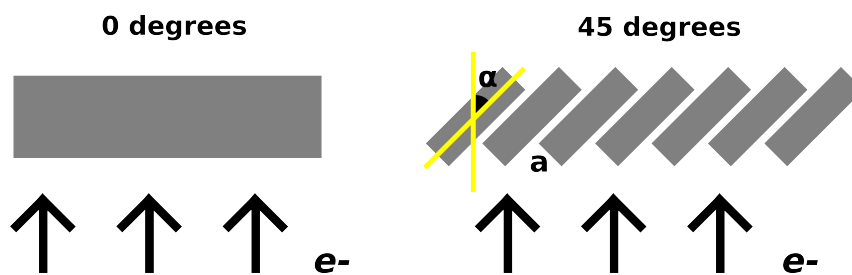


**Figure 4.29:** Schematic picture showing a uniform unrotated target at the left and a non-uniform target at the right side. The non-uniform target consists of several blocks which are rotated by 45 degrees creating an artificial rough surface. Holes are included as well by increasing the space between the centers of the two blocks which allows projectiles travelling through the target without or with reduced energy losses.

Simulations to reproduce experimental backscattering coefficients for an unpolished carbon foil which are affected by non-uniformities of the target are shown in section 5.1.2.1. These will validate the handling of non-uniform targets in TRAX. The procedure to handle non-uniform targets is considered to analyze data from the Toroid experiment in section 5.2.1. It became apparent in the previous part of the analysis of the Toroid experiment [Lineva2008, Lineva2009] that thin solid state carbon targets can be non-uniform and that analysis of the data is not possible without consideration of non-uniformities.

The handling and resulting effects using non-uniform targets in the TRAX MC code is mentioned in [Waelzlein2013a].

---

## 5 Simulations of Microscopic Radiation Transport

The correct handling of radiation transport is the prerequisite to be able to calculate microscopic radiation damage with MC simulations. Understanding the radiation transport delivers basic insight into the radiation action at a very low level. The most important input parameters for the MC simulation of radiation transport are correct interaction cross sections. The main focus lies on low energy electrons as they are directly linked to the nanometer scale due to their short ranges and mean free paths.

One major goal of this thesis is a better understanding of low energy electron interactions (creation and transport) in solids by analyzing the Toroid experiment [Lineva2009] where carbon, nickel, silver and gold have been used as target materials. These experiments were quite unique as they could measure secondary electron spectra energy and angular resolved at energies down to about 50 eV. The observed energy spectra however are a combination of the effects of electron creation and transport even though the target thicknesses have been in the order of only a few nanometers. Measurements covered electrons incident on carbon as well as protons incident on carbon. Additional measurements have been performed for irradiation with  $C^{2+}$  ions incident on C, Ni, Ag and Au. Special focus have been given to the detection of Auger electrons which were intended to be used as probes for the creation and transport processes inside the targets. TRAX was extended to improve calculations to reproduce data from the Toroid experiment which is shown in section 5.2. Previous simulations have been performed using the classic TRAX version [Lineva2008] but could not handle several important phenomena like the Auger electrons and non-uniform targets. Incomplete cross section sets for the investigated target materials did not allow to fully understand electron interactions.

---

### 5.1 Simulations to validate TRAX input

---

Full sets of interaction cross sections for electrons incident on various materials of interest have been assessed. The data collection of D. C. Joy [Joy1995] has been used to find appropriate experimental data for validation of cross sections for electron-solid interactions. Electron stopping powers and electron backscattering coefficients are given for a broad range of materials. D.C. Joy does not give accuracies for the experimental values in his collection and unfortunately not all original publications were available. Moreover, it is a common observation that different experimental data for the same quantity do not agree. Nevertheless, simulations to reproduce these data serves as a crucial step to validate the cross section sets used in this thesis. Due to these uncertainties this could not be done with high assurance. However, the data has been taken for comparison with TRAX simulations as no other data has been available. Additionally to the data of Joy, transmission measurements from Reimer and Drescher [ReDr1977] have been used to verify electron cross sections for specific targets. In the following subsections, data for electron stopping powers are used to test ionization and excitation cross sections. Experiments for the electron backscattering coefficient are used to test the elastic scattering cross sections

---

and the ratio between elastic and inelastic cross sections. Data from transmission experiments are used to test the applicability of both elastic and inelastic cross sections.

---

### 5.1.1 Stopping Power

---

The stopping power  $S$  defines the linear energy transfer of a projectile traversing a given material. It is defined as the energy loss per unit path length  $dE/dx$  and usually given in units of  $\text{keV}/\mu\text{m}$ . The stopping power is a measure for the sum of all inelastic scattering contributions. Data from stopping power measurements given in [Joy1995] have been used as a validation for the inelastic cross sections used in TRAX. Alternatively to conventional theoretical approaches to determine the stopping power, the stopping power can also be obtained if cross sections and corresponding energy losses are known for each inelastic interaction. The sum of the stopping power contribution of each considered inelastic scattering interaction should result in the total stopping power. Both ionization and excitation contribute to the energy loss of electrons in the target material of consideration. From all considered ionization and excitation channels, a total stopping power  $S(E)$  can be calculated:

$$S(E) = \sum_i \Delta E_i \cdot \sigma_i(E) + \sum_j \int (T + I_j) \cdot \frac{d\sigma_j(E, T)}{dT} dT \quad (5.1)$$

where  $\sigma_i$  are the cross sections for the  $i$  excitation channels and  $\Delta E_i$  the corresponding energy losses.  $\frac{d\sigma_j(E)}{dT}$  are the energy differential ionization cross sections for the  $j$  shells, depending on both projectile energy  $E$  and kinetic energy of the ejected secondary electron  $T$ .  $I_j$  denotes the ionization potential for shell  $j$ . The results from formula 5.1 are benchmarked against data from [Joy1995]. The stopping power is often given normalized to the target density in units of  $\text{MeV cm}^2/\text{g}$ .

At high incident electron energies ( $>10$  keV) the total stopping power is reasonably well known as it can be described with the Bethe theory [Bethe1930, Bethe1932, Bloch1933]. However, it depends on the correct choice of the mean excitation potential  $\langle I \rangle$  which is usually obtained by a fit on experimental data, values are given in [ICRU1984]. Recommended  $\langle I \rangle$ -values for a given material can change over time. NIST [Berger2005] provides values for the stopping power of electrons incident on various atomic materials starting at energies above 1 keV, with best confidence above 10 keV. NIST calculations are based on the Bethe theory and apply density effect corrections according to Sternheimer [Sternheimer1952, Sternheimer1982]. The high energy region of the stopping power resulting from TRAX cross sections can be validated using NIST values for comparison. NIST values "automatically" agree with measured stopping power values as the  $I$ -values were obtained by fits to experimental results. Above 1 keV, excitation plays a minor role, so a mismatch in stopping powers at high energies is supposed to be due to inappropriate ionization cross sections. For electrons incident on Fe and Ni, the stopping powers around 10 keV calculated from TRAX classic ionization cross sections overestimated the NIST values even without consideration of excitation as an additional energy loss (Fig. 5.2). A more appropriate choice of binding energy values yields a different ionization cross section allowing to reproduce the well known stopping power at high energies.

Below 1 keV, the Bethe theory is no longer applicable. Experimental data (as far as existing) can be used to validate calculated stopping powers at low energies. Different sets of experimental data for the same target material, can show a spread at a given energy by a factor of more than

---

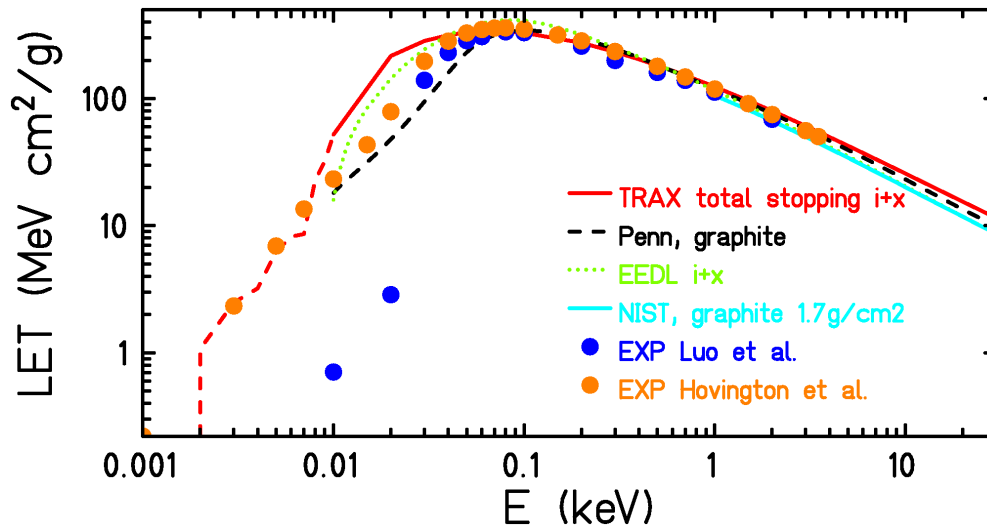


**Figure 5.1:** Stopping power values are a means to verify inelastic scattering cross sections. The symbols represent experimental values obtained by Luo et al. [Luo1991] and Hovington et al. [Hovington1996]. The red solid line represents the total stopping power from ionization (i) and excitation (x) as implemented in TRAX. The dashed part of the red line indicates that only excitation contributes to the stopping power at this energy region. The green dotted line shows the stopping power obtained from the cross sections in the Evaluated Electron Data Library [PeCu1991a]. The dashed black line shows semi-empirical calculations from the Penn algorithm [Shinotsuka2012]. NIST [NIST] values are only available at energies above 1 keV and are shown with a purple solid line.

two. Experiments are usually performed measuring transmission electron energy loss spectra from thin films or by calorimetric measurements. In the low energy region around 100 eV, electronic excitation, plasmon excitation and ionization contribute significantly to the total stopping power. In this energy region, a mismatch of the TRAX stopping power to experimental data is not easily to attribute to a source of disagreement. The latter can be due to large uncertainties in experimental data or it can be due to inappropriate cross sections. An underestimation of the total stopping power only at low energies can be due to missing excitation channels. Published sets of stopping power data often have large uncertainties and/or differ from each other below 1 keV. The Evaluated Electron Data Library (EEDL) [PeCu1991a] is used, e.g., by GEANT4 [AgAl2003, Geant4] down to 250 eV. It should be noted that the stopping power contributions from ionization and excitation below 100 eV in the EEDL might be uncertain of up to 1000% as they were obtained from differential energy spectra which were normalized to the excitation stopping power at 100 GeV [PeCu1991a]. Above 100 eV an uncertainty of 20-50% for excitation and 10-20% for ionization stopping powers between 100 eV and 1 keV is considered [PeCu1991a]. Comparisons with stopping powers from EEDL have been made for carbon targets (Fig. 5.1). Experimental data from Luo [Luo1991] and Hovington [Hovington1996] deviate from each other below 100 eV but their precision is not known. Both data sets are part of the collection of Joy [Joy1995] where no attempt was made to determine accuracies. The stopping power values of Luo and Hovington have been determined by measurements of transmission electron energy-loss spectra through thin films using 100 or 200 keV electrons as primary

projectiles [Shinotsuka2012].

Further comparisons have been made with semi-empirical calculations from Shinotsuka et al. using the full Penn algorithm [Shinotsuka2012] to calculate stopping powers based on parameters fitted to experimental data (optical energy loss functions (ELFs)). Low energy values are extrapolated. The Penn algorithm ignores low-energy effects like electron exchange and correlation. The calculations are based on the dielectric formalism which does require the validity of the first Born approximation (FBA) to give accurate results. Only if the FBA is valid, the probability of energy transfer  $E$  and momentum transfer  $\hbar K$  are proportional to the energy loss function  $Im[-1/\epsilon(E, K)]$  [Dingfelder1998]. This is well known from publications dealing with inelastic cross sections of charged particles at low energies [Inokuti1994, Dingfelder1998, ?]. Based on comparisons with experimental data, cross sections based on the FBA are often overestimated by a factor of two around energies of about 100 eV, the region in which ionization cross sections reach their maximum [Inokuti1994, Dingfelder1998]. Therefore, the accuracy of results from the Penn algorithm in the low energy region ( $<1$  keV) is questionable and deviations from TRAX results are considered to be uncritical in this energy region. However, above 1 keV, TRAX results should match the results from conventional tables. Comparisons of stopping power values are shown exemplarily for all Toroid target materials, carbon (Fig. 5.1), nickel (Fig. 5.2), silver (Fig. 5.3) and gold (Fig. 5.4). It can be seen, that in the high energy region, TRAX results agree with reported values. In the low energy region, TRAX cross sections are supposed to be applicable.

Comparing stopping power values for gold to other calculations and experimental data, the val-

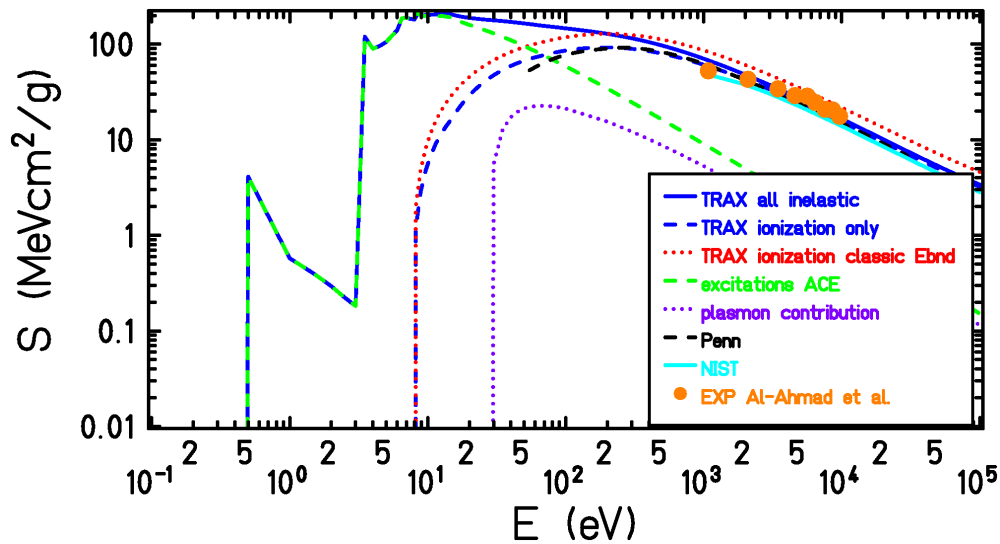


**Figure 5.2:** Stopping power values for electrons in Ni. One can clearly see that even without considering excitations, the TRAX classic stopping power from ionization was too high compared to reported values above 1 keV. The fact that TRAX can now reproduce the stopping power above 1 keV is indicating a correct ionization cross section. The semi-empirical Penn algorithm is supposed to be accurate only at energies above 1 keV. Differences to TRAX are considered uncritical. See text for details.

ues agree within a factor of less than 10, as shown in Fig. 5.4. For Au, semi-empirical stopping power values are given by [Fernandez1993] which are based on a generalized oscillator strength



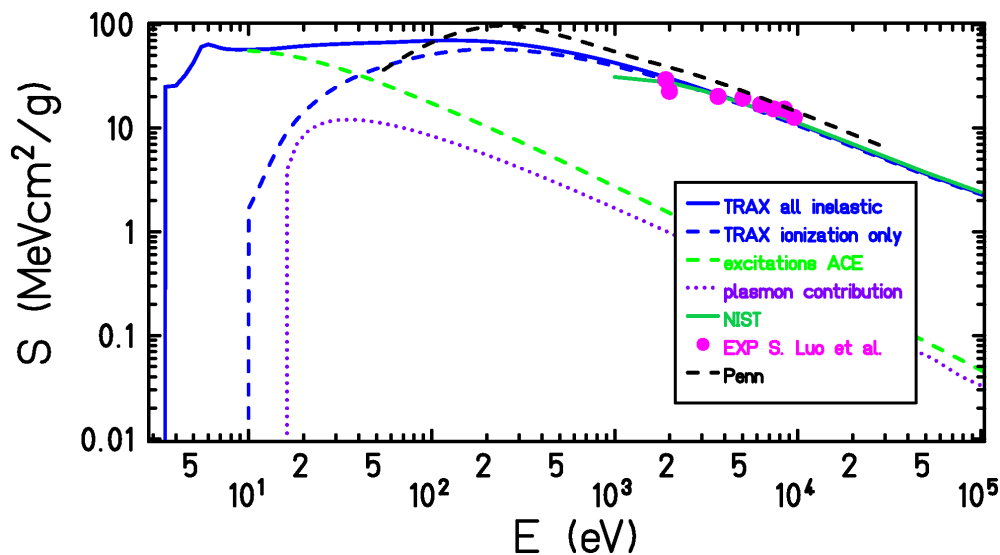


**Figure 5.3:** Comparison of stopping power values for electrons on silver. TRAX values agree with experiments and well accepted values at high energies. For low energies ( $< 1\text{keV}$ ), a reasonable comparison is difficult. The experimental data are taken from [Luo1991]. The results based on the Penn algorithm are discussed to be mismatching with experimental results, even at high energies, where the FBA is valid, due to uncertainties in experimental ELF [Shinotsuka2012].

model using optical and photoelectric data. This method is not very accurate for low energies as it is again depending on the validity of the FBA. Although stopping powers are calculated down to 15 eV, they note that their formula is not appropriate below 790 eV [Fernandez1993]. The stopping power from TRAX below 10 eV is obtained from experimental excitation cross sections according to [Maslov2008, Zatsarinny2008] and deviates from experimental stopping power values. The uncertainty of the excitation cross sections is known (indicated by an error band in Fig. 5.4), while the uncertainty of stopping power values from measurements in [Luo1991] is unclear. The uncertainty of measurements for energies above 1 keV from [AlWa1983] is known and supposed to be around 15%. From discrepancies between experimental data below 100 eV, it can be concluded, that the electron stopping power in gold is not reasonably well known at this energy region. In summary, the cross sections chosen for TRAX calculations are supposed to represent best the most important energy region around 100 eV. As other theoretical approaches require the validity of the FBA, comparisons of TRAX stopping power values to other models can reasonably be made only above 1 keV.

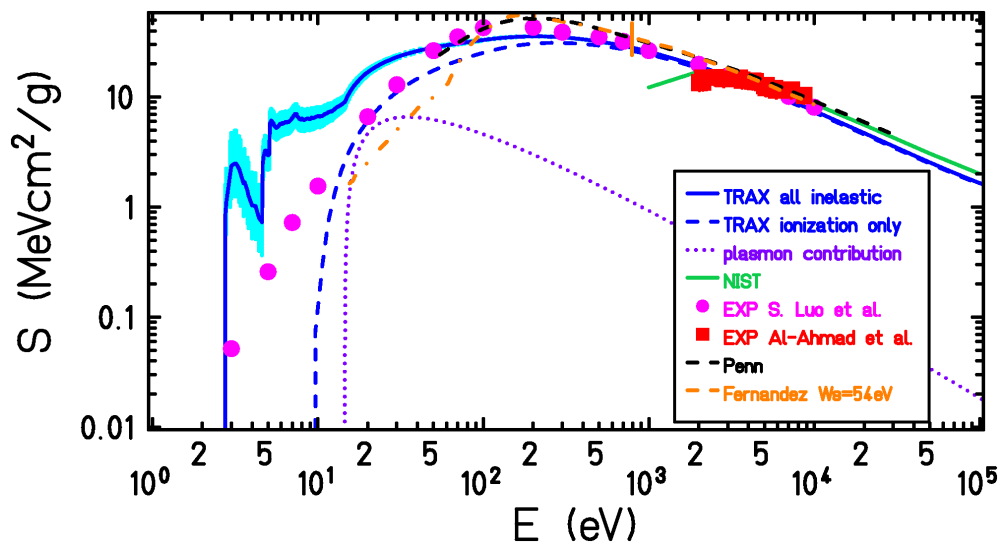


**Figure 5.4:** Comparison of values for stopping power of electrons on gold. The light-blue error band indicates the stopping power uncertainties resulting from uncertainties in experimentally obtained excitation cross sections. Dots and squares present experimental data from [Luo1991] and [AlWa1983] respectively. Calculations from [Fernandez1993] are supposed to be appropriate above 790 eV, which is indicated by a vertical line in this plot. Stopping powers using the Penn algorithm are fitted to experimental data [Shinotsuka2012].

---

## 5.1.2 Electron backscattering coefficients

---

The electron backscattering coefficient can be a useful benchmark method to verify the electron cross section input of a MC simulation. The energy dependent backscattering coefficient  $\eta(E)$  is conventionally defined as the amount of electrons with energies above 50 eV which leave a semi-infinite target at the entrance surface, divided by the amount of incoming electron projectiles.

Electron backscattering coefficients are not only influenced by the elastic scattering cross sections but also by the ratio between elastic and inelastic cross sections. Inelastic cross sections can indirectly enhance or reduce the number of elastic scattering events as a concurrent interaction. According to D.C. Joy [Joy1995], measurements of electron backscattering coefficients provide a useful method to verify the correct ratio between elastic and inelastic cross sections. If the inelastic cross sections are too small (which can be the case if important inelastic channels are not considered), the simulated backscattering coefficients can be too high as the probability for elastic scattering increases while the number of inelastic collisions is decreased. Inelastic interactions may prevent an electron from escaping the target by being absorbed before reaching the exit surface. Higher inelastic cross sections on the other hand reduce the amount of elastic scattering events. With high inelastic cross sections, electrons lose their energy faster so that more electrons are absorbed before they can be backscattered outside the target. Therefore, inelastic cross sections can indirectly reduce the contribution of elastic scattering events. If elastic scattering cross sections are incorrect, for example if scattering to backward angles is underestimated, a deeper penetration into the target material will occur, leading to more inelastic interactions. The amount of electrons which are backscattered and eventually escape the target at the entrance surface is therefore diminished.

The data collection of Joy [Joy1995], which provides measured stopping power values, also provides a collection of measured electron backscattering coefficients which have been used to verify the employed cross sections for elastic and inelastic scattering. In standard backscattering measurements, only electrons with energies above 50 eV are detected to get the "real" primary backscattered electrons rather than a mixture of secondary and primary electrons. The choice of 50 eV is rather arbitrary. However, in reality secondary electrons can be also produced with energies above 50 eV. This threshold is usually realized in experiments by the use of a grid repelling electrons back to the target as a voltage of -50 V is applied [Verma1977].

Calculations using the TRAX classic cross section set (consisting of ionization as only inelastic interaction and elastic scattering described by screened Rutherford cross sections) generally result in high backscattering coefficients. For a range of target materials of interest, backscattering coefficients have been calculated with TRAX and compared to experimental data. Both the experimentally common threshold of 50 eV and the realistic threshold of 0 eV have been used. Including excitations enhances the total inelastic cross sections and reduces therefore the ratio of elastic versus inelastic cross sections. This leads to a reduction of calculated backscattering coefficients. The impact of excitation on backscattering coefficients is large, even for primary projectile energies above 1 keV, an energy at which excitation is supposed to have a minor contribution to the total electron stopping power. But the backscattering coefficient includes also secondary electrons with lower energies, which are affected by excitations. Changing the elastic scattering cross section model from screened Rutherford cross sections to those based on PWA also changes the simulation results (more effectively for higher Z materials where devi-

---

ations between the two models are larger). Comparisons are shown for aluminium (Fig. 5.5), iron (Fig. 5.6), nickel (Fig. 5.7), silver (Fig. 5.8) and gold (Fig. 5.9). Carbon has been handled separately as it shows discrepancies between measurements of polished and unpolished targets which are explained in section 5.1.2.1.

Generally it has been found, that experimental data from different experiments concerning

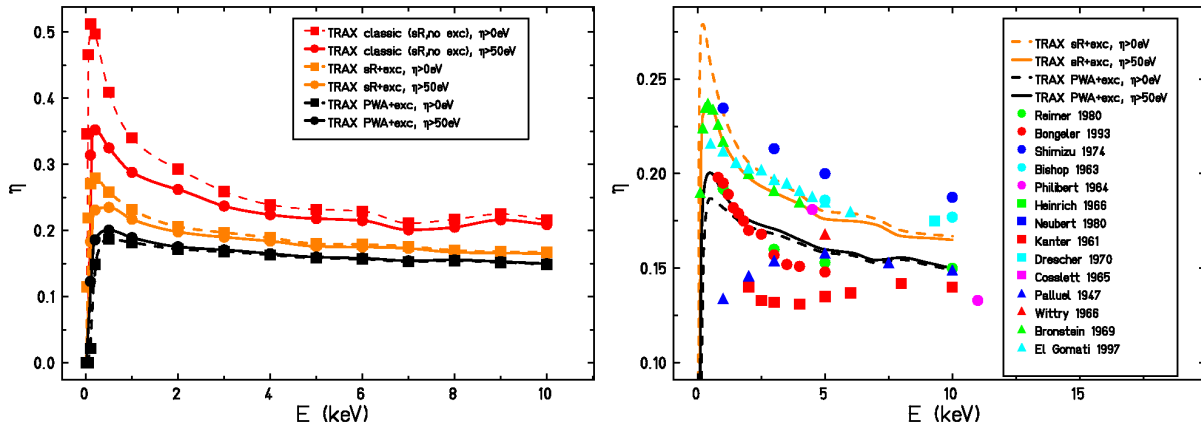


**Figure 5.5:** Energy dependent electron backscattering coefficients for Al ( $Z=13$ ). On the left hand side, different TRAX versions are compared. The red line correspond to TRAX classic, using screened Rutherford cross sections and neglecting excitation cross sections. Orange lines show results for screened Rutherford cross sections and including excitations cross sections from the ACE code. Black lines show results for elastic scattering cross sections based on PWA and included excitation. On the right hand side, comparison with experimental data is shown. Experimental data deviate from each other considerably. TRAX values lie in between experimental results.

the backscattering coefficients for electrons incident on the same material show discrepancies that can be large. One explanation can be that the target conditions have not been equal. Experiments using different target geometries are not consistent. Non-uniform targets or slightly changed electron beam incident angles can alter the backscattering coefficients. The impact of incident angles and non-uniform targets are discussed in more detail in section 5.1.2.1. It is also possible, that targets might have surface contaminations, altering the backscattering coefficient. Some experiments might have used an oil diffusion pump which has been shown to alter backscattering coefficients as a thin oil film can build up on a target [Sternglass1954]. Certain elements react strongly with oxygen. An oxygen layer altering backscattering coefficients is another possible explanation of disagreement in experimental backscattering coefficients [Gomati2008], as well as poor vacuum conditions. Usually a potential of 50 Volts is applied to stop electrons with energies below 50 eV from being detected as the backscattering coefficient is usually defined as the ratio of electrons with energies above 50 eV. A minor change in this potential can alter the backscattering coefficient, as the yield of secondary electrons with energies around 50 eV is high. TRAX simulations show a large difference between backscattering coefficients including electrons with energies above 0 eV or 50 eV.

In comparisons of simulation results with experimental data, even though the spread in experimental data is large, it becomes obvious that using screened Rutherford cross sections for high  $Z$  materials cannot reproduce experimental backscattering data. The quantitative mismatch is

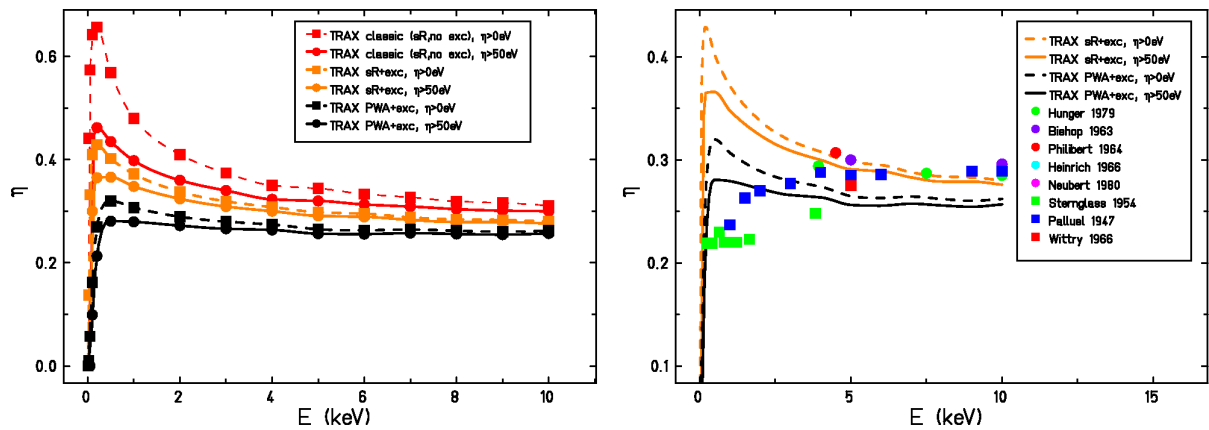


**Figure 5.6:** Comparisons of backscattering coefficients for electrons incident on iron. On the left hand side, different TRAX versions are compared. The right hand side shows a comparison of calculations with experimental data. There is a noticeable spread of the experimental data as well.

large and also a qualitatively mismatch exists. Experimental data for high Z materials, like silver or gold, show an increase of backscattering coefficients increase for increasing energies until the backscattering reaches saturation. Simulations based on screened Rutherford cross sections show an inverse profile with a maximal backscattering coefficient at low energies and a decrease with energy down to a saturation plateau. Simulations using elastic scattering cross sections based on PWA can correctly reproduce the shape which is observed from experimental data for high Z materials. This justifies the effort of using the much more elaborate method for elastic scattering cross sections. Especially when wanting to correctly describe electrons with energies much lower than 100 eV, this approach is mandatory.

The differential elastic scattering cross sections will determine the angular distribution and the amount of elastic scattering events which will be reflected in the backscattering coefficients. The standard cross section in TRAX are based on screened Rutherford cross sections (SRCS). However, for low energies and medium to high Z (atomic number) values, screened Rutherford cross sections, which are based on the Born approximation (BA), are not optimal to correctly describe the angular differential elastic scattering of electrons. Further details of the SRCS and PWA are discussed in chapter 4. In the framework of this thesis, differential elastic scattering cross sections relying on partial wave analysis (PWA) have been assessed. Details on the improvement and calculation method are described in chapter 4 where the input of the NIST ELAST database is discussed. These cross sections show a qualitatively different shape for the differential cross sections (especially for high Z materials and low energies) and can differ largely also in the total cross sections in the case of high Z materials. Screened Rutherford cross sections overestimate the forward elastic scattering for low energetic electrons, especially for high Z materials. For all simulations shown later in this thesis it is explained whether elastic scattering cross sections for PWA have been used rather than SRCS. In general, SRCS have been only used for very low Z materials like carbon and water (applying empirical corrections). For medium to high Z materials like Fe, Ni, Ag, Au, Pt and Gd, cross sections based on PWA have been preferred.

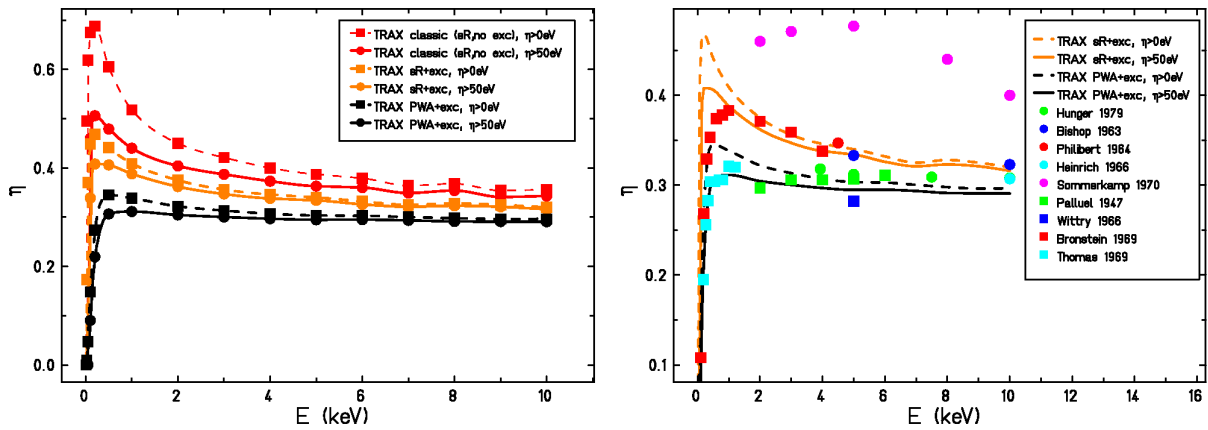


Figure 5.7: Comparisons of backscattering coefficients for electrons incident on nickel. On the left hand side, different TRAX versions are compared. The right hand side shows a comparison of calculations with experimental data. There is a large spread of the experimental data. TRAX results using elastic scattering cross sections based on PWA agree best with experimental data of [Thomas1969, Palluel1947, Wittry1966].

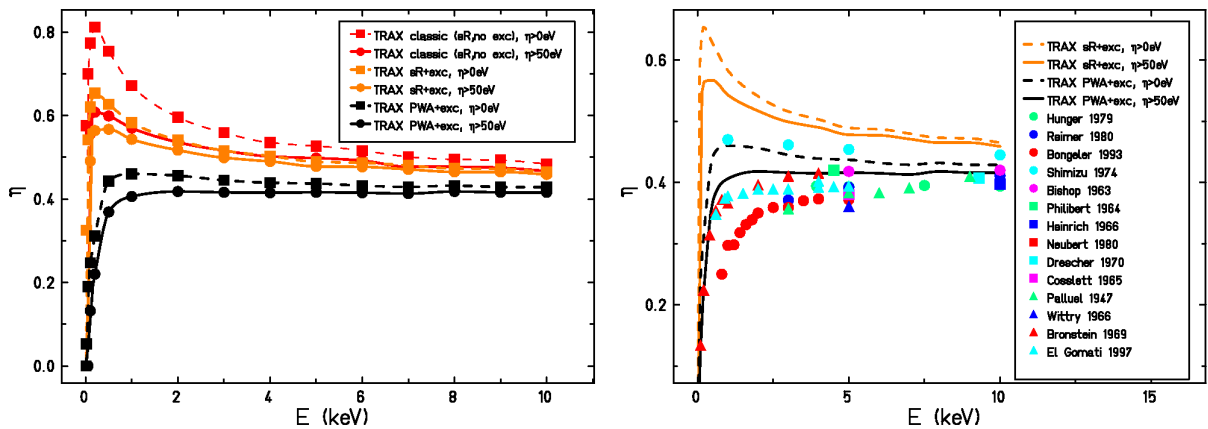
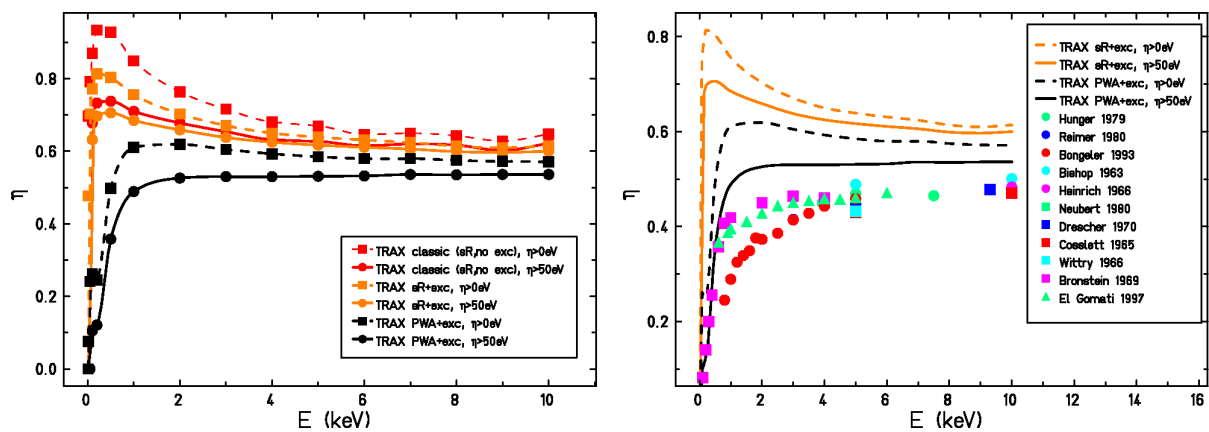


Figure 5.8: Comparisons of backscattering coefficients for electrons incident on silver. Experimental data are inconsistent. Switching from screened Rutherford cross sections to those based on PWA changes the TRAX results not only quantitatively but also qualitatively. The shape of experimental data can be reproduced only using cross sections based on PWA. TRAX results agree well with experiments from [Bishop1963, PhWe1963, Bronstein1969]



**Figure 5.9:** Backscattering coefficients for electrons incident on gold. TRAX calculations have been performed using screened Rutherford cross sections or PWA for elastic scattering. Resulting backscattering coefficients from TRAX using excitation cross sections and elastic scattering cross sections based on PWA reproduces qualitatively the shape of the energy behaviour of the backscattering coefficient from experimental data. However, results from TRAX are still slightly too high for energies above 1 keV which might be due to target conditions.

---

### 5.1.2.1 Backscattering from non-uniform targets

---

Solid state targets, especially graphite targets, can be non-uniform, which has been observed within the Toroid experiments [Lineva2009] and has been discussed in section 4.4. An electron microscope picture of a thin carbon target (Fig. 4.28) shows clearly the possibility of holes and a "rock"-like structure creating a rough target surface. Backscattering coefficients can be largely affected by the roughness of the target as they are dependent on the angle of incidence. The backscattering coefficient is lowest for perpendicular incidence considering the target at a rotation angle of  $0^\circ$  relative to the plane perpendicular to the beam. Rotating the target by a certain angle, increases the backscattering coefficients up to a rotation angle of  $45^\circ$  where a maximum is reached. The trend is shown in Fig 5.10 where backscattering coefficients for electrons incident on carbon have been calculated with TRAX (using screened Rutherford cross sections for elastic scattering and the new inelastic cross section set) using an uniform target.

Holes inside the bulk target on the other hand, let incident electrons traverse the target with-

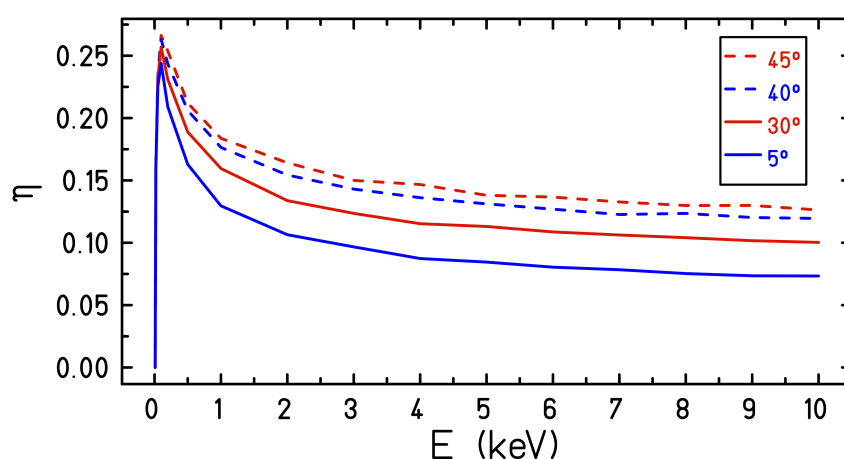


**Figure 5.10:** Simulated backscattering coefficient  $\eta$  of electrons incident on a rotated uniform carbon target. Backscattering coefficients are shown from top to bottom for rotating angles of 45, 40, 30 and 5 degrees. Zero degree correspond to perpendicular incidence of the beam on the target. It can clearly be seen that the backscattering increases with increasing rotation angle. The backscattering is at its maximum at an incident angle of 45 degrees to the plane.

out or with reduced interactions. Holes or slits can therefore reduce the number of scattering events and reduce the backscattering coefficient as electrons can penetrate deeper inside the target or even pass through rather than being backscattered. In section 4.4 TRAX extensions are explained which allow the handling of a non-uniform target that can consist of several rotated blocks aligned in a way to create slits in between. Fig. 5.11 shows TRAX calculations for the electron backscattering on carbon in the presence of slits of varying thicknesses, while larger slits obviously decrease the backscattering coefficients. A laterally extended source has been assumed.

A non-uniform target is considered to alter the backscattering coefficient in both directions. An increase due to rough surfaces non-perpendicular to the incident electron beam and a decrease through holes and slits.

---



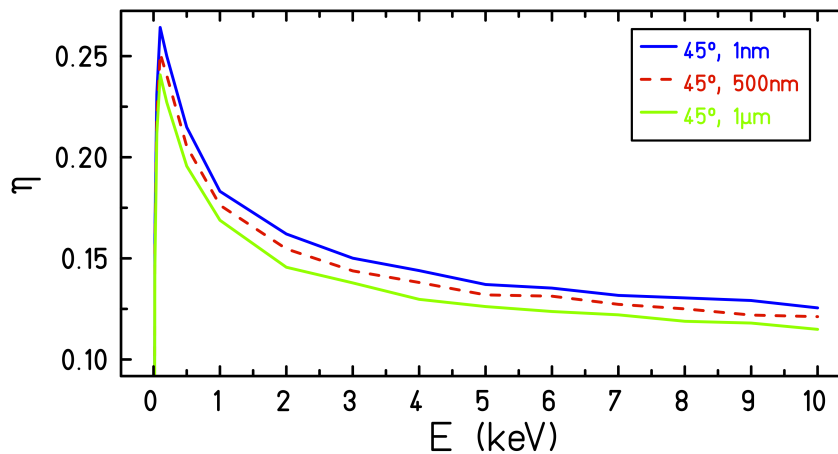


**Figure 5.11:** Simulated backscattering coefficient  $\eta$  for electrons incident on a non-uniform carbon target. The curves are shown depending on the slit sizes of the target. Blocks of a size of  $5\mu\text{m}$  ( $x$ )  $\cdot$   $10\mu\text{m}$  ( $y$ ) are rotated by 45 degrees and aligned with a certain slit size in between. It can clearly be observed that the backscattering coefficient decreases with enhanced slit size. Simulations have been performed with the electron beam impinging perpendicular to the target.

The backscattering coefficient for electrons on carbon has been measured by various authors [HuKü1979, Bishop1963, PhWe1963, Heinrich1966, Sternglass1954, Palluel1947, Wittry1966, Bronstein1969, Gomati1997]. Verma [Verma1977] explicitly measured the backscattering coefficient for polished and unpolished targets, showing a clear difference due to a smooth or rough surface. The experimental data from Verma for electron energies between 0.5 keV and 10 keV has been used as a benchmark for the handling of non-uniform targets in TRAX. Therefore, TRAX calculations have been performed assuming both uniform carbon as well as non-uniform targets. The non-uniform target has been artificially simplified to show a qualitative trend of an enhanced backscattering due to a rough surface. Rectangular blocks of  $5\mu\text{m} \cdot 10\mu\text{m}$  surface area ( $x \cdot y$ ) have been rotated by  $45^\circ$  around the  $y$ -axis. The blocks were aligned with  $0.1\mu\text{m}$  gaps in between (in  $x$ - and  $y$ -direction). The comparison of TRAX calculations with experimental data can be seen in Fig. 5.12.

Below 4 keV, TRAX simulation results for the polished target deviate from the results of Verma [Verma1977] but agree well with data from [Bronstein1969, PhWe1963, Wittry1966, Bishop1963]. Between certain sets of experimental results from different authors, large discrepancies can be observed. This can be explained as target conditions differed. A target below saturation thickness results in a backscattering coefficient which is too low. The target of Verma [Verma1977] has been a graphite target which was cut from a carbon electrode rod. He reports an accuracy of 5%-10% for his measured values obtained by the deviations from mean values for measurements of different graphite samples. Sternglass [Sternglass1954] used a totally different target production-wise. It was prepared from an aqueous solution of colloidal graphite deposited on a nickel disk and baked out [Sternglass1954]. Sternglass wanted to show that the backscattering coefficient for low  $Z$ -materials was independent on energy. Sternglass also mentions that he observed backscattering coefficient shifts due to different temperatures and performed his experiments at 200-400 °C. The target of Hunger [HuKü1979] has been mechanically polished and an accuracy of 2% is assumed. Exact experimental con-

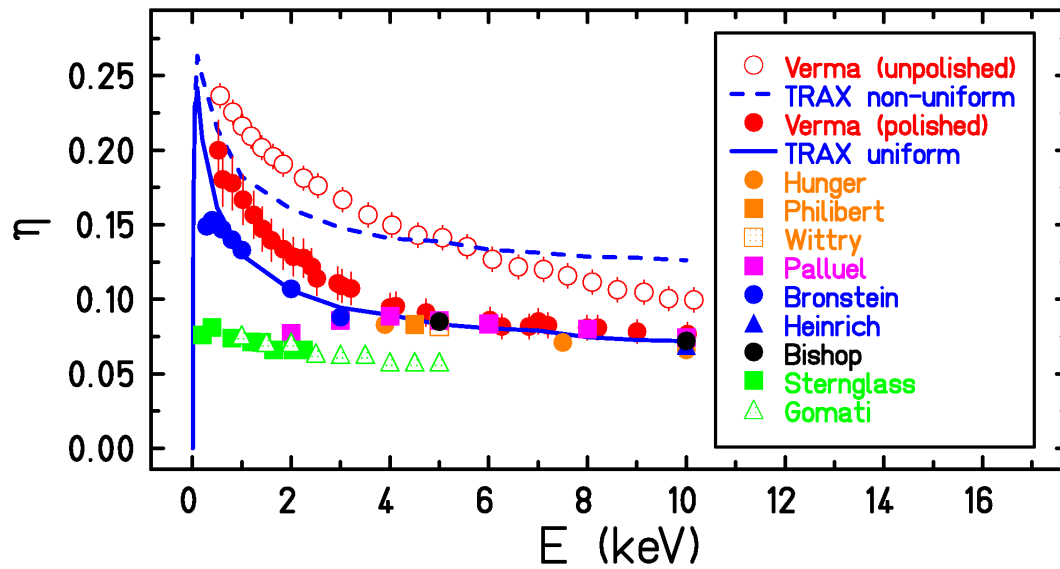


**Figure 5.12:** Back scattering coefficients for electrons incident on carbon polished and unpolished. Experimental data from different authors show a large spread. TRAX calculations for the uniform target are consistent with experimental data from [Bronstein1969, PhWe1963, Wittry1966, Bishop1963]. Other data are supposed to be taken under different target conditions. The qualitative trend of an increased backscattering coefficient for the unpolished target is reproduced by TRAX. Deviations are supposed to stem also from an extremely simplified description of the non-uniform target, which not necessarily reflects the poorly known experimental situation.

ditions for the unpolished target of Verma [Verma1977] are unknown. Therefore a qualitative reproduction of differences of the backscattering coefficients between polished and unpolished targets by TRAX is seen to be sufficient to show that TRAX can handle non-uniform solid state targets. A fairly reasonable qualitative agreement is achieved considering the largely simplified non-uniform target for the simulations and the lack of knowledge about the exact target conditions in the experiment.

---

### 5.1.3 Electron transmission

---

Measurements of electron transmission through thin foils can serve as a further validation for correctness of elastic and inelastic cross sections. Experiments on low-energy electrons are scarce. In the framework of the Toroid experiments, scaling measurements for electrons incident on Al, Ni, Ag and Au have been performed but the data could not be analyzed.

Reimer and Drescher [ReDr1977] performed experiments using thin aluminium and gold foils. They used electrons with energies of 10 - 100 keV as projectiles and defined transmitted electrons as electrons with exit energies above 50 eV [ReDr1977]. The experiments have been performed under normal incidence and transmission coefficients are given as a function of foil thickness for several electron projectile energies. TRAX simulations have been performed for Al and Au foils of various thicknesses for an energy of 9.37 keV, which is the lowest considered in [ReDr1977] and which experiments are mentioned in [Browning1994] with a focus of using proper cross sections for elastic electron scattering. As TRAX is designed to be suitable especially for low-energy electrons, this energy, as it is the lowest present in the experiments, is the most suitable for validations. The experimental results of [ReDr1977] have been carefully digitized from the plots presented in [Browning1994]. Simulations have been performed using complete sets of ionization and excitation cross sections as assessed in the framework of this thesis. For elastic scattering, the "classic" screened Rutherford cross sections as well as the newly assessed cross sections from ELAST have been used in comparison. Fig. 5.13 shows calculation results together with experimental data. The thicknesses given in units of  $\mu\text{g}/\text{cm}^2$  correspond to thicknesses of around 200 nm-1100  $\mu\text{m}$  for Al and 25 nm-155 nm for Au.

In the case of gold it is obvious, that TRAX with the current set of cross sections including those

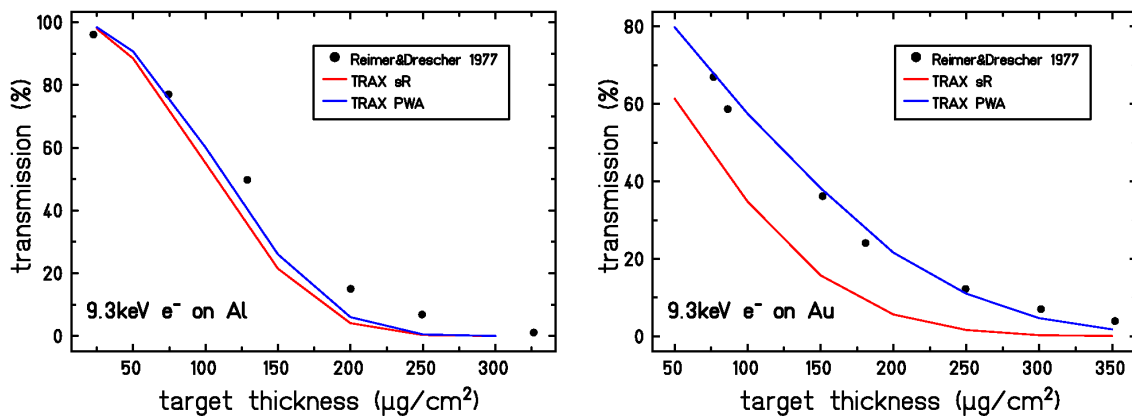


**Figure 5.13:** Transmission coefficients for 9.3 keV electrons incident on aluminium (left picture) and gold (right picture) foils of varying thicknesses compared with TRAX simulations. The experimental values are digitized from [Browning1994] and shown with black dots. The red lines show results from TRAX simulations using the new inelastic cross sections but the previous standard cross sections for elastic scattering (screened Rutherford). The blue lines show the results considering also new elastic scattering cross sections based on PWA.

for elastic scattering based on PWA can reproduce the experimental results. Simulations using elastic scattering cross sections based on screened Rutherford calculations deviate a lot from ex-

---

---

perimental transmission results as for high Z materials these cross sections are not appropriate. The calculations based on screened Rutherford cross sections underestimate the transmission significantly. For aluminium, as a low Z materials for which screened Rutherford cross sections should not be too wrong, a change in the elastic scattering cross sections does not lead to a significant change in transmission results for the chosen projectile energy. However, for both cross section choices, TRAX underestimates the experimental results slightly. This can be explained by experimental uncertainties as the authors report uncertainties due to incomplete detector efficiencies [ReDr1977]. Therefore, the agreement between experimental data and simulation results is considered to be good. The choice of elastic scattering cross sections based on PWA is once more justified and the inelastic cross sections seem to be accurate as otherwise the transmission experiment could not have been reproduced.

---

## 5.2 Simulations for the Toroid experiment

---

Experiments using the Toroid spectrometer [Lineva2009] are some of the very few experiments concerning low-energy electrons ( $< 1$  keV) emitted and transported in solids. These experiments were performed at the Atomic Physics department at GSI by N. Lineva et al. [Lineva2008, Lineva2009] and are well suited to gain further knowledge about low-energy electron interactions in solids and to verify the extended TRAX simulation code. The spectrometer allows to measure angular and energy electron spectra of electrons which are emitted from thin target foils after electron or ion bombardment. It was designed to perform systematic investigations of low energy electron emission for energies below 1 keV down to about 50 eV. The experiments included calibration measurements with 0.5 keV and 1 keV electrons incident on carbon. Furthermore, experiments have been performed for 8.77 MeV protons on carbon and 3.6 MeV/u and 11.4 MeV/u C<sup>2+</sup> ions on carbon, nickel, silver and gold. Target thicknesses have been  $4.7\mu\text{g}/\text{cm}^2$  (C),  $45\mu\text{g}/\text{cm}^2$  (Ni),  $38\mu\text{g}/\text{cm}^2$  (Ag) and  $40\mu\text{g}/\text{cm}^2$  (Au). Even though these targets had thicknesses in the nanometer range, they still comprised several atomic layers. In all experiments, secondary electron energy spectra have been measured, which reflect a combination of electron creation and transport as emitted electrons are stopped or slowed down before leaving the target. For the carbon target, angular spectra have also been measured. Transmitted as well as backscattered electrons could be detected.

In the PhD thesis of N. Lineva [Lineva2008] pioneering attempts to reproduce the experimental data from the Toroid with the classic TRAX version have been performed. However, several issues remained unsolved. Experimental data showed evidence for non-uniformities in the carbon target as transmitted electrons could be detected without any energy loss. The handling of non-uniform targets has not been considered in TRAX classic simulations. Auger electrons were visible in the secondary electron spectra but were not included in previous simulations. Besides, the electron cross sections for all target materials (C, Ni, Ag and Au) have been incomplete (no electronic excitation) or based on insufficient models (for elastic scattering on Ni, Ag and Au). Additionally, also the electron ionization cross sections have been modified within this thesis. Several simulations have been repeated using the extended TRAX code that has been developed in the framework of this thesis. Some simulations results are compared for TRAX classic and the extended version. Furthermore, new simulations have been performed to extend the understanding of the Toroid experiments. In subsection 5.2.1, simulations are shown for the calibration experiments with electron projectiles and carbon targets. Special focus has been given on the non-uniformity of the target. Subsection 5.2.2 deals with the description of elec-

---

---

tron energy losses in the target materials of consideration. Detailed knowledge about electron interactions is mandatory when describing more complex experiments using ion projectiles. In subsection 5.2.3, simulations are shown for experiments with protons, the most simple type of ion projectiles. Auger electron creation is discussed in detail. In the following subsection 5.2.4, further details about the range of Auger electrons are investigated, which have been discussed as probes for electron transport processes. Subsection 5.2.5 shows the most complex experiments, where carbon ions have been used as projectiles to study electron emission cross sections.

---

### 5.2.1 Electron yields and transmission spectra

---

Although the ultimate goal is to describe production and transport of electrons after irradiation of solid state targets with ions, a useful prerequisite is to observe the effects of irradiation with electrons as primary projectiles. Being able to correctly describe electron transport processes is necessary before handling more complicated scenarios with ions projectiles. For calibration purposes, measurements were performed using mono-energetic electrons from an electron gun with 500 eV and 1 keV [Lineva2009]. Carbon targets with a nominal thickness of  $4.7\mu\text{g}/\text{cm}^2$  and  $11\mu\text{g}/\text{cm}^2$  were bombarded with 1 keV electrons and the energy and angular resolved yields behind the target were measured.

As it has been discovered that the thin carbon foils showed non-uniformities (already discussed in section 4.4), simulations have to account for resulting effects to reproduce experimental data. To be able to perform simulations for the carbon target without spending too much effort on the details of the non-uniformity, an effective thickness has been derived. The electron yields as a function of the emission angle have been measured for the used carbon targets bombarded with 1 keV electrons. The measurements of the angular yields have been used as a calibration measurement to determine an effective thickness as production of a thin uniform carbon target has not been possible. The angular electron yields are integrated over all possible electron energies up to the primary energy of 1 keV. The yields have been compared to TRAX simulation results for varying target thicknesses. From TRAX classic simulations an effective thickness of  $3.6\mu\text{g}/\text{cm}^2$  (=15.9 nm) has been concluded to match the experimental yields for the carbon target with a nominal thickness of  $4.7\mu\text{g}/\text{cm}^2$  (=20.7 nm). The uncertainties in the experimental yields are assumed to be in the order of 15-25% [Lineva2008]. A comparison between TRAX classic simulations and experimental results is shown in Fig. 3.11 in [Lineva2008]. As electron cross sections for carbon have been modified for the present TRAX version and Auger electrons are now considered which present an additional source of low energy electrons, the simulation has been repeated. As differences in the yields due to different cross sections have not been significant (see Fig. 5.14), the assumed effective thickness should be still valid and has been taken for further simulations concerning the Toroid experiment.

An important observable after the transport of electrons through a material is the transmission spectrum. Energy-differential electron yields have been measured behind the carbon target after incidence of 1 keV electrons. Electron spectra are integrated over a certain angular interval. The angular zones which have been used in the Toroid experiments have a width of 30 degrees and are explained in Fig. 5.15. To obtain electron spectra for transmission and backscattering, several angular zones have been analyzed.

Previous TRAX classic calculations evaluated transmission and backscattering spectra and showed several deviations from experimental results. Two main aspects have been important for the transmission spectra which were supposed to be caused by the non-uniformities

---

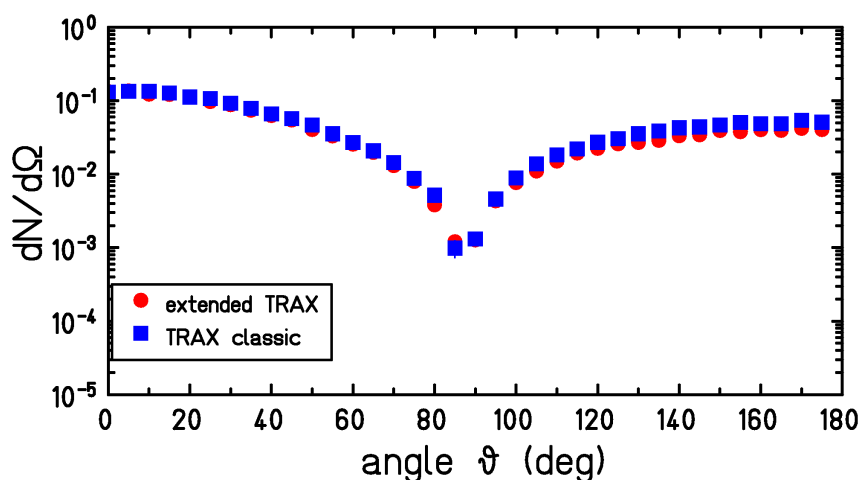


**Figure 5.14:** Simulations of the angular yield of electrons for 1 keV electrons incident on a carbon target for the TRAX classic and the extended version with modified cross sections. The comparison is needed to assure if the effective thickness  $3.6\mu\text{g}/\text{cm}^2$  considered from TRAX classic simulations is still valid for the extended TRAX. As there are no significant deviations the assumption of an effective thickness is considered to remain valid.

of the target. A zero-energy loss peak at the primary electron energy of 1 keV has been observed in the experimental spectra which could not be reproduced with TRAX classic. As this peak is clearly caused by holes or slits in the target, it has been necessary to introduce this kind of target non-uniformity in TRAX. After implementing the possibility of holes in the target, the experimental observation could be reproduced (Fig. 5.16). Furthermore, the position and width of the centroid of the energy distribution of electrons behind the target differed in simulation results and experimental data. In the experimental data, the position of the centroid appears at higher energies and is broader than in TRAX classic simulations. This shift in energy position can be explained by a decreased energy loss for electrons travelling through the target with fluctuating densities. Therefore, the extended TRAX version has been used to perform simulations with non-uniform targets accounting for varying densities. Four different target geometries have been used in TRAX simulations to show differences between a uniform target and targets with slits and varying thicknesses. The results are shown in Fig. 5.16. A uniform target shows no zero-energy loss peak at 1 keV and the position of the centroid of the energy loss peak is around 600 eV. The non-uniform target is represented by slits of 5 nm thickness between blocks with a length of  $10\mu\text{m}$ . The experimentally observed zero-energy loss peak is reproduced by simulation results. Introducing blocks with varying thicknesses (5% of the blocks with 8 nm or 10 nm instead of 15.9 nm thickness) leads to a shift of the centroid of the energy loss peak to higher energies. For the geometry type where 5% of the blocks had 8 nm thickness, the position and shape of the energy loss peak of the experimental data can clearly be reproduced. A reduced target thickness reduces the number of energy loss interactions. As different paths through the target are possible, electrons experience different target thicknesses. This leads to a broadening of the energy loss peak as the mean energy loss is smeared out. The chosen non-uniform geometries are largely simplified but allow to break down the effects on an electron transmission

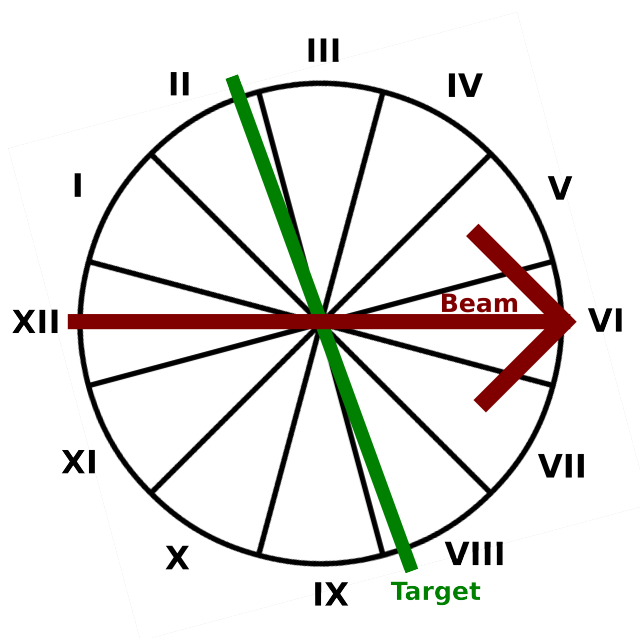


**Figure 5.15:** In the Toroid experiments, electron spectra have been measured in angular zones with a width of 30 degrees. In zones V, VI and VII, electron spectra are measured in forward (transmission) direction. In zones I, XII and XI, spectra are measured in backward direction. The target was rotated by 70 degrees with respect to the beam axis.

spectrum due to a non-uniform target in two basic considerations: slits to observe zero-energy loss electrons and thickness fluctuations to alter the mean energy loss.

---

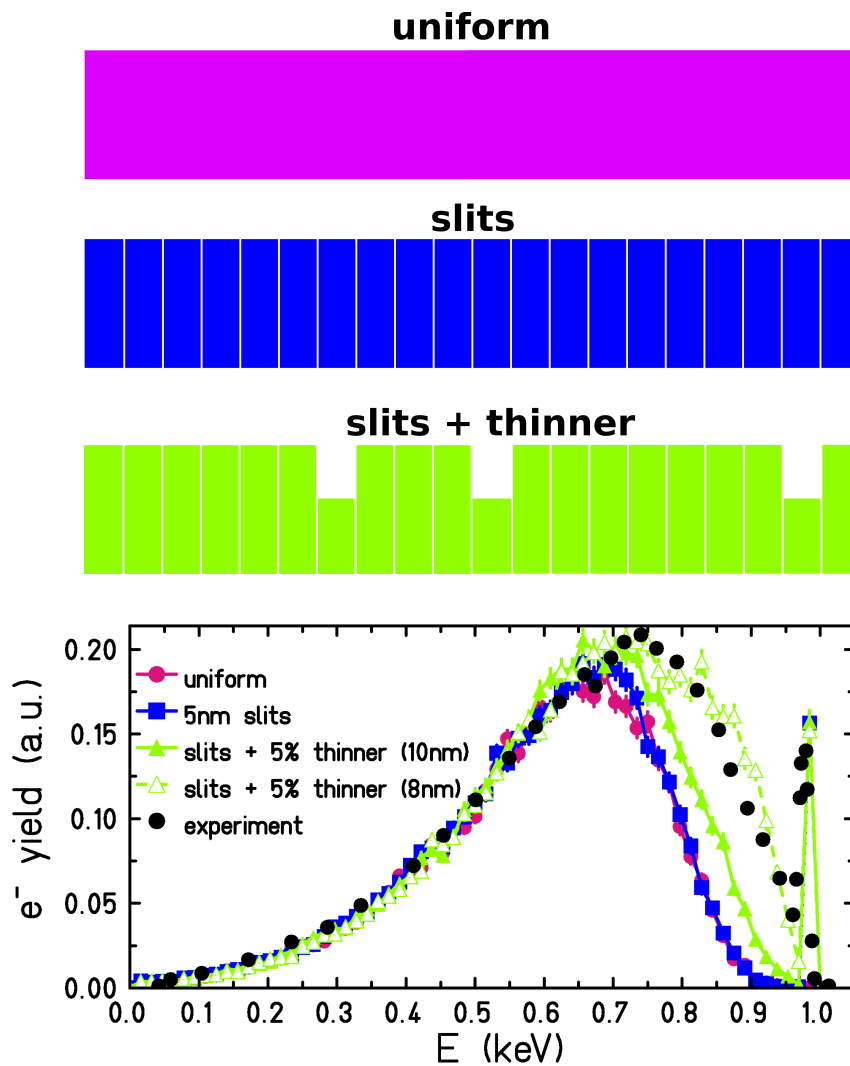


**Figure 5.16:** Energy resolved transmission spectra after incidence of 1 keV electrons on a 15.9 nm thick carbon target. Experimental data from the Toroid experiment are shown with black dots. The data have been obtained by carefully digitization of the VI section in Fig. 3.14. from [Lineva2008]. It shows the angular region 0-15 degrees from Fig. 5.15. The height of the electron loss peak was renormalized as absolute yields are unknown due to uncertainties in experimental scaling factors. TRAX simulated electron spectra are shown in pink for an uniform target, while the blue squares describe the result for a target with 5 nm slits between blocks of 10  $\mu\text{m}$  length. The data set represented by green triangles shows the results for a target with a reduced thickness of 8 nm/10 nm for 5% of the blocks.



---

## 5.2.2 Electron stopping powers

---

To determine the electron energy losses in the targets of interest for the Toroid experiment (C, Ni, Ag and Au), one has to use the correct cross sections, from which electron stopping powers can be derived. These stopping powers can be directly calculated from the cross sections and energy losses for electron ionization and electron excitation as shown in 5.1.1. The concept of using stopping powers to determine the energy loss of electrons inside a material rather than using individual cross sections is a very crude approximation for low energy electrons and does not contain important details around the ionization threshold. N. Lineva [Lineva2008] shows the result for a simple parametrized approximation for the stopping powers in Fig. 5.2 of her thesis. These values have been digitized and are shown with the resulting stopping power values from TRAX which are more sophisticated in Fig. 5.17. Absolute values for the stopping power deviate at energies below 200 eV and the shape of the TRAX curves is different. The region around 1-200 eV is the most critical where simple parametrizations can not give a realistic stopping power. TRAX includes all the details about shell-specific and individual excitation channels. Therefore, the start of an excitation channel at the energy threshold which is needed to allow this excitation is visible as an irregular edge in the stopping power curve. At low energies below the ionization threshold, excitation cross sections can show a pronounced maximum with a sudden decrease for increasing projectile energies. These details are usually not covered by simple parametrizations of the stopping power.

From the stopping power values which are a measure for energy loss in a material, one can

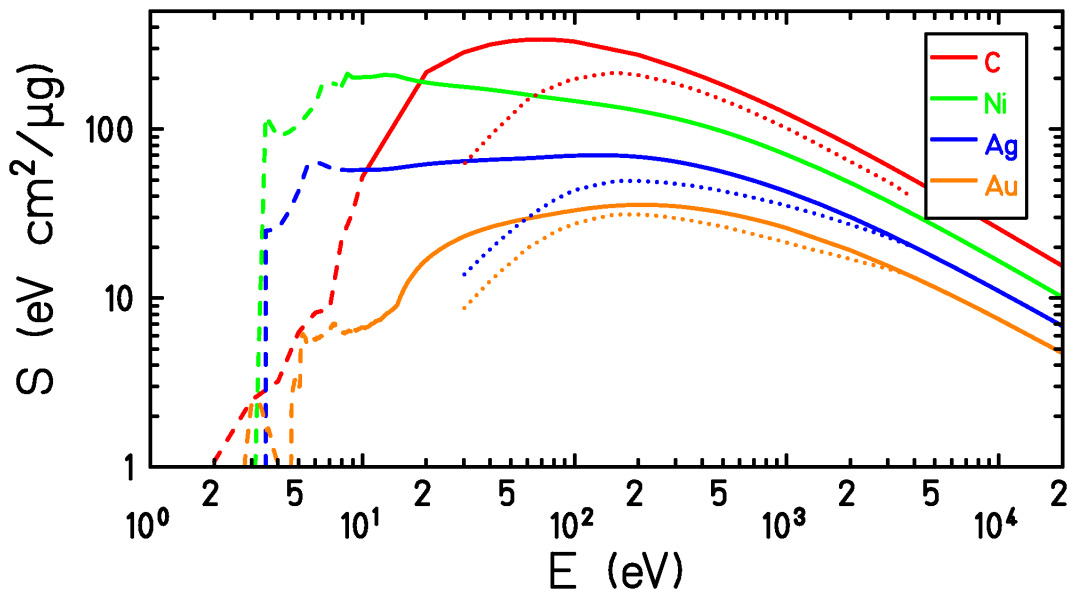


**Figure 5.17:** Stopping power values for electrons incident on target materials used in the Toroid experiments: C, Ni, Ag and Au. The values were calculated from cross sections and energy losses used in TRAX. Dashed extensions of the solid lines indicate that at these energies, only excitation does contribute to the energy loss. Dotted lines for C, Ag and Au are digitizations of the lines in Fig. 5.2 of [Lineva2008] and show largely simplified values for the electron stopping powers.

---

---

estimate which target thickness is needed to fully stop an electron of a certain energy by absorption. One idea of the Toroid experiment has been to use Auger electrons as probes for emission and transport processes. They are emitted isotropically at discrete energies. Auger electrons created in carbon have energies around 260 eV. For carbon and electron energies around 200 eV, the stopping power is about  $200 \text{ eV}\cdot\text{cm}^2/\mu\text{g}$ . Therefore, a target with a thickness of around  $1 \mu\text{g}/\text{cm}^2$  is needed to absorb an electron of this energy. Thicker targets require a more complex simulation scenario to account for Auger electrons created at varying depths. The targets used in the Toroid experiment had a nominal thickness of  $4.7 \mu\text{g}/\text{cm}^2$ . Therefore, most Auger electrons observed in experimental data are created near the surface, rather than deep inside the target. The extended TRAX version allows to perform complex simulations as it can directly account for the production and transport of Auger electrons.

---

### 5.2.3 Secondary electron creation and Auger electrons

---

Proton projectiles are the simplest type of ions as they have  $Z=1$  ( $Z$ : atomic number) and consist only of one nucleon. Protons incident on carbon targets create secondary electrons inside the target through ionization processes. When analyzing the secondary electron spectrum behind the carbon targets, we have to consider a combination of proton transport (ionization leading to the emission of secondary electrons) and electron transport (electrons losing energy on their way to the surface leaving the target). In a Toroid experiment described in [Lineva2008], carbon targets with a thickness of  $4.7 \mu\text{g}/\text{cm}^2$  have been irradiated with 8.77 MeV protons to measure the secondary electron production. Experimental data have been compared with TRAX simulations using the previous code version [Lineva2008]. An effective thickness of  $3.6 \mu\text{g}/\text{cm}^2$  has been assumed in the simulations for the carbon target according to the previous electron experiments. Secondary electron spectra have been measured up to an energy of 1000 eV [Lineva2008]. For comparisons with previous TRAX calculations, simulated yields have been renormalized to match experimental yields around 1000 eV, as the scaling of experimental data is not well known. Previous TRAX classic calculations could reproduce the part of the secondary electron spectra between 550 eV and 1000 eV, where no Auger electron peaks were visible. Below 550 eV, Auger electron peaks of oxygen and carbon were clearly visible in the experimental data but simulations with TRAX classic could not reproduce them. Auger electron peaks have been measured with edges at an energy of around 260 eV, which corresponds to an Auger transition after K-shell ionization in carbon, as well at an energy of around 540 eV, which corresponds to an Auger transition after K-shell ionization in oxygen. Therefore it has been concluded [Lineva2008], that the target surface has been contaminated with molecules containing carbon and oxygen from the residual gas in the measurement chamber, while the amount and exact composition of these molecules has not been further analyzed. Fig. 5.3 of [Lineva2008] shows the experimental data together with the TRAX classic simulations. The simulation from TRAX classic is shown in comparison with experimental data in Fig. 5.19. For enhanced visibility of the Auger electron peaks, the spectrum is not shown as an energy dependent yield  $dN/dE$ , but as an energy weighted yield  $E dN/dE$ . While the measurements only covered the solid angle with polar angle  $\theta$  from  $-180^\circ$  to  $180^\circ$  and azimuthal angle  $-1.3^\circ$  to  $1.3^\circ$ , the TRAX simulations have been performed for azimuthal angle  $0^\circ$  and polar angle  $0^\circ$  to  $180^\circ$  [Lineva2008].

With the extended TRAX code, Auger electrons are accounted for in the simulation. To account for the contaminations of the target including carbon and oxygen (i.e. CO resulting from surface oxidation), a simplified non-uniform target was assumed in the simulation (sketch Fig. 5.18).

---

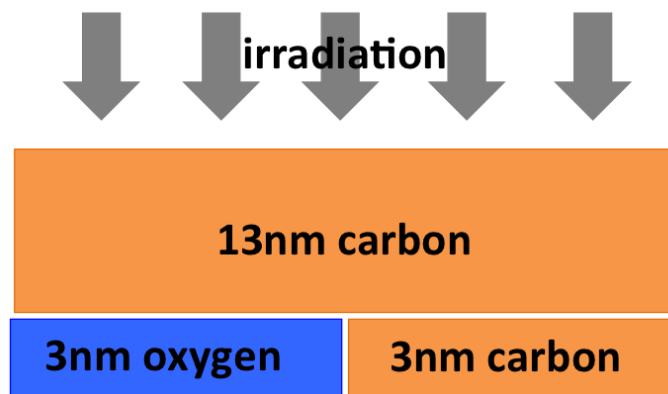


**Figure 5.18:** Simplified target geometry composed of 13 nm carbon plus 3 nm of carbon and oxygen, attached behind the exit surface of the carbon target. The carbon and oxygen attachments were simple solid blocks, each covering half of the irradiated target area.

A total target thickness of 16 nm is matching the effective target thickness of  $3.6\mu\text{g}/\text{cm}^2$  which has been used in previous simulations. A more sophisticated target geometry does not seem to be necessary, as neither the amount nor the exact composition of the contaminating molecules containing C and O is known. With the new simulations, the reproduction of the experimental spectrum could be largely improved as seen in Fig. 5.19. Auger electron peaks from carbon and oxygen are clearly visible in the TRAX simulation. This is also a proof of principle that the Auger process can be handled by TRAX. However, the exact shape, especially for the oxygen Auger electron loss peaks could not be reproduced. From the long tail of the Auger electron peaks towards lower energies, it can be guessed, that the Auger electrons must have been emitted deeper inside the material which could be explained by molecules which have not been attached to the surface but have penetrated inside the target material. As the carbon target has shown clear indications for non-uniformities (including slits and holes), it might be possible that molecules attached to the carbon target inside these holes. A long tail of an energy loss peak is caused by a broad distribution of energy losses of the Auger electrons. According to the used database for Auger electron probabilities [PeCu1991], a K shell ionization in oxygen leads to the production of three different Auger electron energies from five transitions. By reducing the energy bin size for the histogram produced by TRAX, these transitions become visible as separate peaks. In the experiment, the energy resolution is considered to be smaller than the difference in energy between these transitions. Table 5.1 shows the Auger transition probabilities and energies for oxygen and carbon after K-shell ionization. Considering in detail all possible Auger electron transitions for carbon and oxygen allows to reproduce the indication of a multiple peak structure in the simulated spectra.

Further deviations between experimental and simulation results, especially in the low energy region below 100 eV are supposed to be caused by non-perfect proton cross sections. The ionization description, based on the binary encounter approximation, should be improved in the future.

---

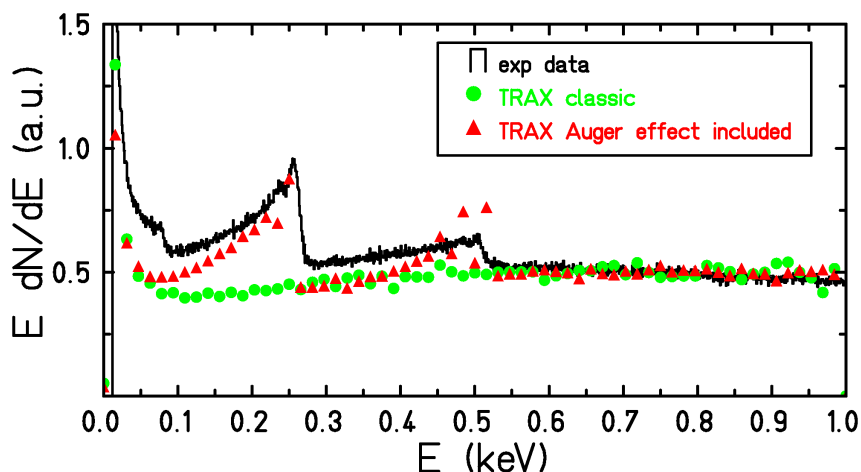


**Figure 5.19:** Secondary electron energy spectra after incidence of 8.77 MeV protons on a  $4.7\mu\text{g}/\text{cm}^2$  carbon target. The experimental data, shown in black, have been scaled to match the simulated yield around 1 keV according to [Lineva2008]. While the nominal target thickness has been  $4.7\mu\text{g}/\text{cm}^2$ , TRAX simulations have been performed for  $3.6\mu\text{g}/\text{cm}^2$ . TRAX classic calculations are shown in green. Auger electrons are not included in the classic simulation but the energy dependency of the electron yields above about 550 eV can be reproduced. Simulation results based on the extended version are shown in red. The yields inside the Auger electron peaks do not perfectly match as the exact composition and amount of adsorbents is not known. Simple atomic C and O was attached to the target to result ion Auger electron peaks from both materials. The chosen energy resolution for TRAX is 15.62 eV/bin.

oxygen			carbon		
transition	probability (%)	energy (eV)	transition	probability (%)	energy (eV)
1-2-2	17.86	460	1-2-2	41.36	251
1-2-3	11.62	488	1-2-3	40.73	256
1-2-4	23.04	488	1-3-3	17.72	262
1-3-4	29.11	516			
1-4-4	16.68	516			

**Table 5.1:** Auger transitions after K-shell ionization of oxygen and carbon with probabilities given by [PeCu1991]. As for oxygen, shell 3 and 4 are considered to have the same binding energy, the corresponding Auger transition energies do not differ.

---

## 5.2.4 Range of Auger electrons

---

As Auger electrons have been intended to be used as probes for electron transport processes, further investigations have been performed. To obtain information about their creation point and about their energy losses, the energy distribution in the Auger electron peak could be used. A problem with this approach appeared in the Toroid experiments as the range of carbon Auger electrons is lower than the target thickness. Some Auger electrons are stopped already inside the target and the secondary electron spectrum shows only Auger electrons created at the surface and in outer layers of the target.

Previous simulations have been performed [Lineva2008] to determine the range of electrons with 262 eV in carbon with the classic TRAX code. These simulations have been repeated with the extended TRAX version since due improved cross sections, stopping powers have changed. Newly included excitations enhanced the electron stopping power resulting in a reduced electron range. Fig. 5.20 shows simulated angular electron yields for isotropically emitted monoenergetic electrons with 262 eV after travelling through a carbon target of a certain thickness. Simulation results are compared for TRAX classic and the new extended version. Yields are decreasing faster with increasing target thickness in the new simulation results due to the enhanced inelastic cross sections.

To further investigate the propagation of Auger electrons in carbon, additional simulations

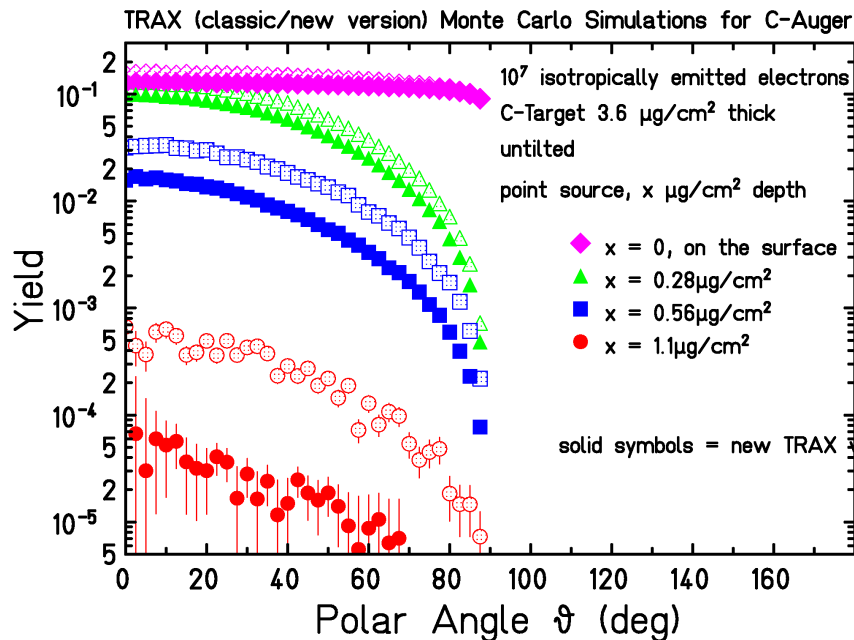


**Figure 5.20:** Angular yields of 262 eV carbon KLL Auger electrons in carbon, normalized per projectile. The depths in  $\mu\text{g}/\text{cm}^2$  correspond to depths 0 nm, 1.2 nm, 2.4 nm and 4.8 nm, respectively. At a depth of 4.8 nm, almost all Auger electrons are absorbed in the target.

with the new TRAX version have been performed to obtain energy resolved transmission spectra. Again, a mono-energetic electron source with an energy of 262 eV has been used and transmission spectra have been calculated after a certain target thickness. The results are shown in

---

Fig. 5.21 . The transmission spectra show, that not only the yield of Auger electrons is very much decreased already for a target thickness of about 2 nm, but that also the energy distribution of the Auger electrons shifts to lower energies as their mean energy is decreased by several inelastic collisions. Furthermore, their energy distribution does not only change in the position of the centroid, but also broadens, leading to the effect that Auger electrons emitted from 4 nm inside the target cannot be identified by their energy as no clear maximum can be observed.

The range of 262 eV Auger electrons in carbon is not precisely defined due to range strag-

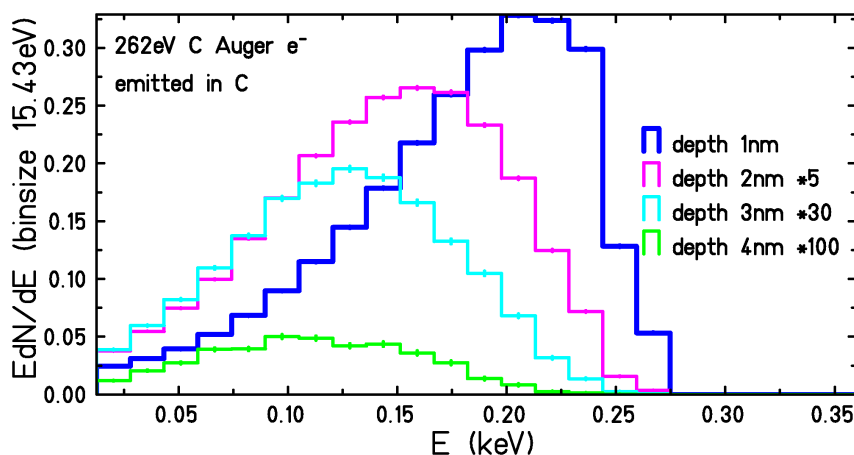


**Figure 5.21:** Energy dependent yields of 262 eV carbon KLL Auger electrons in carbon after travelling through layers of varying thickness. The yields for larger depths have been scaled by the indicated factor as the total yield is reduced by absorption. One can clearly see how much the Auger peak flattens, due to a broad range of energy losses.

gling. However, a transmission probability can be considered to determine the range of Auger electrons in carbon. TRAX simulations have been performed to determine the transmission coefficients as a function of target thickness. Simulation results are shown in Fig. 5.22 and show the ratio of electrons of all energies that could be detected in the forward half plane behind the carbon target normalized by the number of incident projectiles. For a target thickness of 4 nm, the transmission rate drops below 0.1%.

Additionally to the considerations for the carbon Auger electrons, further simulations have been evaluated to determine the range of oxygen Auger electrons in carbon. This can be useful to determine how deep inside the target, oxygen contaminations must have been present to create an oxygen Auger electron peak as seen in the experimental data from the Toroid spectrometer. The same simulations as for carbon Auger electrons have been performed for oxygen Auger electron with an energy of 516 eV using the extended TRAX version. The angular electron yield as a function of target thickness can be seen in Fig. 5.23. The range of 516 eV is high enough that electrons emitted isotropically from a source depth of around 4.8 nm can leave the target through the backward plane. For the simulation of angular dependent yields, a carbon target with a thickness of 15.9 nm has been assumed.

Transmission spectra for 516 eV electrons incident on a carbon target with varying thickness can be seen in Fig. 5.24. Oxygen Auger electrons transmitted through 4 nm of carbon still show a defined energy loss peak rather than a broad distribution. However, the peak broadens with increasing target thickness and the centroid is shifted to lower energies as the average energy loss

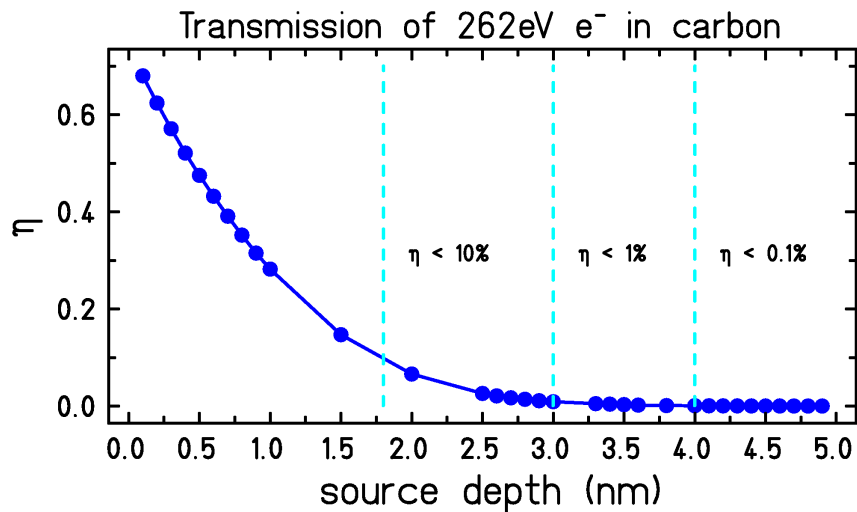


**Figure 5.22:** Transmission factor  $\eta$  for 262 eV carbon KLL Auger electrons in carbon as a function of depth. The transmission yields have been integrated over all forward directed polar angles (0-90 deg).

increases. The spectrum of one of the Toroid experiments, showing secondary electrons emitted from carbon after proton incidence (Fig. 5.19), shows enhanced secondary electron yields due to oxygen Auger electrons around 270 eV-520 eV. The oxygen Auger peak is clearly visible with a long tail toward lower energies caused by oxygen Auger electrons which suffered energy losses. Even below 300 eV, the yield is significantly enhanced and must be induced by oxygen Auger electrons emitted at various depths. The transmission spectra for oxygen Auger electrons in Fig. 5.24 show, that a target thickness of at least 4 nm is needed to obtain a significantly large electron yield at energies of around 300 eV. Therefore, it can be concluded, that oxygen Auger electrons must have been emitted at depths as high as 4 nm. This would mean that the contaminations of the target in the Toroid experiments from molecules consisting of carbon and oxygen might have penetrated inside the carbon target through holes and slits. Another explanation would be that some parts of the target must have been as thin as around 4 nm to obtain the additional electron yield from surface contaminations at the other side of the target. TRAX simulations accounting for these contaminations used an already generous 3 nm oxygen layer on the surface and could not reproduce the experimental yields around 300 eV. Transmission coefficients for 516 eV electrons through carbon are shown in Fig. 5.25. A transmission of less than 0.1% of the oxygen Auger electrons is reached after 9.5 nm of carbon.

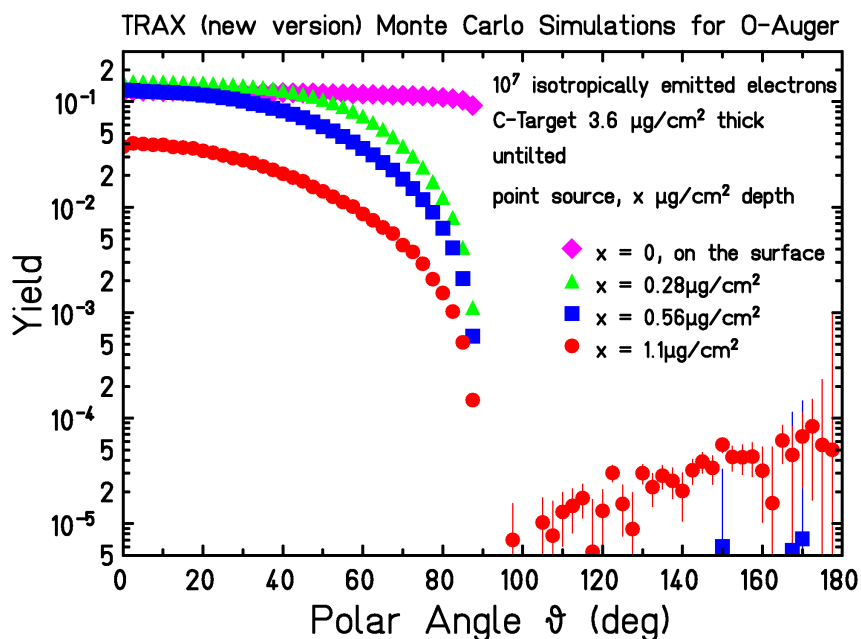


**Figure 5.23:** Yields of 516 eV oxygen KLL Auger electrons in carbon. The indicated depths in  $\mu\text{g}/\text{cm}^2$  correspond to depths 0 nm, 1.2 nm, 2.4 nm and 4.8 nm, respectively. The yield is higher at lower energies for small depths as the electrons produce further low energy secondary electrons and the yield is integrated over all electron energies. At larger depths, the range of oxygen KLL Auger becomes larger than the total target thickness minus the source depth which leads to electrons escaping the target at the other surface as the electron source is isotropically.

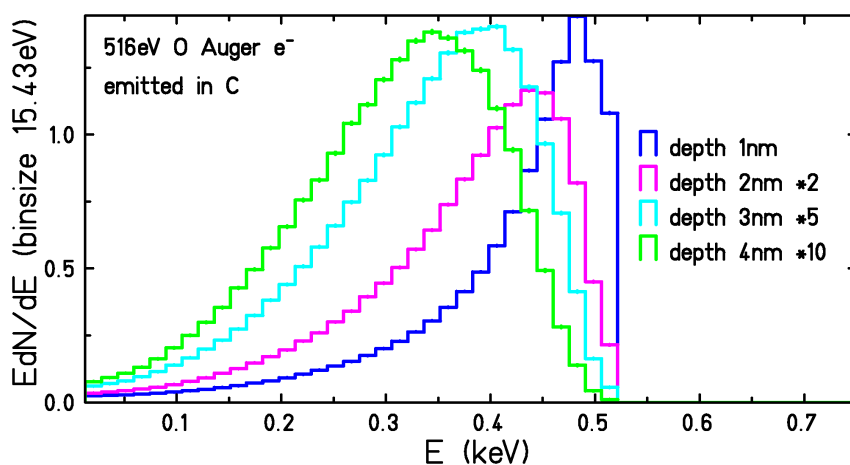


**Figure 5.24:** Yields of 516 eV oxygen KLL Auger electrons in carbon after travelling through a certain thickness. The yields for higher depths have been scaled by the indicated factors as the total yield is reduced by absorption.



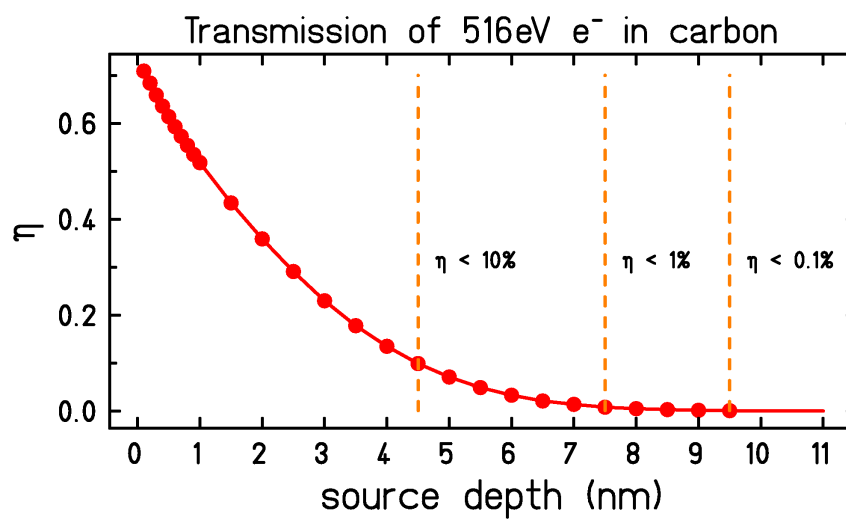


**Figure 5.25:** Transmission factor  $\eta$  for 516 eV oxygen KLL Auger electrons in carbon as a function of depth. At a depth of 9.5 nm, the transmission rate drops below 0.1%.

---

---

## 5.2.5 Electron emission cross sections for carbon projectiles

---

In the framework of the Toroid experiments,  $C^{2+}$  ions with an energy of 3.6 MeV/u and 11.4 MeV/u were used as projectiles incident on targets consisting of C, Ni, Ag and Au [Lineva2008]. This experiment has been intended to serve as a pilot project to measure electron emission from solids [Lineva2008]. From the measured emitted electron yields, an energy dependent electron production cross section has been calculated. Many scaling factors have to be applied to obtain a cross section from the measured electron yields in each channel (=energy bin). In [Lineva2008] the normalization formula is given including scaling factors considering the number of projectiles, the number of active target electrons (scattering centers), the energy acceptance of the spectrometer for the given energy, the covered solid angle and the detection efficiency.

Within the Toroid experiments, this is the most complex experiment concerning analysis, as both ion transport and secondary electron transmission and transport have to be understood. For comparison, cross sections for electron emission have been calculated using the modified Rutherford formula which is valid for electron emission from gaseous targets [Lineva2008]. The formula depends on electron binding energies for all shells of the considered target material. As the binding energies used in [Lineva2008] could not be obtained, the results for the modified Rutherford formula have been digitized from Fig. 5.6 and Fig. 5.7 of [Lineva2008]. The mentioned modified Rutherford formula to calculate electron emission cross section includes a parameter to adjust to smaller energies and is given by [StDu1997]:

$$\frac{d\sigma}{dE_{e-}} = \frac{\pi \cdot Z_p^2 \cdot e^2}{\epsilon_p \cdot (c \cdot |E_{bnd}| + E_{e-})^2} \quad \text{with } c = \left[ \ln \left( \frac{2\epsilon}{E_{bnd}} \right) \right]^{-1/2} \quad (5.2)$$

$E_{bnd}$  denotes the electron binding energy, while  $E_{e-}$  is the kinetic energy of ejected electrons.  $Z_p$  corresponds to the projectile charge, while  $\epsilon_p$  is the projectile energy. The logarithmic dependency on projectile energy  $\epsilon_p$  is included in parameter  $c$ .

The main drawback of the modified Rutherford formula is that it can not reproduce the relative magnitudes of the experimentally obtained electron emission cross sections for C, Ni, Ag and Au. Theoretical emission cross sections for 3.6 MeV/u  $C^{2+}$  ions from the modified Rutherford formula have been highest for nickel, followed by carbon, silver and gold. Experimental data showed a different order, with highest emission cross sections for carbon, followed by gold, silver and nickel. Due limited availability of cross sections, simulations with TRAX classic have only been performed for carbon as a target material.

Therefore, new simulations have been performed using the extended TRAX version to obtain electron energy spectra which have to be converted to emission cross sections by a range of normalization factors. In the simulations, an effective charge has been assumed as TRAX currently does not handle projectile ionization and electron capture. The effective charges to be used are given in [Lineva2008] and are listed in table 5.2. TRAX allows the calculation of an electron energy distribution which is given as an energy dependent yield  $dN/(dE \cdot d\Omega)$  with units  $[1/(\text{keV} \cdot \text{sr})]$ . To convert this yield to a cross section  $d\sigma/dE$  with units  $[\text{cm}^2/\text{eV}]$ , the yield has been multiplied with the following normalization factor:

$$\frac{1 \text{ keV}}{1000 \text{ eV}} \cdot \frac{4\pi}{N_{\text{target atoms}} \cdot N_{\text{active e-}}} \quad (5.3)$$


---

with

$$\frac{1}{N_{\text{target atoms}}} = \frac{M_{\text{mol}}[\text{g/mol}]}{\text{target\_thickness}[\text{g/cm}^2] \cdot N_{\text{Avogadro}}[1/\text{mol}]} \quad (5.4)$$

In [Lineva2008], the number of active electrons are given in a table which have been used to obtain normalization factors to obtain electron emission cross sections from TRAX electron spectra. The calculated normalization factors are given in table 5.2.

target	thickness ( $\mu\text{g/cm}^2$ )	active e <sup>-</sup>	normalization factor	projectile
C	3.6	6	1.159E-20	3.6MeV/u C4+
C	4.7	6	8.879E-21	3.6MeV/u C4+
Ni	45	26	1.047E-21	3.6MeV/u C5+
Ag	38	37	1.274E-22	3.6MeV/u C4.2+
Au	40	51	1.600E-22	3.6MeV/u C3.5+
C	3.6	6	1.159E-20	11.4MeV/u C4+
C	4.7	6	8.879E-21	11.4MeV/u C4+
Ni	45	26	1.047E-21	11.4MeV/u C5.1+
Ag	38	45	1.048E-22	11.4MeV/u C4.4+
Au	40	69	1.185E-22	11.4MeV/u C3.7+

**Table 5.2:** Used targets and projectiles for the simulations in Fig. 5.27 and Fig. 5.28. The results for the normalization factors are given with which TRAX energy dependent electron yields have been scaled to obtain electron emission cross sections.

---

### Carbon target

---

In previous simulations (Fig.5.8 in [Lineva2008]) using the classic TRAX version, the cross sections for electron emission after incidence of C<sup>2+</sup> ions on the carbon target could not be reproduced satisfactorily. TRAX results have been scaled at an energy of around 50 eV to match experimental cross sections (derived from measured electron yields) as the correct scaling of the experimental data is unknown. However, above an energy of around 100 eV, TRAX failed to match the shape and absolute values of the experimentally measured curve. Besides, TRAX classic simulations could not consider a rotated target, while the target in the experiments has been tilted by -20 degrees as indicated in Fig. 5.15. Using the new TRAX version allowed to improve on this. The comparison between experimental data and TRAX results can be seen in Fig. 5.26 on the left hand side. The consideration of the rotation of the target has a minor influence on the results, it leads to a slight increase in overall values. The carbon Auger electron peak at around 260 eV can now be reproduced qualitatively. The target assumed in the simulations contained no C- and O-contaminations, which resulted in a higher Auger electron peak than in the measurement results. In contrast to previous calculations, the cross sections from simulations and experiment are now matching in the range between about 260 eV and 600 eV. Above 600 eV TRAX still underestimates the measured results which is supposed to be caused by the cross sections for the carbon projectiles which are based on a simplified method to describe electron emission.

For carbon ions with an incident energy of 11.4 MeV/u, previous TRAX classic calculations could

---

already reproduce the results for electron emission cross sections apart from the Auger electron peaks. Simulations using the new TRAX version allowed to reproduce the experimental data including the Auger electron peak which can be seen on the right hand side of Fig. 5.26. An adaptation that had to be made has been the use of an effective charge of 4+ instead of the experimental value of 2+ or the theoretical value of 3+ [Lineva2008]. The value of 2+ is supposed to be the charge state of ions leaving the accelerator. Due to electron capture and projectile ionization, the charge state can change. The effective charge represents the average value inside the target. The experimentally observed Auger peak is slightly lower in intensity. This can be explained by oxygen contaminations which can alter the carbon Auger electrons. In the experimental data, a structure indicating the Auger electron peak from oxygen is visible. In this simulation, a basic carbon target without any additional contamination material has been used.

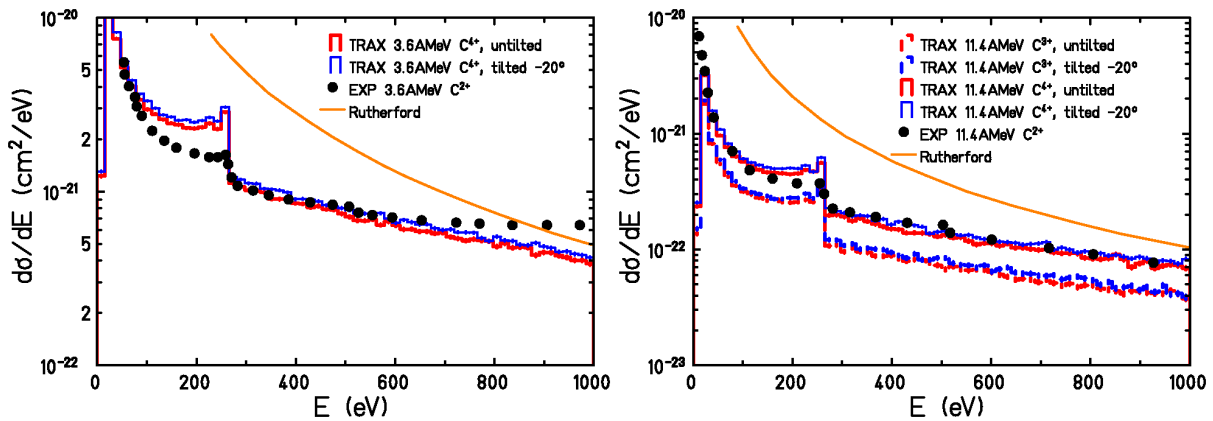


**Figure 5.26:** Electron emission spectra for 3.6 MeV/u (left plot) and 11.4 MeV/u (right plot) C<sup>2+</sup> ions incident on carbon. TRAX results have been scaled to match experimental data at around 50 eV as mentioned in [Lineva2008]. A constant charge of 4+ has been considered inside the target as it has been done in [Lineva2008].

---

### Nickel, silver and gold targets

---

For nickel, silver and gold targets, no previous simulations existed. TRAX simulations using the extended code have been performed and scaled with the derived normalization factors given in table 5.2. Experimental data as well as theoretical cross sections using the modified Rutherford formula have been digitized from Fig. 5.6 of [Lineva2008]. The comparison between simulations and experiments can be seen in Fig. 5.27 and TRAX results allow to reproduce the experimentally observed order of magnitudes reasonably well. Emission cross sections are highest for carbon, followed by gold, silver and nickel. However, the absolute magnitude of carbon differs a lot between simulation results and experiments. As the experimental scaling is not known precisely, this can be an explanation for deviations. No C- and O-contaminations have been added to the targets in the TRAX simulations which explain deviation from experimental result which contain peaks with large tails towards lower energies with an edge at around 260 eV and 516 eV. Emission cross sections are based on the binary encounter approximation to account for ionization through carbon projectiles. The binary encounter approximation is known to overes-

---

timate the emission at small energies which might explain further deviations in the low energy region.

For the other projectile energy of 11.4 MeV/u, TRAX simulations have been performed as well.

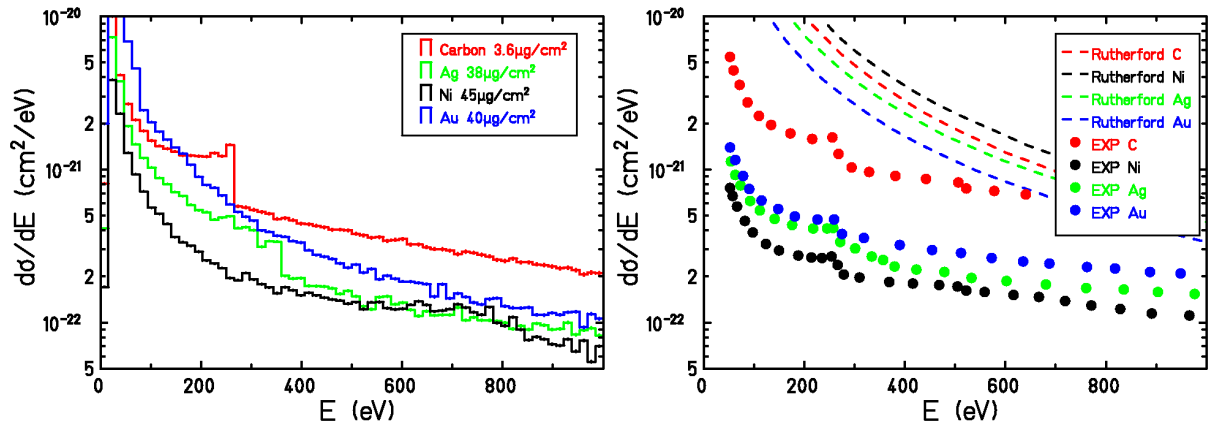


**Figure 5.27:** Electron energy spectra from 3.6 MeV/u C ions incident on C, Ni, Ag and Au. Left: TRAX simulations using the extended cross sections and elastic scattering description according to PWA. Right: Experimental data and theoretical results from modified Rutherford formula from Fig. 5.6 of [Lineva2008].

The comparison with experiments can be seen in Fig. 5.28. Again, TRAX can reasonably reproduce the correct order of magnitudes for the emission cross sections for all target materials, which has not been possible using the modified Rutherford cross section. As the targets have not been thin enough to contain only a few atomic layers, a combination of electron emission and transport is seen in the spectra. The normalized emission cross sections, obtained from the measured electron yields, are modified by energy losses and absorption and should therefore be lower than the predicted theoretical emission cross sections. As TRAX can follow all the details of electron emission and transport, TRAX simulation results are in much better agreement with experimental data than analytical estimates. The accuracy of the simulation results is limited by the electron emission cross sections for carbon ions. At low energies, electron emission cross sections are higher for Ag than for Ni. At increasing energy, the order changes. This trend can be reproduced by TRAX simulations which is an indication for a correct choice of the used electron cross sections correctly describing the transport of low energy electrons.

In [Lineva2008], the visibility of Auger transitions in experimental data for electron emission from nickel and silver foils has been mentioned. For the Ag-target, MNN-transitions around approximately 250 eV, 280 eV and 320 eV are supposed to be visible in the secondary electron energy spectra. For the Ni-target, LMM transitions are supposed to be visible at energies of around 700 eV, 780 eV and 880 eV [Lineva2008]. As the extended TRAX considers the production of Auger electrons, simulations have been performed to obtain electron spectra containing energy dependent yields for secondary electrons after incidence of 11.4 MeV/u C ions on Ag and Ni. Auger transitions that can occur are numerous. Considering MNN-transitions in Ag, there are 5 shells labelled as M shells and 5 shells labelled as N shells between which a total number of 55 possible Auger transitions have been considered, while some are more probable than others. Therefore, sharp peaks cannot be expected in the spectra. However, regions of

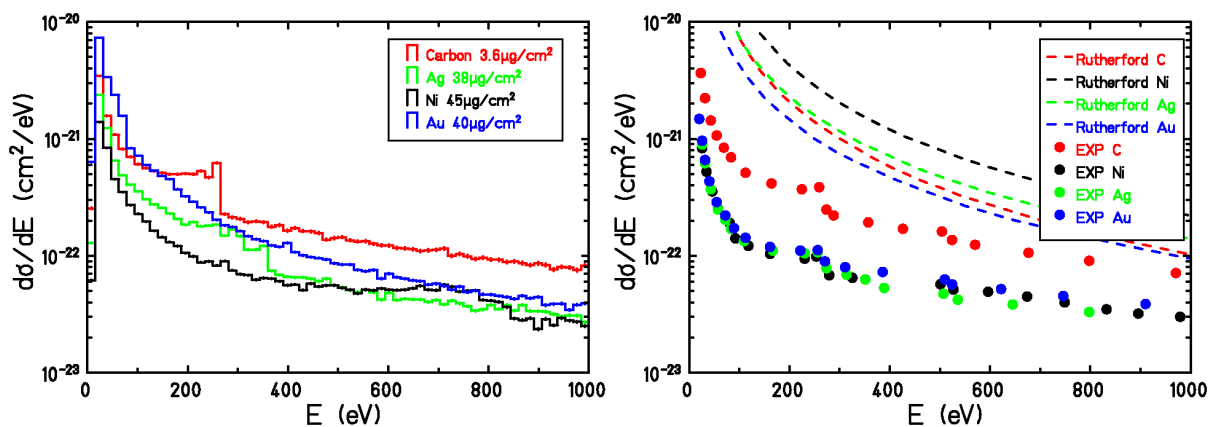


**Figure 5.28:** Electron energy spectra from 11.4 MeV/u C ions incident on C, Ni, Ag and Au. Left: TRAX simulations using the extended cross sections and elastic scattering description according to PWA. Right: Experimental data and theoretical results from modified Rutherford formula from Fig. 5.7 of [Lineva2008].

enhanced electron yields can be identified which are marked in the Ag spectrum (see Fig. 5.29), caused by Auger electrons from MNN-transitions.

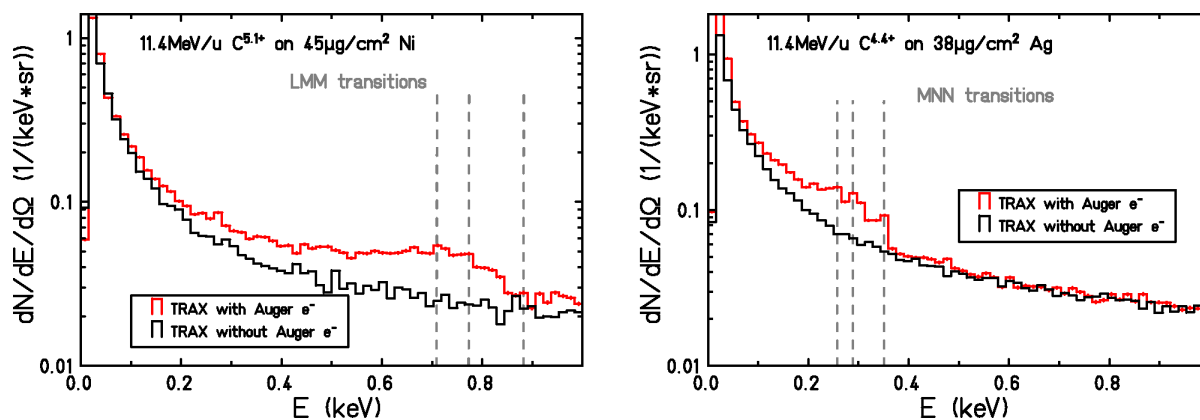


**Figure 5.29:** TRAX simulated secondary electron energy spectra for 11.4 MeV/u C ions incident on Ni (left) and Ag (right) are shown using the extended cross sections and elastic scattering description according to PWA. For illustration, simulations have been performed with and without consideration of the Auger effect. LMM-transitions for Ni and MNN-transitions for Ag are visible in the simulations. However, numerous transitions are possible, slightly different in their energies which is why Auger electrons can not always be observed as sharp peaks. Dashed lines indicate the energies at which transitions have been observable in experimental data of the Toroid experiment [Lineva2008].

---

## 6 Microscopic radiation damage

A common tool to describe microscopic damage is the radial dose distribution which has been described in section 2.2. As different approaches to obtain the radial dose distribution do not agree at small radial distances below about 10 nm and this area is of special importance for several applications, one goal of this thesis has been to find a physically realistic dose for small radii down to  $r=0$  using the TRAX simulation code.

The radial dose distribution can be directly obtained as an output parameter of TRAX without having to make any assumptions. A large number of tracks is evaluated by repeating the simulation with many projectiles. The average effect per single projectile can then be calculated by normalization. From the position of the inelastic scattering events, a radial distance from the track center can be derived. The radial dose is evaluated inside a cylinder. Usually, radial bin sizes are chosen with a logarithmic spacing as the dose falls off rapidly approximately as  $1/r^2$ . To obtain the dose in Gray, the energy deposition is divided by the cylindrical volume, the density of the target material ( $1\text{g/cm}^3$  for  $\text{H}_2\text{O}$ ) and normalized to a single ion. The following formula is applied in TRAX [Kraemer1995]:

$$D_r(r)[\text{Gy}] = \frac{\sum_z D(r^2, z)[\text{keVcm}^{-3}] \cdot 1.602189 \cdot 10^{-13}}{2 \cdot \pi \cdot r \cdot \Delta r \cdot (z_{\max} - z_{\min}) \cdot \rho \cdot N_{\text{ions}}} \quad (6.1)$$

MC simulations usually reproduce the  $1/r^2$  dependency predicted by analytical models at intermediate radial distances. But in the innermost part of the track, large uncertainties in the radial dose distribution can occur. In this chapter, different considerations are discussed which can influence the simulation results for the radial dose distribution at small radii. Further TRAX extensions have been performed to provide further insights in the microscopic radiation damage.

---

### 6.1 Choice of $r_{\min}$

---

For the evaluation of  $D(r)$  with TRAX, a radial binning has to be defined including a minimum radius  $r_{\min}$  for the first bin. The binning is usually chosen logarithmically as the radial dose decreases rapidly with increasing radii. The zero radius bin contains the dose at  $r=0$  which considers all energy depositions between  $r=0$  and  $r=r_{\min}$ . All energy depositions directly caused by the primary projectile are considered to be along the ion track at  $r=0$ . If the choice of  $r_{\min}$  is very small, the volume of consideration decreases. As the radial dose is calculated by division by the cylindrical volume, the result will lead to a larger dose values. Effects due to a different chosen  $r_{\min}$  on TRAX results for the radial dose distribution of 1 MeV/u protons incident on water can be seen in Fig. 6.1. Considerations about a reasonable choice of  $r_{\min}$  are discussed in the following sections. Experimental data exist [WiBa1976] which have been obtained from measurements in gaseous targets scaled to liquid water density. TRAX calculations agree with experimental results which are only available down to simulated distances around  $r=1$  nm. TRAX allows the calculation for smaller radii. As a minimum radius has been chosen for the first bin, all dose which is deposited at radii below  $r_{\min}$  is accounted for in the  $r=0$  bin. Thus

a "step" in the dose distribution can be observed between the zero radius bin and the following bins. The question is, whether this "step" is realistic or if any reasonable physical effects can change the dose distribution, smoothening the transition from the zero bin to the first bin. The step can cause problems as several models like LEM use the radial dose as an input parameter and are very sensitive on values for the radial dose at  $r=0$ . In the following sections, physical considerations that have an impact on the radial dose distribution at radial distances below a few nanometers are discussed.

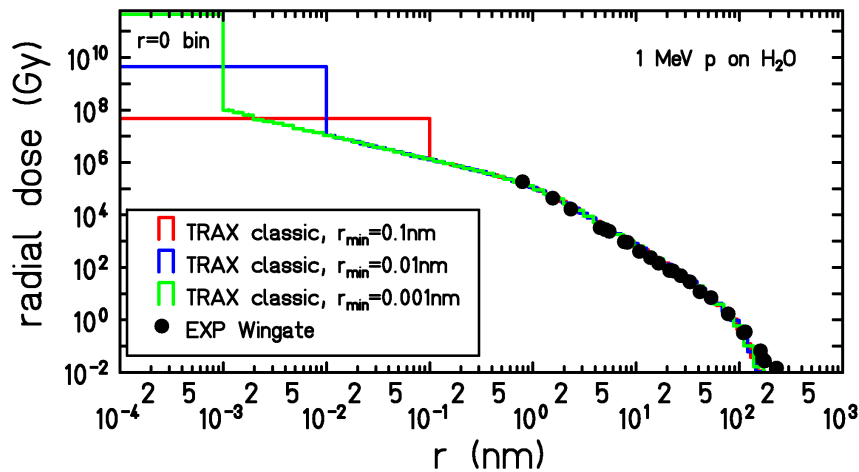


**Figure 6.1:** In TRAX, a minimum radius  $r_{min}$  below which the "zero" radial bin is evaluated has to be defined. All energy depositions below this radius are considered to be inside the core. The choice of the minimum radius changes the radial dose in the zero bin critically. A smaller radius leads to a lower value and therefore an increased dose.

## 6.2 Elastic Scattering of Ions

The elastic scattering of ions is often neglected in track structure Monte Carlo simulations as the effect is small compared to electron elastic scattering. The contribution of elastic ion scattering is small on the macroscopic scale as the scattering width is much smaller than 1% compared to the travelling distance. Most MC codes consider the so called multiple scattering effect of ions by folding a distribution to the simulation results at the end of a simulation process to get the correct width of the ion beam. For the latter procedure, parametrizations for multiple scattering are needed. Molière describes the effects of multiple scattering on the angular distribution of ions [Molière1948]. The result is a shape similar to a Gaussian distribution with a larger tail. Much simpler parametrizations for the angular width of an ion beam after a given target thickness are provided by simple formulas given by Highland and Lynch and Dahl [Highland1975, LyDa1991]. The parametrizations differ for thin or thick targets and rely on parameters like the radiation length in a certain target material. The accuracy of parametrized descriptions is limited. By considering the elastic scattering of ions directly in the Monte Carlo simulation it is possible to obtain a much higher accuracy as long as all interactions are correctly described. It is possible to directly extract the angular width of the beam at any surface of the target geometry.

TRAX has been extended to include this interaction using screened Rutherford cross sections



as mentioned by Berger [Berger1963]. A factor in the description of the screening parameter has been changed to adapt the parametrization from electrons to protons or ions. The factor includes a term accounting for the difference in projectile mass. The screening parameter for ions can be described as:

$$\eta = Z_{Target}^{2/3} \cdot 1,75 \cdot 10^{-5} \cdot (M_{e^-}/M_{ion})^2 \cdot \eta_c \cdot (1/\beta^2 - 1) \quad (6.2)$$

The resulting total cross section for the elastic scattering of ions then is:

$$\sigma_{total} = \left( \frac{1}{2 \cdot \eta} - \frac{1}{2 \cdot \eta + 1} \right) \cdot 2 \cdot \pi \cdot \frac{(\alpha \cdot \hbar \cdot c)^2 \cdot 10^{-26}}{(E_{kin} + E_0 \cdot \beta^2)^2} \cdot N \cdot Z_{Target} \cdot (Z_{Target} + 1) \cdot Z_{proj} \cdot Z_{proj} \quad (6.3)$$

with constants  $\alpha = 1/137$  and  $c$  being the speed of light,  $E_0$  the rest mass of the projectile and  $N$  being the neutron number of the target material.

A technical difficulty in the implementation of hard-coded differential cross sections for the elastic scattering of ions is the choice of reasonable angular stepsizes to handle all kinds of ions. Usual deflection angles are small and they decrease with increasing mass of the ion projectile. To avoid sampling of too large angles, a linear tabulating of angles cannot be used. A logarithmic step size is also not suitable as low angles should be distinguished with more precision. Depending on the chosen ion projectile, a different scale for probable scattering angles can be necessary. Therefore, a semi-logarithmic tabulating method has been chosen. Six different intervals are defined in which the angle step size is chosen to be linear and 128 values per interval are defined. The intervals themselves are somehow spaced in a semi-logarithmic way: [0,0.0001], [0.00011, 0.001], [0.0011, 0.01], [0.11,1], [1.1, 180]. The intervals are combined, leading to a feasible table size of 768 angular values for which differential cross sections are calculated. In the simulation routine, an angular value from the table is derived when a scattering event is sampled. The implementation has been tested extensively to assure that simulation results do not depend significantly on the choice of table step sizes. Illustrations of the simulated tracks of ions through the target material of consideration show, that for a geometry with a length of a few micrometer, the typical size of a biological cell, the elastic scattering of ions does deflect the ion tracks by a few nanometers in lateral direction. A TRAX simulation showing tracks of 11.9 MeV/u carbon ions in water can be seen in Fig. 6.2.

---

### 6.2.1 Validation simulations

---

To validate the correct implementation of the elastic scattering of ions, comparisons of simulation results with experimental results have been made. Additionally, comparisons with multiple scattering parametrizations by Highland and Lynch and Dahl [Highland1975, LyDa1991] have been performed. Gottschalk et al. [Gottschalk1993] have measured the angular spread of 158.6 MeV protons after passage through solid state targets. The target materials ranged from low Z materials such as beryllium to high Z materials such as uranium. Different thicknesses were used, from thin targets, where energy losses were negligible, up to targets with thicknesses above the mean proton range [Gottschalk1993]. Gottschalk quantified his results through the width of the angular distribution and concluded that in the small angular region the differences between a Molière scattering distribution and a Gaussian shape are small. Therefore it is possible to perform a fit of a Gaussian distribution to the experimental or simulated data, which is

---

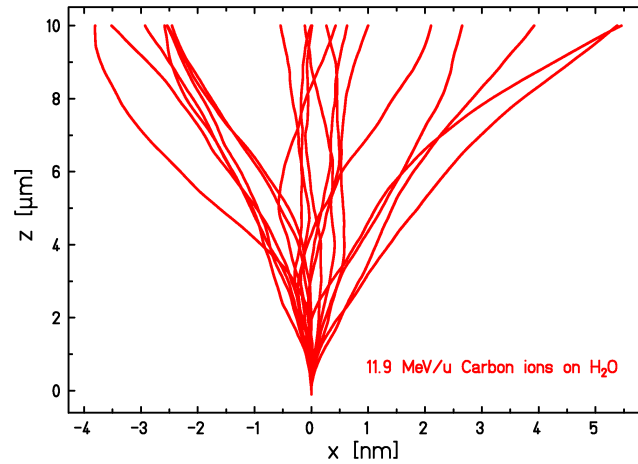


**Figure 6.2:** Tracks of twenty individual carbon ions with 11.9 MeV/u with central incidence on water. The lateral displacement due to elastic scattering is in the order of a few nanometer over a travelling distance of 10  $\mu\text{m}$ . This distance corresponds roughly to the diameter of biological cell nuclei. x and z axes are scaled differently for illustration purposes.

much easier to handle than the Molière distribution.

By simulating the passage of protons through a certain target, the protons are either elastically scattered or undergo an ionization event. So the resulting angular distribution of protons is affected by both the correct description of elastic scattering and ionization. Excitation cross sections for protons incident on solids are not included due to non-availability. Screened Rutherford cross sections for elastic scattering have been observed to be less suitable for low-energy electrons incident on high Z materials than for low Z materials. As a first description these cross section have nevertheless been applied to ions incident on any materials. Comparisons with experimental data should give insights in the applicability of these cross sections for the elastic scattering of ions.

Fitting a Gaussian distribution

$$y = \frac{N}{\sigma \cdot \sqrt{2 \cdot \pi}} \cdot \exp\left(-0.5 \cdot \left(\frac{\pi - \mu}{\sigma}\right)^2\right) \quad (6.4)$$

with  $\mu=0$ , the parameters  $N$  and  $\sigma$  are obtained from simulation results. A nonlinear least square fit relying on the Levenberg-Marquardt algorithm [Marquardt1963] has been used. The value of  $\sigma$  from the fit has been compared with the values for  $\sigma$  from Gottschalk. Comparisons for a range of target materials and thicknesses are shown in table 6.1 and Fig. 6.3. Within the uncertainties, a very good agreement between TRAX results and experimental data is found for all kinds of target materials and thicknesses. Uncertainties for the TRAX calculations are directly provided by the uncertainties of the fit parameter  $\sigma$ . Additionally there has been an uncertainty due to the chosen bin size for the simulation. The agreement is best for low and medium Z target materials. The resulting angular proton distribution from the simulation is affected by both elastic scattering and ionization cross sections for protons. For high Z target materials, proton cross sections for elastic scattering based on screened Rutherford calculations are supposed to be less suitable. However, even for high Z materials like Pb, the agreement between TRAX

results and Gottschalk's experiment is rather good.

Additionally, the results were compared with parametrizations according to the Highland formula [Highland1975] which is a crude parametrization of Molière's theory [Molière1948]:

$$\sigma_{\text{Highland}} [\text{rad}] = 14.1 \text{ MeV} \cdot \frac{\sqrt{\frac{X}{X_0}} \cdot z}{p \cdot c \cdot \beta} \cdot \left[ 1 + \frac{1}{9} \cdot \log_{10} \left( \frac{X}{X_0} \right) \right] \quad (6.5)$$

The radiation length  $X_0$  and the thickness of the target  $X$  are needed and the momentum  $\mathbf{p}$  has to be inserted in units of MeV/c.  $z$  is the charge of the projectile. The momentum in units of MeV/c has been calculated via  $\sqrt{(E_{\text{kin}} + E_0)^2 - E_0^2}$  with energies given in MeV. For 158.6 MeV protons,  $\mathbf{p} = 568.056 \text{ MeV/c}$  and  $\beta = 0.58152$ . The radiation length can be obtained, e.g. from [Gupta2010]. It is usually given in units of  $\text{g/cm}^2$ . The target thickness  $X$  in units of  $\text{g/cm}^2$  can be derived from the target thickness in cm by division through the density of the material. Highland's formula is supposed to have an accuracy of about 17%. [LyDa1991].

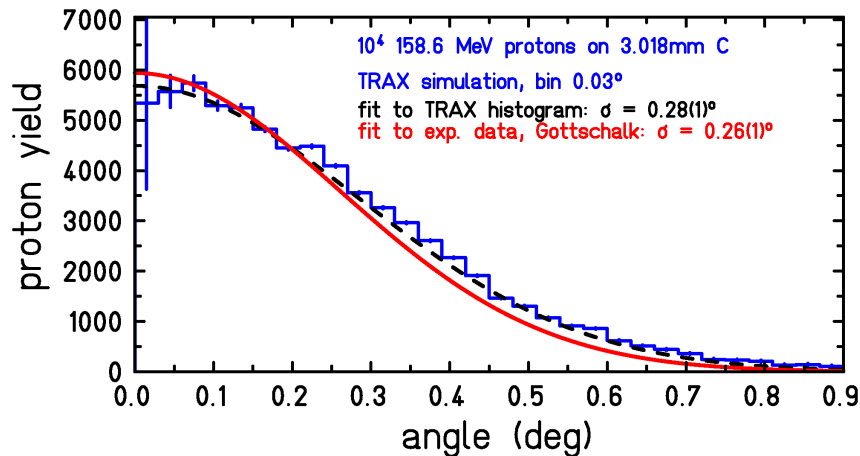


**Figure 6.3:** Angular distribution of protons after passage through carbon target. Shown in blue is the TRAX simulation result as a histogram while the fit result for a Gaussian to the TRAX data is indicated with a dashed black line. The red line indicates a Gaussian with the width determined experimentally by Gottschalk [Gottschalk 1993].

target thickness	TRAX fit	Gottschalk experiment	Highland's formula
Be 0.309 mm	0.05(1) <sup>o</sup> bin size 0.01 <sup>o</sup>	0.06(1) <sup>o</sup>	0.05 <sup>o</sup>
Be 0.602 mm	0.08(1) <sup>o</sup> bin size 0.02 <sup>o</sup>	0.09(1) <sup>o</sup>	0.07 <sup>o</sup>
Be 3.475 mm	0.20(1) <sup>o</sup> bin size 0.03 <sup>o</sup>	0.21(1) <sup>o</sup>	0.19 <sup>o</sup>
Be 6.584 mm	0.30(1) <sup>o</sup> bin size 0.03 <sup>o</sup>	0.30(1) <sup>o</sup>	0.27 <sup>o</sup>
Be 9.822 mm	0.37(1) <sup>o</sup> bin size 0.03 <sup>o</sup>	0.37(1) <sup>o</sup>	0.34 <sup>o</sup>
Be 13.006 mm	0.46(1) <sup>o</sup> bin size 0.03 <sup>o</sup>	0.44(1) <sup>o</sup>	0.40 <sup>o</sup>
Be 25.677 mm	0.73(4) <sup>o</sup> bin size 0.07 <sup>o</sup>	0.68(1) <sup>o</sup>	0.66 <sup>o</sup>
Be 51.117 mm	1.06(4) <sup>o</sup> bin size 0.07 <sup>o</sup>	1.03(2) <sup>o</sup>	0.93 <sup>o</sup>
Be 76.794 mm	1.42(11) <sup>o</sup> bin size 0.07 <sup>o</sup>	1.41(2) <sup>o</sup>	1.14 <sup>o</sup>
C 1.423 mm	0.18(1) <sup>o</sup> bin size 0.03 <sup>o</sup>	0.18(1) <sup>o</sup> , 0.19(1) <sup>o</sup>	0.16 <sup>o</sup>
C 3.018 mm	0.28(1) <sup>o</sup> bin size 0.03 <sup>o</sup>	0.26(1) <sup>o</sup>	0.24 <sup>o</sup>
C 7.279 mm	0.46(1) <sup>o</sup> bin size 0.03 <sup>o</sup>	0.44(1) <sup>o</sup>	0.40 <sup>o</sup>
Al 0.800 mm	0.21(1) <sup>o</sup> bin size 0.015 <sup>o</sup>	0.20(3) <sup>o</sup>	0.18 <sup>o</sup>
Al 3.226 mm	0.45(1) <sup>o</sup> bin size 0.05 <sup>o</sup>	0.44(3) <sup>o</sup>	0.39 <sup>o</sup>
Al 8.048 mm	0.73(1) <sup>o</sup> bin size 0.07 <sup>o</sup>	0.75(1) <sup>o</sup>	0.65 <sup>o</sup>
Cu 0.050 mm	0.13(1) <sup>o</sup> bin size 0.015 <sup>o</sup>	0.13(1) <sup>o</sup>	0.11 <sup>o</sup>
Cu 0.102 mm	0.19(1) <sup>o</sup> bin size 0.02 <sup>o</sup>	0.18(1) <sup>o</sup>	0.16 <sup>o</sup>
Pb 0.026 mm	0.14(1) <sup>o</sup> bin size 0.01 <sup>o</sup>	0.13(1) <sup>o</sup>	0.12 <sup>o</sup>
Pb 0.051 mm	0.23(1) <sup>o</sup> bin size 0.02 <sup>o</sup>	0.19(1) <sup>o</sup>	0.18 <sup>o</sup>
Pb 0.400 mm	0.70(1) <sup>o</sup> bin size 0.07 <sup>o</sup>	0.64(1) <sup>o</sup>	0.57 <sup>o</sup>

**Table 6.1:** Gaussian width  $\sigma$  of angular distribution in degrees for 158.6 MeV protons. TRAX uncertainties result directly from the fit result.

---

## 6.2.2 Effect on radial dose distribution

---

Elastic scattering of ions causes a slight lateral deflection of ion tracks away from the initial direction. The lateral deflection of the ions changes the position of excitation and ionization events and therefore the position of the resulting damage. When analyzing the radial dose distribution, a diffusion of the radial dose can be observed at nanometer distances, shifting dose contributions from  $r=0$  to larger radii. The maximum radius at which an elevated dose contribution due to the lateral ion deflection can be observed is consistent with the maximum lateral deflection. With increasing travelling length, the deflection increases. To evaluate the radial dose distribution with TRAX, an integration inside a cylinder over a given length is performed. Correspondingly, the effect on the radial dose distribution depends on the evaluation length chosen for integration of simulated energy depositions. From comparisons with experimental data, where the radial dose has been evaluated inside ionization chambers, the cylinder length in liquid water can be estimated. According to the experiments for the evaluation of the radial dose of 1 MeV protons in water [WiBa1976], a cylinder of a length of 100 nm is considered to be appropriate. The value has been approximated from the dimensions of the ionization chamber and the conversion factors which are used to scale the radii from gaseous to condensed phase media. In Fig. 6.4 TRAX simulations are compared with and without consideration of the elastic scattering of ions for an integration length of  $\Delta Z=100$  nm. Some energy depositions are shifted from the core to radii of up to around 0.2 nm which increases the radial dose in the corresponding bins. The lateral deflection of 1 MeV protons over a travelling length of 100 nm seems to be negligible on a macroscopic scale, but on the nanometer scale, the radial dose distribution is affected. Fig. 6.5 shows changes on the radial dose profile of 1 MeV protons in water for integration lengths of 50 nm, 100 nm and 200 nm.

There is no clear rule from which an appropriate integration length could be determined. In

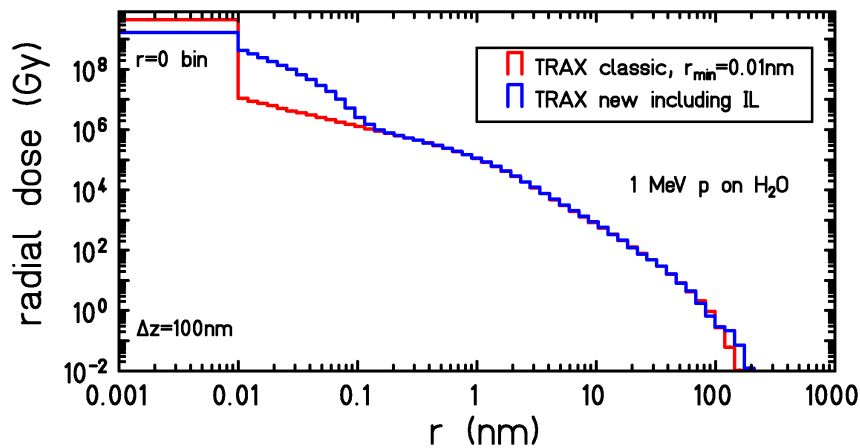


**Figure 6.4:** For 1 MeV protons incident on H<sub>2</sub>O, a radial dose has been calculated with TRAX classic (shown in red, neglecting the elastic scattering of ions) and the recent TRAX version (shown in blue). The dose at the  $r=0$  bin decreases slightly if elastic scattering is considered. Deviations show up below 0.2 nm. The evaluation has been performed inside a cylinder with height  $z=100$  nm.

experiments, the size of an ionization chamber or gas counter is known and the needed evalu-

---

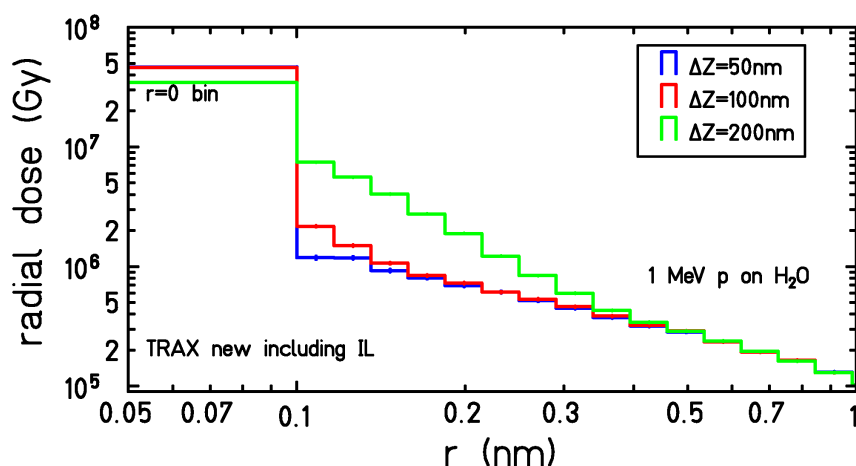


**Figure 6.5:** For 1 MeV protons incident on H<sub>2</sub>O, a radial dose has been calculated with TRAX including the elastic scattering of ions.  $r_{min}$  has been chosen to be 0.1 nm in each simulation. Different integration lengths have been chosen to determine the radial dose. The evaluation has been performed in cylinders with height 50 nm, 100 nm or 200 nm, differences exist at radii below 0.4 nm. If a larger cylinder height would be chosen, the smear out of the radial dose would be visible at larger radii.

ation length to compare with simulation results can be derived from density scaling. However, the ion beam does not necessarily enter the ionization chamber with zero angular spread. Usually, it has already a lateral deflection which has to be considered. The simulation geometry or the evaluation length to analyze the radial dose distribution would have to be chosen larger, enhancing the diffusion effect.

To theoretically estimate an appropriate cylinder length, two factors are important. The incident projectile should not lose a significant amount of its initial energy and the buildup of secondary electrons should be complete. The last factor is especially important to obtain reasonable results from MC simulations. Higher statistics can reduce the length needed for an appropriate radial dose evaluation. An ion projectile with a kinetic energy of 1 MeV/u can produce electrons with kinetic energies up to around 2 keV. Statistics and the cylinder length have to be chosen to assure the consideration of electrons up to 2 keV. The range of these electrons directly corresponds to the maximum radius at which a contribution to radial dose distribution is present. Including the elastic scattering of ions, secondary electrons are created at slightly different positions which can slightly increase the maximum radius at which contributions to the radial dose are present. Another possibility to choose the evaluation length is to choose standard values. These can be considered to be equal to typical volumes in which the evaluation the radial dose is important. Typical targets of biological interest are the distance between two strands of the DNA which is about 2 nm, a cell nucleus with a size of  $\approx 1 \mu\text{m}$  and a cell which has a size of about  $10 \mu\text{m}$ . In the case of 11.9 MeV/u carbon ions on water, a typical energy present in particle therapy, the size to obtain an energy loss of about 1% is  $5.31 \mu\text{m}$  which is comparable to the order of the cell nucleus diameter.

Even though the effect of the elastic ion scattering on the radial dose distribution is noticeable only at (sub) nanometer radii, it is supposed to have an impact on biological damage for critical target sizes are on the nanometer scale. The effect is considered to be important also for de-

tector simulations. TLD efficiencies [Horowitz2001] critically depend on correct values for the radial dose values on the nanometer scale. A full simulation considering the lateral spread of ions along their path through a TLD might be necessary to evaluate the appropriate radial dose distribution.

### 6.3 Discrete interaction distances

In MC simulations, distances between interactions are usually chosen randomly inside a medium considered as uniform. The actual interaction length is determined by the mean free path, which has been derived from the interaction cross sections, and by a random number. Any interaction point is possible, no matter whether a target atom is actually located at that point or not. This approach is appropriate for gaseous targets where atoms move very fast and on a macroscopic scale their exact current position is unimportant. In solid or liquid targets, densities are high in contrast to gaseous targets and therefore atoms or molecules are placed closer to each other. Besides, the motion of atoms or molecules is slowed down compared to a gaseous state, so as an approximation one could consider that they do not move on a short timescale. As a very simple model assumption one could consider a cubic grid where the atoms or molecules are located with constant average interatomic or intermolecular distances. With the density of a material it is possible to calculate the average distance between atoms/molecules. Considering water with a density of  $\rho = 1 \text{ g/cm}^3$ , and a molar mass of 18 g, the number of molecules per cubic centimeter can be estimated:

$$\frac{\#\text{molecules}}{\text{cm}^3} = \frac{N_{\text{Avogadro}} \cdot \rho}{M_{\text{mol}}} = \frac{6.023 \cdot 10^{23}}{18} \approx 3.35 \cdot 10^{22} \quad (6.6)$$

From this one can estimate the average molecular distance  $\mathbf{d}$ , assuming a distribution of molecules on a cubic grid:

$$\mathbf{d} = \left( \frac{\#\text{molecules}}{\text{cm}^3} \right)^{-1/3} = 3.1 \cdot 10^{-8} \text{ cm} = 0.31 \text{ nm} \quad (6.7)$$

The same estimation performed for amorphous carbon with a molar mass of 12 g and a density of  $2.267 \text{ g/cm}^3$  results in an average inter-atomic distance of 0.27 nm. Graphite has a different atomic arrangement, with atoms arranged in hexagons forming layers in which the inter-atomic distance is about 0.14 nm and a distance between two layers of around 0.34 nm. So for our simulation purposes the minimum distance between carbon atoms is considered to be about 0.14 nm.

To consider the differences between solid and gaseous targets, TRAX has been extended to account for the possibility of having discrete interaction distances. As usual, a mean free path is derived and the actual interaction distance is sampled using a random number. As an approximation, atoms are considered to be arranged at a cubic grid. Therefore, the x- y- and z-coordinates of the sampled interaction point are compared with multiples of the inter-atomic or inter-molecular distances. Considering water as a target material, the sampled interaction point is changed to the nearest located point which coordinates are a multiple of 0.31 nm. The shift is performed individually for all three coordinates. Therefore, interaction points are shifted to the center position of the nearest located molecule. With this modification, radial dose distributions have been calculated for 1 MeV protons in water. Results show a non-continuous profile

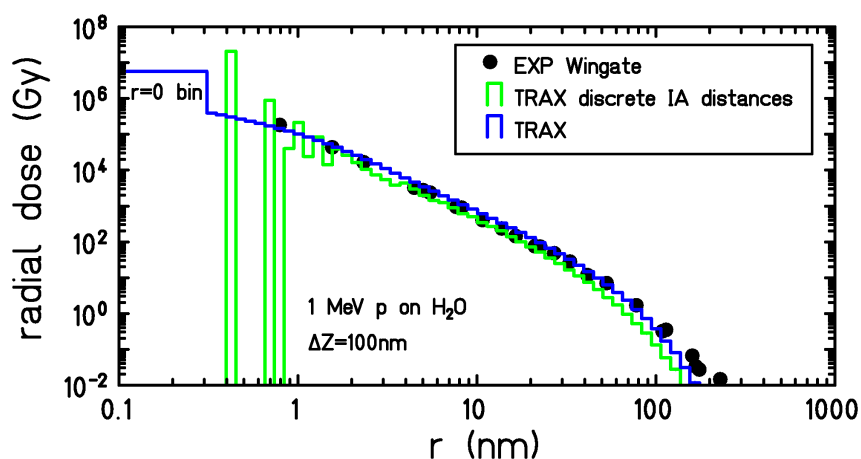


**Figure 6.6:** TRAX results for the evaluation of the radial dose for 1 MeV protons in H<sub>2</sub>O in a cylindrical volume with a height of 100 nm. The blue histogram show standard TRAX calculations while the green histogram shows results including the consideration of discrete interaction distances. As only multiples of 0.31 nm are allowed for x and y coordinates, the radius which is calculated via  $r = \sqrt{x^2 + y^2}$  can have only values resulting from the discrete x and y values. The minimum radius at which a dose contribution can be found is therefore 0.31 nm, at (0.31 nm, 0 nm) or (0 nm, 0.31 nm).

with dose values appearing at the multiples of the assumed molecular distances (see Fig. 6.6). Therefore, the choice of a minimum radius for  $D(r)$  smaller than the inter-molecular distance is considered to be inappropriate. Although the approach is largely simplified for liquids as usually molecules are not strictly arranged in a cubic grid and still have a certain possible range of movement. For solids the approach is considered to be reasonable. The considerations show that there must be a lower limit for a reasonable choice of the minimum radius since an energy deposition at distances smaller than the atomic radius is not possible. However, several models relying on radial dose profiles as input parameters, like the biophysical LEM [SchKr2004] assume a continuous dose profile starting at  $r_{min} = 0.1$  nm. As the radial dose distribution in LEM is considered to describe the average energy deposition per unit mass, a conceptual problem arises. A distribution of local energy depositions might describe the situation in solids closer to reality than the definition of a radial dose distribution. This concept is not compatible with LEM. The approach of discrete interaction distances could be investigated further in a full simulation describing damage in biological targets or detector materials.

## 6.4 Gaussian diffusion of radicals

Ionization and excitation can lead to the production of radicals. It is known that in water a variety of radicals is produced, like OH, H, HO<sub>2</sub>, H<sub>2</sub>O<sub>2</sub>, OH<sup>-</sup> and others [Nikjoo2006]. These radicals can travel inside the target material and interact with other radicals or target atoms. Radicals can recombine or create further radicals and will diffuse the resulting damage around their point of creation. Through radical diffusion, energy can be deposited apart from the initial interaction point for the ionization or excitation which produced the radical. The description of radical transport is more complicated than for secondary electrons. Therefore, one could con-



sider the effect of radical diffusion by a random diffusion of damage around the initial inelastic interaction point. A TRAX version has been created which considers the effect by distributing the damage by ionization or excitation events randomly inside a Gaussian distribution with a width  $\sigma$  of 4 nm. This width has been chosen according to a similar approach which has been considered in an extension of LEM III [Elsässer2008] where the complete radial dose distribution has been folded with a Gaussian profile assuming a constant  $\sigma$  of 4 nm. In the evaluation of the radial dose distribution with TRAX, the coordinates of the damage deposition are modified. As for the evaluation of the radial dose, an integration over  $z$  is performed and only  $x$  and  $y$  coordinates are needed to determine the radius  $r$  by  $\sqrt{x^2 + y^2}$ ,  $x$  and  $y$  have been altered. Two random numbers  $g_1$  and  $g_2$  are created with values between 0 and 1, while the probability of their values is weighted according to a normalized Gaussian profile, with a value of 1 at the maximum and a width  $\sigma$  of 1. The random numbers have been obtained by a Box-Muller transformation. The new shifted  $x$ - and  $y$ -coordinates are calculated via  $x = x + \sigma \cdot g_1$  and  $y = y + \sigma \cdot g_2$  with  $\sigma=4$  nm. The approach using TRAX and shifting the damage deposition coordinates allows more variability as it can be distinguished between excitation, ionization and cut-off events and the possibility to change diffusion width for a certain type of inelastic interaction is given. Besides, excitation and ionizations do not only take place at the center of the track, they can also be induced by secondary electrons farther away. The method of considering the diffusion in the simulation code, allows to diffuse also these dose contributions. A TRAX simulation for the radial dose distribution resulting from 1 MeV protons in water, shows a substantial dilution of the core dose and is compared with TRAX classic results in Fig. 6.7. The version considering the diffusion of radicals shows an approximately constant dose around the center of the track and an almost identical profile at larger radii. Minor differences are visible which are caused by the diffusion of dose created by secondary electrons.

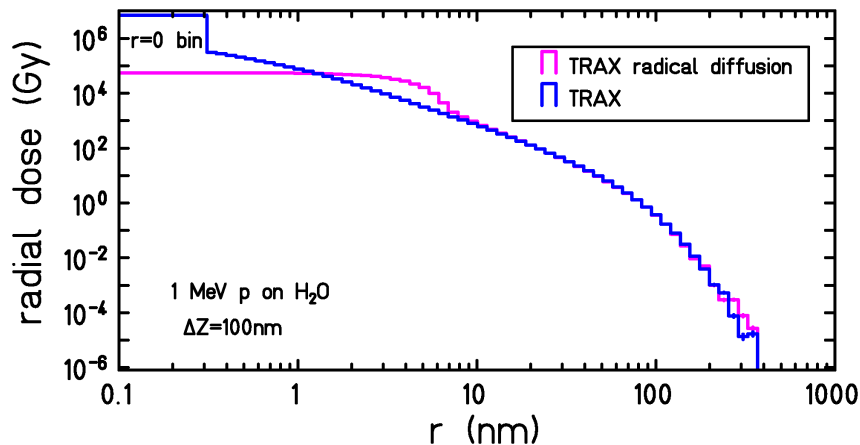


**Figure 6.7:** Radial dose for 1 MeV protons incident on  $H_2O$  evaluated with TRAX in a cylindrical volume with height 100nm. Compared are standard TRAX results (blue histogram) for  $r_{min}=0.31$  nm with those including the radical diffusion in the evaluation (pink).

---

## 6.5 Cut-off energy dependence

---

The cut-off energy for electrons determines the energy below which the tracks of electrons are no longer followed. It is reasonable to assume a certain cut-off value, as electrons below a certain energy have ranges that can be less than a nanometer. For energies below 10 eV, the most probable interaction is elastic scattering. Further following of electrons would lead to a high number of events which increases calculation time without contributing to energy degradation. However, for some applications, details on the (sub)nanometer scale might be relevant. To follow the ends of the electron tracks, a reduced cut-off value can be reasonable, if the description of inelastic interactions is still possible. The lower limit is the lowest possible energy transfer present in one of the inelastic interactions and the lowest projectile energy for which the cross section for the interaction is known. A standard value for the cut-off which has been chosen in TRAX classic is the ionization threshold. In the case of H<sub>2</sub>O this has been 11.5 eV. Excitation cross sections for electrons in water are available for 8 channels down to 7.4 eV while sub-excitation cross sections can be obtained down to 1.7 eV. As the extended TRAX uses these excitation cross sections, evaluations of the radial dose distribution are possible using lower cut-off energies.

The radial dose distribution evaluated by TRAX, contains contribution from cut-off events.

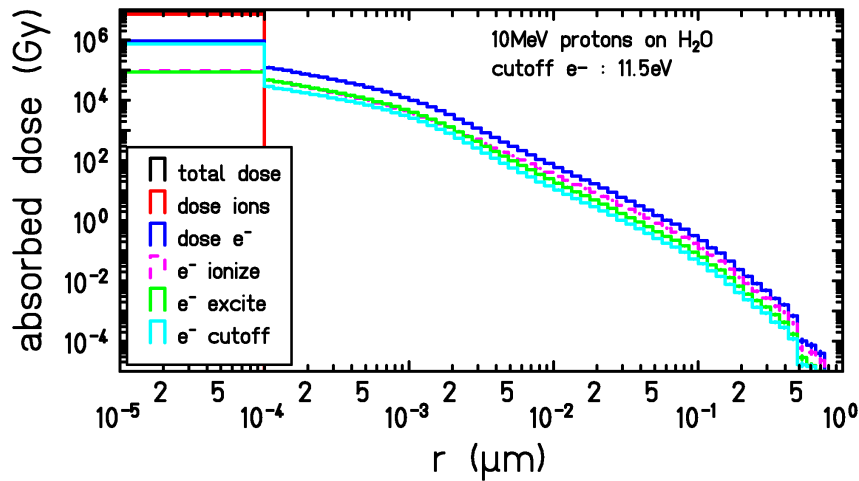


**Figure 6.8:** TRAX calculations for the radial dose from 10 MeV protons in water. The total dose in the lowest bin is dominated by ion contributions. For larger radii, secondary electrons create the dose contributions.

To illustrate the impact of a certain cut-off energy, contributions from different energy deposition events have been distinguished. A differentiation from dose contributions between ions and electrons has also been implemented. Fig. 6.8 shows the contributions for the radial dose distribution for 10 MeV/u protons in water. The majority of the contribution in the lowest bin is induced by the primary projectiles. At larger radii, all contributions stem from electron interactions. For this simulation, the elastic scattering of ions has been neglected, therefore no contributions from ions are present at larger radii. At smaller radii, the maximum contribution to the electron dose stems from cut-off events. The plot shows results for the standard cut-off value of 11.5 eV which is used by TRAX classic. The dose in the zero radius bin which goes from  $r=0$  to the minimum radius shows a much higher value than the first bin starting from

---

$r_{min}=0.1$  nm. Apart from the ion contributions to the dose, also from electron contributions a step is visible. The step is considered to be caused by the rather high cut-off energy. Many produced electrons at radii below 0.1 nm, which is the chosen  $r_{min}$  value, have energies below 11.5 eV, as the electron dose contribution is dominated by cut-off events.

As improved cross sections for electron excitation of water are available, the simulation has been repeated with the reduced cut-off energy which can be seen in Fig. 6.9. The step between electron contributions to the total dose inside the lowest bin to the following bins almost completely vanishes. Cut-off contributions no longer dominate the dose contributions from electrons. There is a bump in the radial dose profile at around 20 nm for contributions from cut-off events. At the same radius, there is a shift in the order of relevance of ionization and excitation contributions. Probably, at this point most ionizations created by secondary electrons are caused by electron with an energy already high enough to induce an ionization but without much energy left that could be transferred to the tertiary electron in form of kinetic energy. Therefore, all tertiary electrons are directly absorbed by cut-off events. At increasing radii, secondary electrons have higher energies and can create tertiary electrons with kinetic energies high enough to be not directly stopped.

Other MC track structure simulations like PENELOPE [Salvat2003] often have cut-off energies

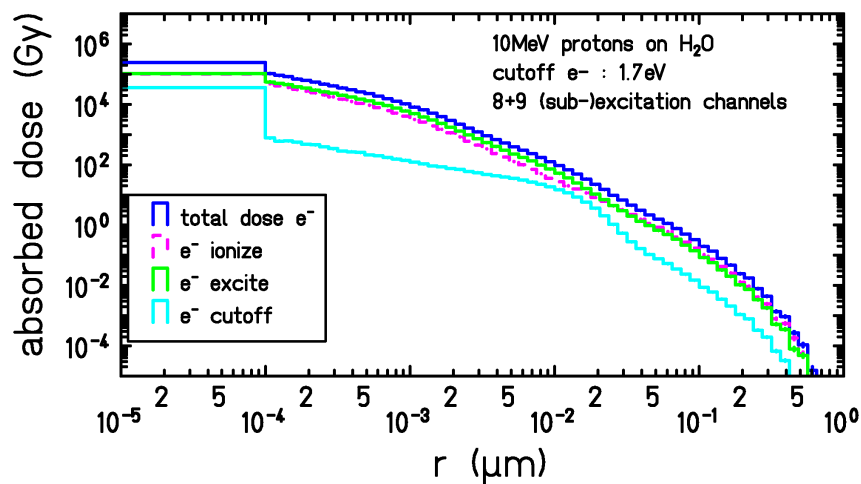


**Figure 6.9:** TRAX radial dose contributions from secondary electrons created by 10 MeV protons in water. Reducing the cut-off energy to 1.7 eV allows a more realistic description. Both ionization and excitation contribute significantly to the total dose. There is almost no step between the zero radius bin and the following bins.

as high as 50 eV or even 100 eV. Most TLD efficiency calculations are based on simulations using a cut-off energy as high as 50 eV [Avila1999, Horowitz2001]. To illustrate the resulting effect of a high cut-off energy of 100 eV on the radial dose distribution, the total dose contribution from secondary electrons, created by 10 MeV protons incident on water, is shown in Fig. 6.10. A very large step in the dose profile is visible at the lowest bin.

To illustrate the resulting differences in the radial dose distribution, total electron dose contributions have been compared for cut-off values of 100 eV, 50 eV, 11.5 eV, 7.4 eV and 1.7 eV. The energy of 7.4 eV corresponds to the lowest possible energy loss for an electronic excitation while 1.7 eV is the lowest energy for which electron cross sections are available for sub-excitations. Reducing the cut-off energy to energies below the ionization threshold, enhances the amount of

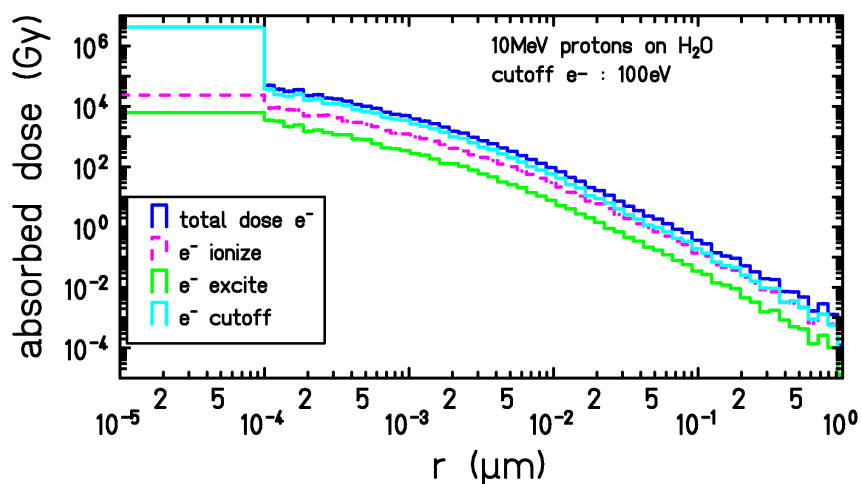


**Figure 6.10:** TRAX radial dose contributions from secondary electrons created by 10 MeV protons in water. The dose is almost completely stemming from cut-off events as most produced electrons have energies below 100 eV, which is the chosen cut-off energy.

excitation and elastic scattering events and the dose contribution from excitation while reducing the dose contribution from cut-off.

This differentiation of contributions to the radial dose calculation shows the importance of the use of a cut-off energy as low as possible for radial dose calculations on the (sub) nanometer scale.

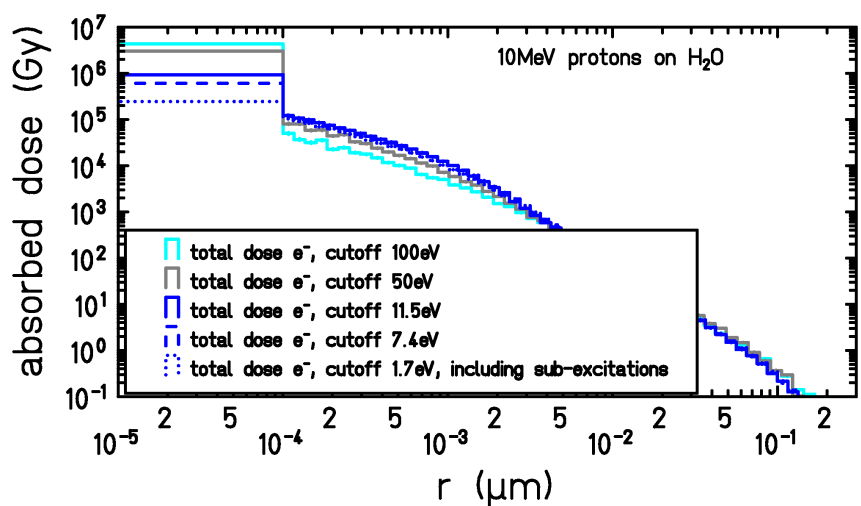


**Figure 6.11:** Dose contributions from secondary electrons, created by 10 MeV protons in water. For a larger cut-off energy, a huge step is visible between the dose in the zero radius bin and the following bins. For illustration purposes, the radial dose distribution is only shown down to a value of 0.1 Gy. Choosing a high cut-off energy does not only result in a large step at  $r_{min}=0.1$  nm but also influences the radial dose at small radii above  $r_{min}$ .

---

## 6.6 Impact on RBE

---

In [Elsässer2008] it has been shown that calculations for the RBE with LEM are significantly affected by a change of the radial dose profile in the ion track center at radii below a few nanometers.

Usually, LEM uses simplified radial dose profiles based on amorphous track structure calculations to determine the radiobiological effectiveness of ion irradiation. These amorphous track structure radial dose profiles have a constant dose core, while the radial size of this core is depending on the energy of the projectiles.  $r_{min}$  is chosen as  $\beta_{ion} \cdot r_c$  with  $\beta_{ion} = v/c$ ,  $v$  being the velocity of the particle and  $c$  the speed of light.  $r_c$  is considered to be the largest extension for the inner part of the track at  $v = c$  [Elsässer2008]. The value is chosen according to a fit to experimental data for a given cell type. Above this core, the dose falls off with  $1/r^2$  until a maximal radius is reached. The maximal radius is a parametrized value. A justification of the choice of a constant dose core is given by geometrical considerations. The DNA in the cell nucleus is supposed to be the critical target for cell inactivation [Elsässer2008]. It is considered that differences in the radial dose at distances smaller than the target area cannot be assigned. Deviations from this simple amorphous track structure model and TRAX results for the radial dose distribution can be seen for 11.9 MeV/u carbon ions incident on water in Fig. 6.12. Results from amorphous track structure differ from TRAX results for the radial dose at small radii up to a few nanometers. Furthermore, the maximum radius at which dose contributions are present is significantly different. It should be noted that calculations based on amorphous track structure do not account for the energy depositions directly caused by the primary ions in the core (which is about 1/3 of the total dose). This contribution is simply added to the radial dose distribution in order to correctly reproduce known LET values by integration of  $D(r)$  over  $r$ .

It has been planned to improve the radial dose profile which is used as an input in LEM by a physically more realistic external radial dose profiles which have been calculated with TRAX. As input, radial dose distributions with a minimum radius of 0.1 nm for the innermost radial bin are needed, using a semi-logarithmic scaling for the radial bins. The calculation of the RBE is very sensitive on changes of the radial dose profile at radii below a few nanometers. Therefore the goal should be to be as accurate as possible in the innermost part of the track. TRAX radial dose profiles from the classic version have already been used as input for LEM [Elsässer2008]. Using radial dose profiles without considering radical diffusion, unrealistic parameters had to be chosen in order to use these radial dose profiles in combination with LEM to obtain reasonable RBE values. In TRAX classic calculations the dose value for the zero-radius bin has been much higher than the value for the next radial bins, which can be seen in Fig. 6.12. Including the diffusion of radicals externally by folding the radial dose distribution with a Gaussian profile affected the resulting RBE values significantly. For a similar analysis using the new approach for radical diffusion handled directly in the simulation leads to a difference up to a factor of 2 in the resulting RBE values around  $LET = 70 \text{ keV}/\mu\text{m}$ .

Unfortunately, conceptual problems arise between LEM and track structure MC codes. LEM is based on the average dose induced by an incident ion. Reducing the value of  $r_{min}$  to a value on the nanometer scale can lead to a conflict in the approach of an average value. As the dose is defined as energy/(volume · density), the dose increases with decreasing volume. Considering very small volumes can result in single molecules located in the volume of interest. Defining an average dose for a single molecule is not a reasonable concept.

---

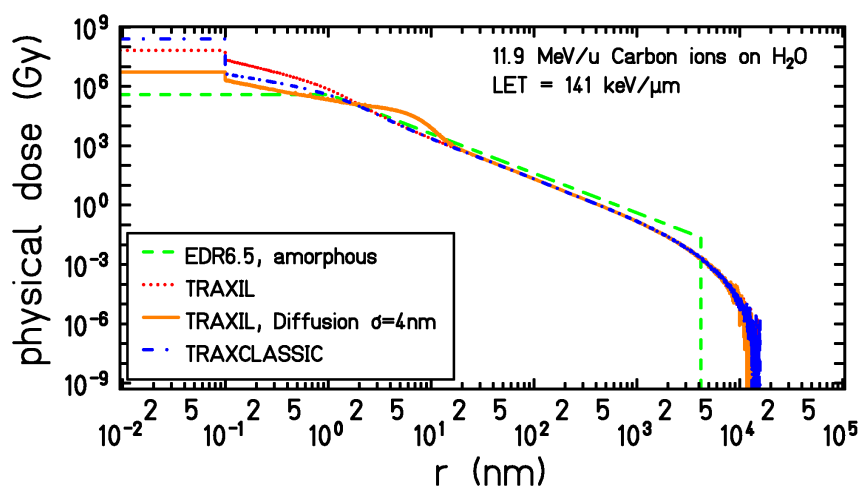


**Figure 6.12:** Radial dose profiles using different model assumptions: The current version of LEM uses a simple amorphous track structure model, "optimized" to reproduce experimental RBE results (labeled EDR6.5). TRAXIL is the TRAX version including the elastic scattering of ions. Another TRAX version includes the diffusion of radicals by folding the energy deposition events with a Gaussian profile with  $\sigma=4$  nm. For all TRAX simulations,  $r_{min}$  has been set to 0.1 nm which results in the non-physical step. The step is also visible in the version considering radical diffusion, as the diffusion has not been considered for energy depositions due to cut-off.

As the implementation of the multiple scattering of the primary ions has an impact on the difference between the dose in the zero-radius bin and the next bins, it has been hoped to evaluate the effects using these radial dose profiles with LEM. Unfortunately, radial dose profiles accounting for this effect cannot be translated to the LEM because they are not compatible with the assumptions on which the LEM is based. LEM assumes the radial dose profile to be defined relative to the actual scattered ion path, rather than along the original direction of incidence when entering the sensitive volume. In LEM, the origin of the radial dose profile is always matching the actual center of the ion track, and is not defined around the initial direction. As LEM considers the average radial dose distribution created by a single ion traversal, the effect of multiple scattering cannot be taken into account. In TRAX, the average of a single ion is evaluated by the calculation of multiple ion tracks which are then normalized to the number of incident ions. However, in reality, the theoretical definition considered in LEM is not justified. Applying ions beams for irradiation, a target of consideration will always be affected by the traversal of multiple ions. The effect of ion irradiation and following ion and electron interactions has a stochastic nature which is reproduced in MC simulations. The scenario which is simulated by TRAX resembles the situation which is usually found in microdosimetry experiments. Ions traversing an ionization chamber will scatter elastically which will lead to a nanoscopic lateral broadening of the beam. The radial dose can only be evaluated around the original center of the ion track as a change of the center of a single track cannot be followed experimentally. Theoretically one can define the radial dose center along the axis of a cylinder around the actual ion path. But in measurements or actual applications where the radial dose distribution is used to describe damage in biological systems or inside a detector (TLD), it will not be possible to define this actual axis and the scenario which TRAX simulates will be appropriate.

---

A solution to consider physical effects like the multiple scattering of ions in a biophysical model would be to modify the whole concept. It would be necessary to directly include the sampling of single interactions like it is done in the MC simulations. To account for single inelastic events in a biophysical model rather than using an average radial dose distribution would be more realistic.

---





---

## 7 Simulations on metallic nanoparticles

Metallic nanoparticles (NPs) have been considered as possible "dose enhancers" in combination with radiotherapy. In combination with photon irradiation, a local dose enhancement is proven and can be assigned to the creation of a high amount of secondary electrons by Auger electron cascades. Ion irradiation causes the creation of a large amount of secondary electrons, even without the vicinity of a metallic NP. It has to be evaluated whether metallic NPs irradiated by ions lead to an excess secondary electron creation, which could be caused by Auger electron cascades. To elucidate whether metallic NPs can lead to a dose enhancement in combination with ion irradiation, the radial dose distribution around the NP has to be determined. Then it has to be compared with the radial dose distribution without the presence of a metallic NP. Before evaluating microscopic damage, the radiation transport has to be followed. It is interesting to observe the secondary electrons which are created inside the NP. Secondary electrons can be produced either directly by ionization processes or indirectly after an ionization event in the form of Auger electrons. Both processes are qualitatively different as direct secondary electrons have a continuous energy distribution while Auger electrons are emitted with discrete energies. Auger electrons are seen as a promising source of additional electrons as their yields can be large in the case of high  $Z$  ( $Z$  = atomic number) materials. In high  $Z$  materials like gold, a huge amount of electrons are located in various electron shells. Therefore it is conceivable, that not only one Auger electron is emitted in the relaxation process after an ionization event, but rather a cascade. But dense, high  $Z$  materials can not only produce a large number of secondary electrons. The same properties also lead to a high stopping power and therefore a short range of electrons inside the material. Therefore, it is important to evaluate which secondary electrons actually escape the NP so that they can deposit energy outside the NP in the surrounding tissue. The extended TRAX code allows the calculation of electron creation and transport in several metallic target materials. The detailed calculation allows to observe which process dominates. Besides, the detailed production of Auger electron cascades can be simulated. As Auger electrons are supposed to play an important role in this process, focus has been given on the evaluation of the emission of Auger electrons and cascades inside metallic NPs. Description of resulting damage of ions and electrons inside water (as a tissue equivalent material) is possible using the radial dose distribution. This allows to perform simulations for metallic nanoparticles and to estimate their impact when used in radiotherapy. A publication about TRAX calculations concerning the effect of metallic nanoparticles in combination with ion beam irradiation is in preparation [Waelzlein2013b].

In the following TRAX simulations, a monoenergetic proton source with 80 MeV has been used. The NPs used in the simulations have a radius of either 2 nm or 22 nm and have been surrounded by a hollow water sphere. These values have been chosen according to experimental data [Polf2011] and the energy is a typical value inside the spread out Bragg peak. The nanoparticle sizes are supposed to result in a high cellular uptake. The water sphere has an inner radius of 2.1 nm or 22.1 nm respectively and an outer radius of  $1\ \mu\text{m}$ . The outer radius corresponds roughly to the diameter of a biological cell nuclei. The proton source has been spatially distributed across a thin disk with the same diameter as the NP. To evaluate the pure effect of

---

proton irradiation on the NP, the source has been placed in a vacuum of 0.1 nm thickness between the inner NP sphere and the outer water sphere. Proton projectiles hit the NPs in straight forward direction while covering the whole surface of the NP. Fig. 7.1 shows a sketch of the geometry used for the simulations.

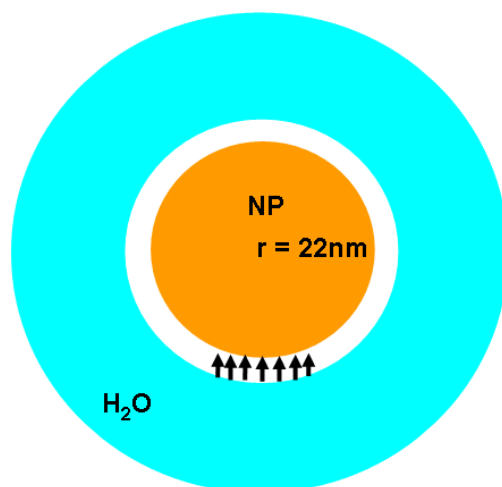


**Figure 7.1:** Sketch of the geometry used for TRAX simulations.

---

## 7.1 Auger electron energy distributions

---

Auger electron production in several high Z metallic materials is evaluated for NPs consisting of Au, Pt and Gd. Fig. 7.2 shows histograms as a function of energy for produced Auger electrons in  $r=22$  nm NPs after incidence of 80 MeV protons. Auger electrons are recorded with their initial energies (before suffering inelastic collisions) at the point of creation, neglecting possible energy losses during their transport through the NPs. The overall yield is much higher for Au and Pt than for a Gd NP. The integrated energy of Auger electrons created per projectile further fortifies this observation. Gd Auger electrons have an integrated energy of 11 eV which is much lower than the integrated energy for Au (52 eV) and Pt (76 eV).

Analyzing the amount of created Auger electrons per projectile for the different NP materials, shows that for Pt and Au the number of ionizations is enhanced compared with Gd, and the enhancement in Auger electron yields is even larger. Table 7.1 compares for Au, Pt and Gd NPs with  $r=22$  nm and proton projectiles with 80 MeV, the number of ionizations, total cumulated number of produced Auger electrons (including cascades), number of single Auger electrons and number of produced photons per incident projectile. The number of produced X-rays per projectile is extremely small which shows their insignificance. X-rays can be produced in competition to Auger electrons after an ionization event. The current TRAX version does not follow the transport of photons, which is justified for these simulations as the X-ray contribution is less than 0.1% in this simulation, even for high Z materials. Pt shows the highest ionization and Auger electron yield in this comparison. Due to the presence of Auger electrons, the number of secondary electrons is enhanced by a factor of about 10% in the case of Pt, but only about 2% in the case of Gd. Comparisons for the Auger electron yields as a function of cascade size are presented in Fig. 7.3.

---

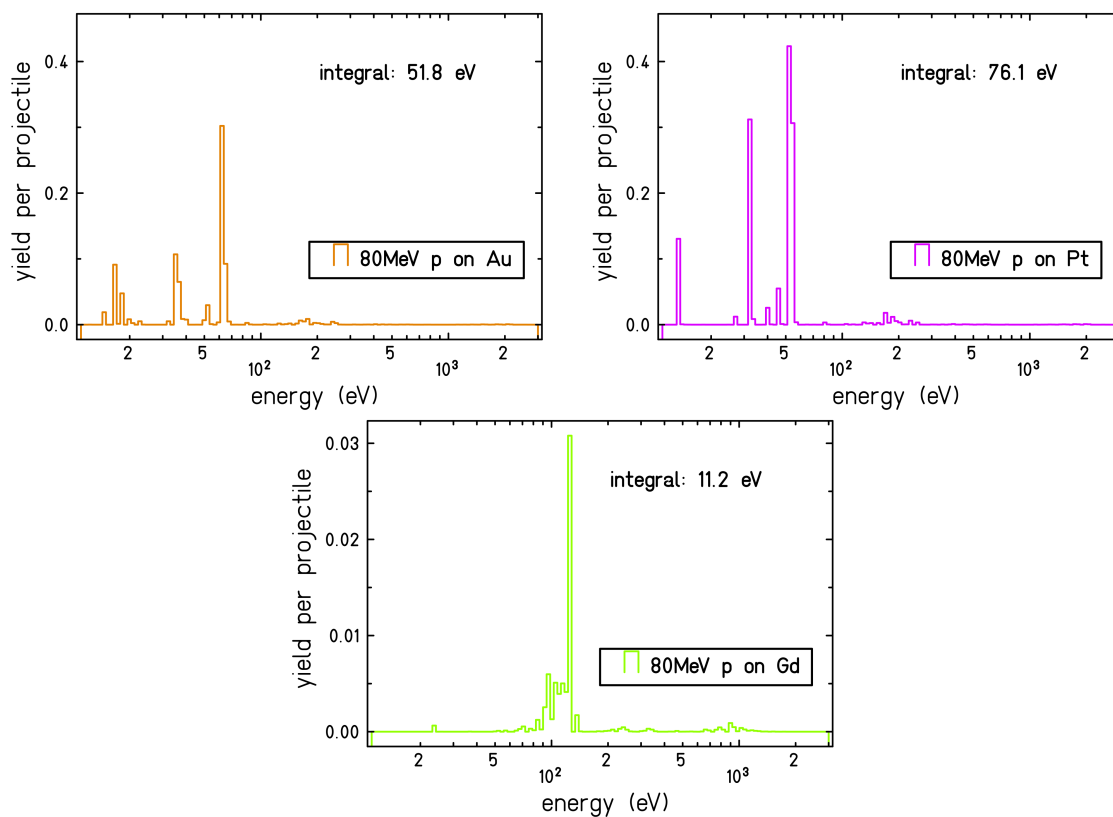


**Figure 7.2:** Initial energy spectra of Auger electrons created in various materials after incidence of 80 MeV protons on a  $r = 22$  nm NP. Considered are Auger electrons created anywhere in the full NP with their initial energies. Upper left: Au. Upper right: Pt. Bottom: Gd, which shows yields lower by an order of magnitude. Integrated energies for all produced Auger electrons with initial energies up to 3 keV are shown per projectile.

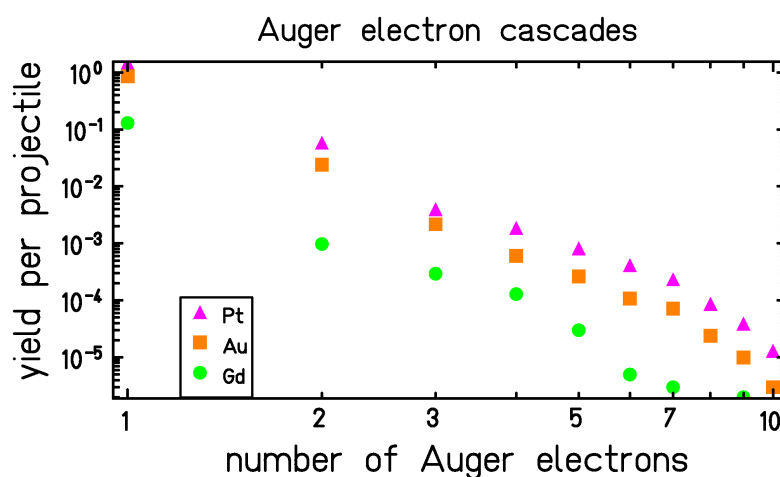


**Figure 7.3:** Yield of Auger electrons created in various materials after incidence of 80 MeV protons on a  $r = 22$  nm NP. The yields are shown for single Auger electrons and cascades as a function of the size of the cascade.

material	ionizations	primary Auger e <sup>-</sup>	all Auger e <sup>-</sup>	photons
Au	10.0	0.85	0.91	0.001
Pt	16.5	1.46	1.61	0.0002
Gd	7.7	0.13	0.13	0.00008

**Table 7.1:** Number of ionizations, number of primary Auger electrons and produced Auger electrons including cascades per incident 80 MeV p projectile on a r=22 nm NP. Auger electrons created by secondary electrons are included. For Gd, almost only primary Auger electrons are created.

## 7.2 Secondary electron spectra outside the NP

For a possible local dose enhancement in the tissue surrounding the NPs, secondary electrons created inside the NPs have to escape. Evaluations of the energy spectra of secondary electrons escaping the NP have been made after having suffered transport collisions inside the NP. The spectra are compared with and without the consideration of Auger electron production. Additionally, electron spectra have been evaluated by replacing the metallic NP with water or water with the same density as the metallic material. This is designed to show differences through an enhancement in electron yields in the presence of a metallic NP in tissue. Water is used as a tissue equivalent material. The comparison with the artificial "dense water" is used as a reference to distinguish between pure density effects and real differences arising from the specific properties of the metallic material. Fig. 7.4 shows secondary electron spectra for Pt, Au and Gd where significant differences can be observed.

The spectra of Au and Pt show similar Auger electron distributions. Several transitions are visible at energies below 100 eV and a few additional Auger electrons at around 200 eV and around 2 keV. The spectra for Gd show dominant Auger transitions around 150 eV and slightly below 1 keV which can be identified by two prominent edges. From the edge at 150 eV, a long tail towards lower energies can be observed which is caused by Auger electrons created anywhere in the Gd NP. Depending on their creation point, they lose different amounts of energy during their transport to the surface of the NP. As Gd has high excitations cross sections for low energy electrons, these electrons are easily absorbed. Therefore, in the region below 20 eV, Gd shows no enhancement for the electron yield compared to water. For Pt and Au, clear enhancements are visible compared to water in the same energy region.

## 7.3 Radial dose distributions

The resulting excess dose distribution from electrons escaping the NP can be evaluated in surrounding water using radial dose distributions. Rather than analyzing the radial dose inside a cylinder along the ion track, the radial dose has been analyzed in spherical shells around the center of the NP. This kind of dose distribution allows to study local dose enhancements close to the NPs as a function of distance from the NP. In analogy to the secondary electron spectra, NPs which have been placed inside the surrounding water, have been replaced a sphere of water ( $\rho = 1 \text{ g/cm}^3$ ) and by a sphere consisting of dense water ( $\rho = \rho_{Fe} = 7.874 \text{ g/cm}^3$ ,  $\rho_{Ag} = 10.49 \text{ g/cm}^3$ ,  $\rho_{Gd} = 7.901 \text{ g/cm}^3$ ,  $\rho_{Pt} = 21.09 \text{ g/cm}^3$  or  $\rho_{Au} = 19.3 \text{ g/cm}^3$  respectively) for comparisons. The simulations are again performed for NPs with r=22 nm and protons with

---

80 MeV. Additionally, 2 MeV and 300 MeV have been chosen as projectile energies to cover the whole energy range which can be present along the penetration depth of protons used for radiotherapy. The higher energy corresponds to the entrance energy of protons for deep seated tumours while the lower energy corresponds to the Bragg peak region, close to the final stopping of proton projectiles. Fig. 7.5 shows radial dose distributions outside various metallic NPs in comparison with water and dense water. Pt and Au appear to be the most efficient materials in terms of dose enhancement, followed by Ag and Gd. In the vicinity of these NPs, an obvious dose enhancement is visible up to radial distances of around 50 nm from the center of the NP. These 50 nm correspond to a radial range of around 18 nm outside the NP as the dose evaluation has been performed outside the NP starting at  $r=22.1$  nm. The results for 2 MeV and 300 MeV protons are qualitatively the same as for 80 MeV protons, showing an overall enhancement of local dose for metallic NPs, where Au and Pt lead to the highest enhancement compared with water or dense water. Quantitatively, the overall dose has been enhanced for 2 MeV protons but the enhancement has been equal for the metallic NP and the water replacement. Therefore the result is just changed by scaling factors due to different cross sections for the proton projectiles at different velocities. For 300 MeV the doses are reduced accordingly.

The same simulations have been repeated using smaller NPs with a radius of 2 nm. Results are shown in figure 7.6 and are qualitatively the same as for NPs with a radius of 22 nm. A dose enhancement is visible at radial distances up to around 5 nm away from the metallic NPs for all materials except Fe. The enhancement is maximal for Au and Pt. In the simulation results the range of dose enhancement outside the  $r=2$  nm NP is smaller than for a  $r=22$  nm NP. This might be caused by statistical reasons. For the same number of projectiles incident on a NP with a certain size, the buildup of higher energetic secondary electrons can be incomplete for a small NP. From physical considerations it can be concluded that for 80 MeV protons secondary electrons with energies up to around 160 keV can be produced. The maximum energy present in the simulated secondary electron spectra depends on a combination of the choice of the target thickness and the choice of the number of incident projectiles. Low energetic electrons are much more probable to be created than high energetic electrons. For a nanoparticle with a radius as small as 2 nm, the maximum energy of possibly created secondary electrons, which is the least probable to be sampled in the simulation process, requires an extreme high numbers of incident projectiles to be visible in the simulation results.

---

## 7.4 Protons versus electrons

---

Electrons with the same velocity as protons are expected to have a roughly similar behaviour when interacting with matter. Due to different masses and charges, differences can be nevertheless existing. Therefore, simulations have been compared for 80 MeV protons with electrons with an energy of 44 keV, which have an equal velocity. To evaluate differences between electrons and protons, the total and shell specific ionization cross sections have been compared for gold as an exemplary target material. The ionization cross sections are responsible for the yields of secondary electrons through primary ionization events and indirectly, for the yields of Auger electrons. The cross sections are shown in Fig. 7.7, as well as the yield of ionized shells leading to Auger electron creation and the accumulated yield of produced Auger electrons as a function of their initial energy. Most of the Auger electron cascades stem from primary ionizations of intermediate electron shells. Larger Auger electron cascades can be produced after ionization of inner electron shells. From the comparison, it has been observed that total ionization cross

---

---

sections are higher for protons than for electrons at the same velocity. For certain subshells, electron cross sections can exceed the proton cross section, e.g. for shell 10 and 11. For shell number 15 and 16, proton cross sections are higher, leading to an enhanced number of Auger electrons emitted after the ionization of these shells. Resulting Auger electron yields are higher for proton projectiles than for electron projectiles for transitions with energies around 65 eV. Electrons lead to a higher yield of Auger electrons with energies around 35 eV. These transitions can be related to primary ionizations of shell 10 and 11, for which electron subshell ionization cross sections exceed those for protons.

In addition to the comparison of Auger electrons created by protons or electrons with the same velocity, secondary electron spectra and radial dose distributions have been compared. Fig. 7.8 shows evaluations for a small NP with  $r=2$  nm. It could be observed that for electrons, the Auger effect plays a bigger role in enhancing the dose near the NP than in the case of protons. However, the question is, if these differences are justified, as the ionization cross sections used for protons incident on all target materials (besides H<sub>2</sub>O) rely on the Binary Encounter Approximation (BEA) [BoVr1970], which is known to overestimate the emission of very low energy electrons. However, the differences between secondary electron spectra created from metallic NPs in comparison to those from a H<sub>2</sub>O NP remained, even when the cross sections for H<sub>2</sub>O are calculated with BEA as well. Therefore, these tentative results showing a local dose enhancement in the vicinity of a metallic NP are supposed to be valid.

---

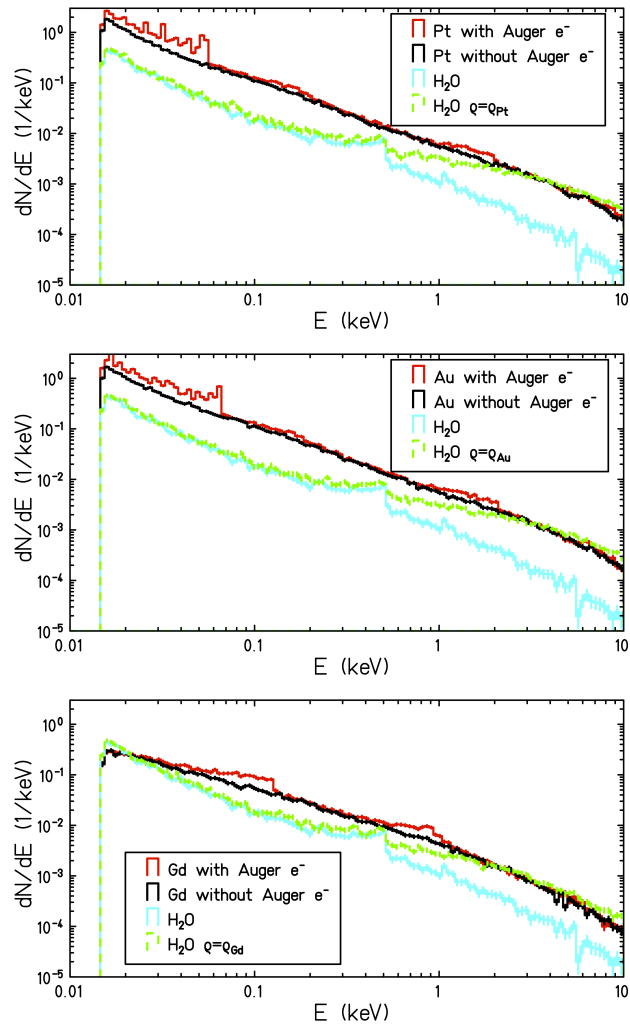


**Figure 7.4:** Spectra of electrons escaping a NP ( $r=22$  nm) are shown with histograms in black. From top to bottom, simulations are shown for Pt, Au and Gd, respectively. The NPs have been irradiated with a disk source of 80 MeV protons covering the whole NP. For further comparisons, the metallic NPs have been replaced by water ( $\rho=1\text{g}/\text{cm}^3$ , lightblue histogram) and water with the same density as the metal (green). Red histograms represent simulations neglecting Auger electrons.

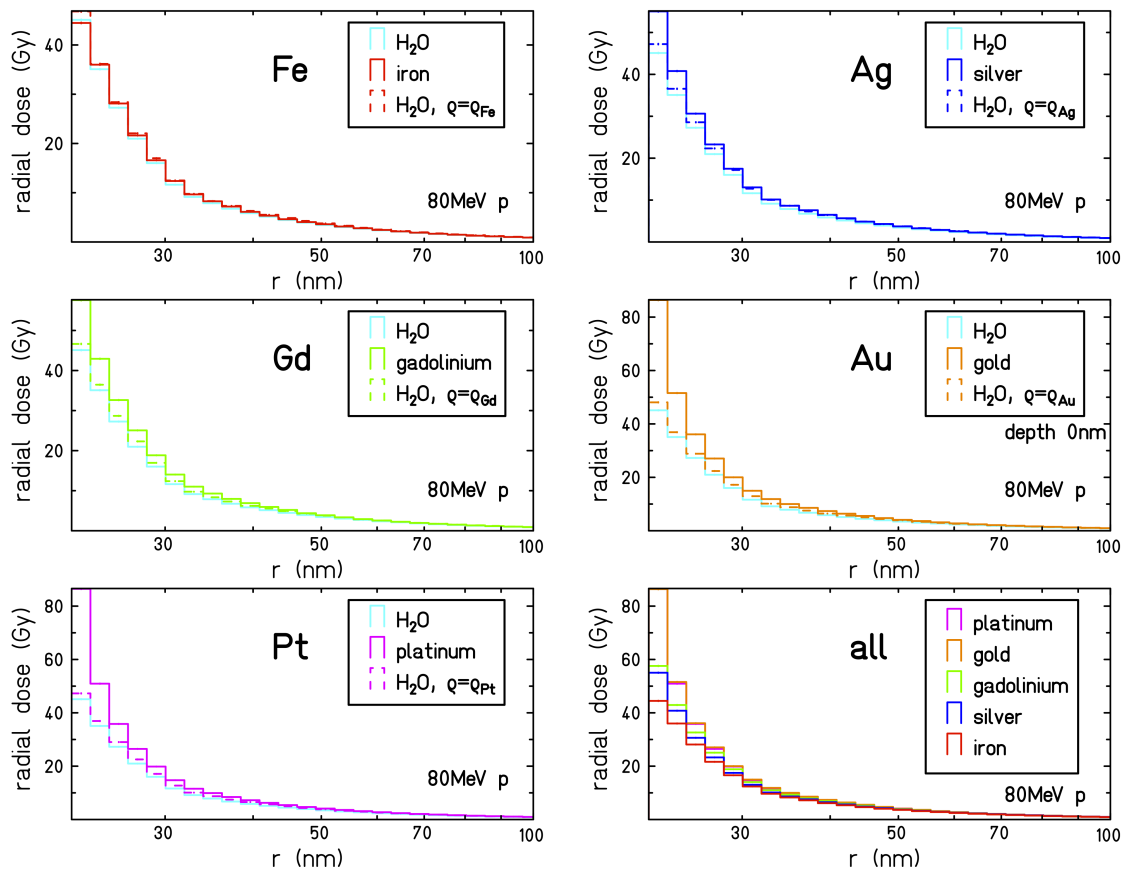


**Figure 7.5:** Radial dose distribution evaluated in spherical shells of 80 MeV protons hitting a nanosphere ( $r=22$  nm) consisting of either Fe, Ag, Gd, Au, Pt,  $H_2O$  or  $H_2O$  with the densities of the corresponding metals. The dose has been evaluated in water surrounding the nanosphere. The radius is measured from the centre of the NP. The effect of an enhanced dose in the presence of a metal NP is maximal in the case of Au and Pt. The bottom figure on the right hand side compares the doses created by all metal NPs.



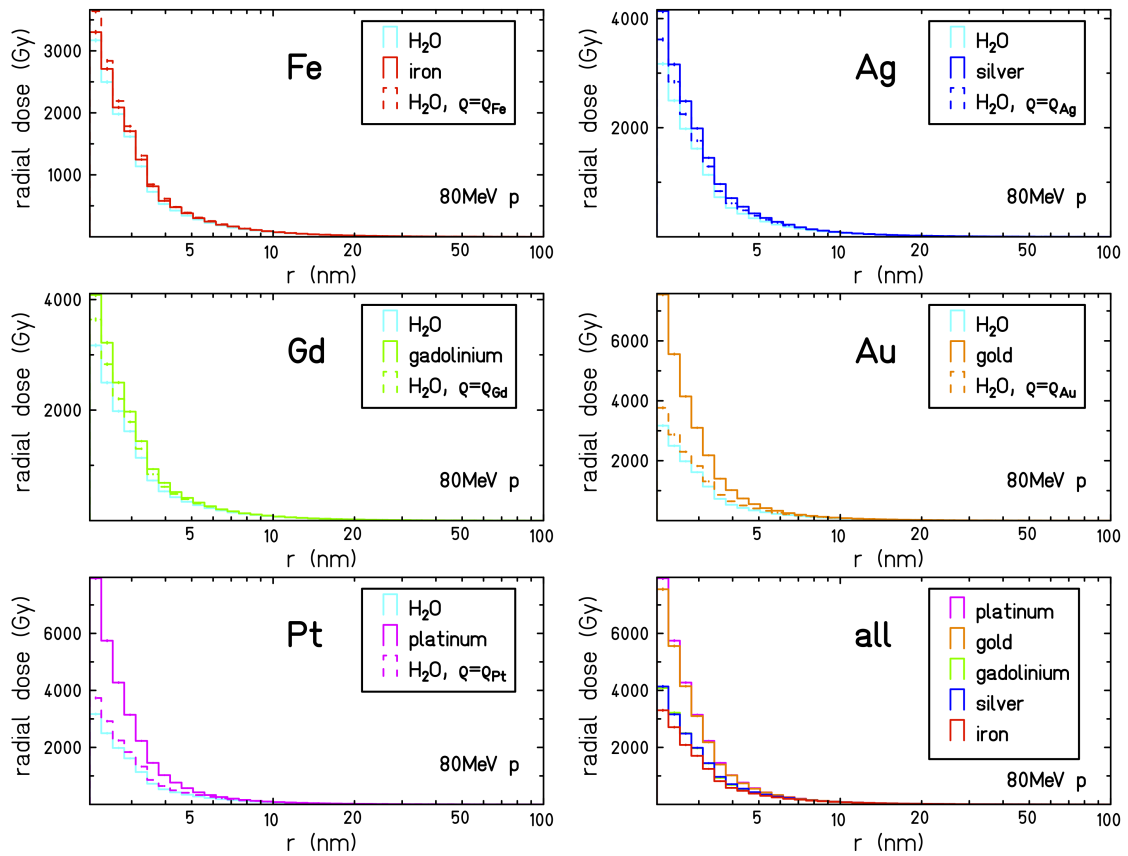


**Figure 7.6:** Radial dose distribution evaluated in spherical shells of 80 MeV protons hitting a nanosphere ( $r=2$  nm) consisting of either Fe, Ag, Gd, Au, Pt,  $H_2O$  or  $H_2O$  with the densities of the corresponding metals. The dose has been evaluated in water surrounding the nanosphere. The radius is measured from the centre of the NP. The effect of an enhanced dose in the presence of a metallic NP is maximal in the case of Au and Pt. The bottom figure on the right hand side compares the doses created by all metal NPs.

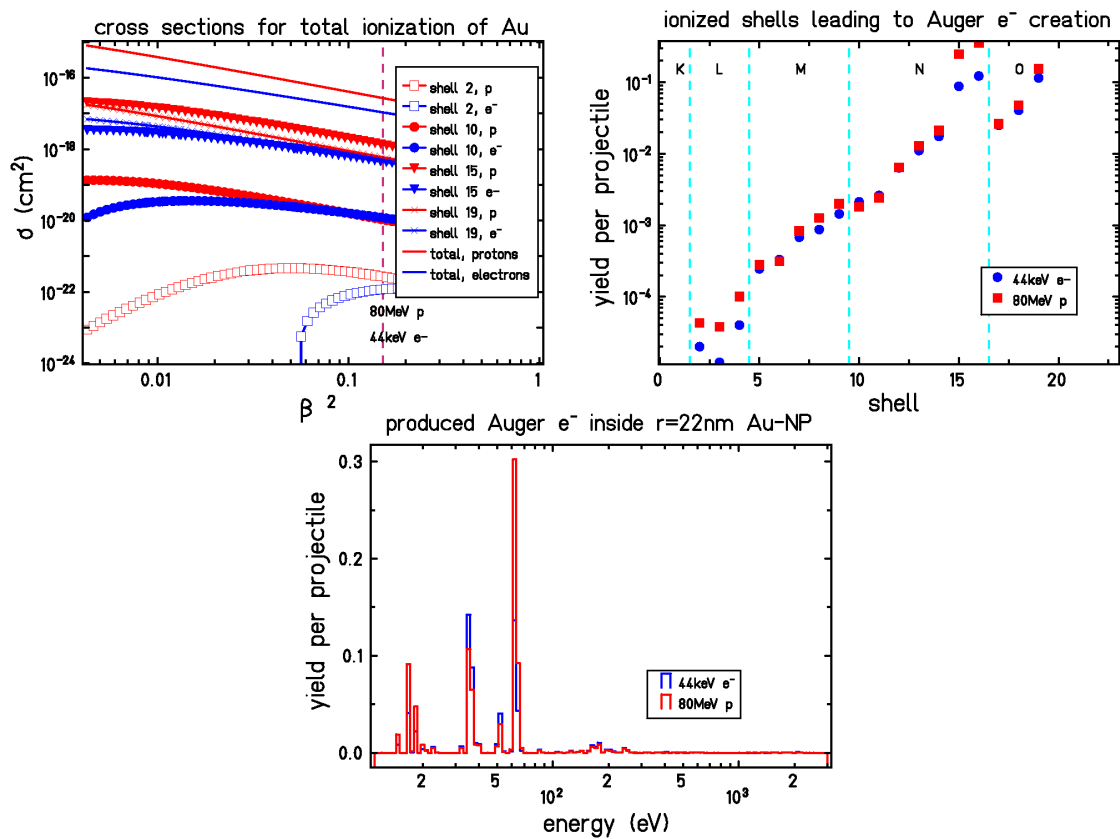


**Figure 7.7:** In the upper picture on the left hand side, total ionization cross sections for Au and electron or proton projectiles are shown. The projectiles are shown with their relativistic beta-factors to compare electrons and protons with equal velocities. A dashed vertical line indicates the beta-squared value corresponding to 80 MeV protons or 44 keV electrons. Shell specific ionization cross sections are shown exemplarily for shells 2, 10, 15 and 19. The upper picture on the right hand side shows ionized shells leading to at least a single Auger electron creation. The lower picture shows produced (not necessarily escaping) Auger electrons inside a  $r = 22$  nm Au NP are shown per projectile for 80 MeV protons (red) and 44 keV electrons (blue).

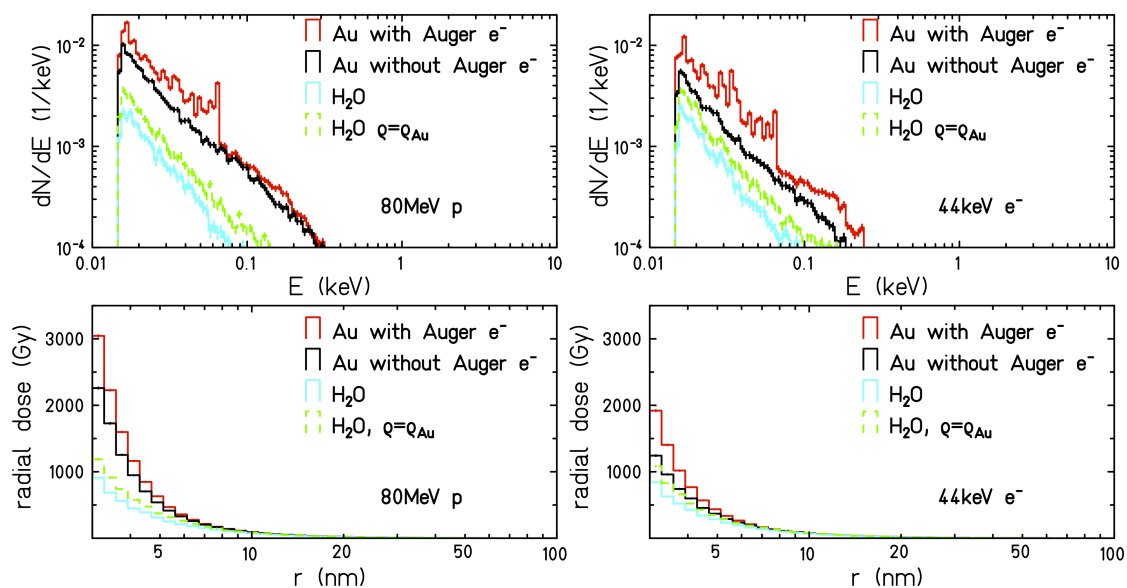


**Figure 7.8:** In the upper panel, secondary electron spectra of electrons escaping a  $r = 2$  nm NP are shown. The lower pictures show the radial dose distribution evaluated in spherical water shells outside the NP. On the left hand side, the simulations have been performed for 80 MeV proton projectiles, while on the right side, 44 keV electrons hit the NP. In all simulations, the NP has either been gold (red histograms), water (light blue) or dense water (green). For comparison, the black histograms represents simulations without Auger electrons.



---

## 8 Summary and Outlook

---

### 8.1 Description of radiation transport

---

One of the aims of this thesis is an improved description of low-energy electron creation and transport in various solid target materials. Ions traversing a material produce a large amount of secondary electrons with low energies which can cause a high local damage. To analyze the effects of ion irradiation, the emission and transport of electrons has to be understood with high accuracy. Describing the transport is a necessary prerequisite to predict damage through ion or electron irradiation on the nanometer scale which is important for various aspects ranging from radiobiology to detector efficiencies. The single interaction track structure MC code TRAX is perfectly suited to study electron interactions down to very low energies. Needed input are appropriate interaction cross sections, which are scarce for energies below 1 keV. Nevertheless, **complete sets of electron cross sections down to energies as low as a few electron Volts** have been compiled and assessed for a broad range of target materials ranging from low-Z materials like carbon, to high Z-materials like gold. The cross sections cover elastic scattering, ionization of sub-shells, electronic excitation and plasmon excitation. The collected sets have been used for simulations with the MC code TRAX and allow to study electron transport in detail. As far as existing, experimental data for electron stopping power, transmission and backscattering have been used to validate these cross sections. Comparisons with experimental data show that for electrons below 1 keV, very few or inconsistent data exists for backscattering and transmission. Basic experiments, measuring electron transmission spectra for primary electron energies below a few keV incident on thin solid state foils (e.g. Al, Fe, Ni, Ag, Au), would be helpful as further benchmarks. The extended code considers **Auger electron emission and transport** in detail which is important for comparisons with measured secondary electron energy spectra. A further extension allowed to handle **non-uniform targets**, a feature which can be important for the description of solid state targets, especially for carbon targets. This may be an important application also for diamond detectors. The extended TRAX code allows to reproduce data from GSI's **Toroid electron spectrometer**. However, a comparison of absolute yields has not been possible due to uncertainties in experimental scaling factors. The overall good agreement with TRAX calculations justifies the neglect of more "exotic" solid state effects such as track potentials [Schiewietz1992], electron jets [Zäpfel2002] and wake effects [RoGe2006]. Besides plasmon excitation, all interaction cross sections are based on single particle collisions. However, with the consideration of non-uniform targets, an important solid state feature has been considered which is necessary to reproduce experimental data for carbon targets. Further evaluations concerning Auger electrons revealed that the usage of Auger electrons as probes for electron emission and transport is limited to target thicknesses of a few nanometers. Nevertheless, TRAX is able to follow the whole tracks of Auger electrons, which allows to interpret Auger electron spectra emitted from a thicker target. As most Auger electrons stem from the surface, care should be taken to avoid contaminations in experiments.

---

## 8.2 Microscopic damage

---

Being able to follow the transport of low-energy electrons allows to predict microscopic damage. The local damage can be described in terms of a radial dose distribution. While different methods to obtain the radial dose distribution differ in their results at radii below a few nanometers, MC calculations should provide a physically realistic result for the radial dose at nanometer distances.

Several aspects have been evaluated that have an impact on nanoscopic damage, like the **elastic scattering of the primary ions** which leads to a natural diffusion of the innermost part of the radial dose distribution. The consideration of **discrete interaction distances** in solids shows that the choice of a minimum radius for the radial dose distribution below interatomic or intermolecular distance is not considered to be realistic. Another aspect that has been evaluated is the **diffusion of radicals**. The coordinates of energy deposition events by excitation and ionization have been randomly shifted following a Gaussian distribution with a constant diffusion width of  $\sigma = 4$  nm (according to [Elsässer2008]), which changed the radial dose profile considerably at low radii. An extension to directly follow radical production and recombination could help to explain the Oxygen Enhancement Ratio effect [Barendsen1966] for particle therapy on the track structure level, i. e. as a function of LET.

Moreover, the impact of the **cut-off energy value** for electrons on the radial dose distribution has been evaluated. In the case of water as a target material, reducing the cut-off value from an already low value of 11.5 eV down to 7.4 eV or even down to 1.7 eV has a large impact on the radial dose distribution in the sub nanometer region. Considering a MC cut-off value of 50 eV or 100 eV (as used e.g. in PENELOPE [Salvat2003]), differences become even larger. Provided accurate cross sections for this energy region are given, the cut-off value should be chosen as low as possible for the evaluation of the radial dose. However, considering electrons with energies as low as a few electron Volts might make it necessary to consider effects like quantum interference. This effect might play a role if the de Broglie wavelength of an electron becomes comparable to interatomic distances. The consequences are so far not quantifiable.

E. g., LEM can be used to predict **biological damage** of ion irradiation in terms of RBE values. It relies on radial dose distributions as input parameters with a  $r_{\min}$  value of 0.1 nm . LEM is very sensitive on dose values at small radii.

However, calculating a radial dose distribution with a MC simulation down to a minimum radius  $r_{\min}$  on the nanometer scale leads to conceptual problems. A dose is an average value for an energy deposition per unit mass. Considering small volumes by the choice of a small value for  $r_{\min}$ , the volume of consideration might contain only a few single molecules. The energy depositions in this volume would be accumulated to single molecules. Calculating an average dose for a single molecule is not reasonable. Considerations of local energy depositions rather than the calculation of a local dose would be appropriate. To predict the biological damage of ions in radiotherapy, a full simulation covering single inelastic interactions rather than using an average radial dose distribution might be necessary. This might be also true for radial dose calculations concerning **detector efficiencies**, e.g. for TLDs. If the radial dose value at sub nanometer distances has to be known, all physical effects have to be considered, including the fact that ions passing the dosimeter can scatter elastically changing their initial travelling direction.

---

---

### 8.3 Metallic nanoparticles in combination with ion beam radiotherapy

---

TRAX now allows to study Auger electron creation and transport in all details, which is why it is perfectly suited to examine the importance of Auger electrons and cascades emitted in metallic nanoparticles under ion or electron irradiation. This aspect has so far not been studied for ion beam irradiation by theoretical calculations. For protons incident on metallic nanoparticles, a local dose enhancement of up to a factor of 2 can be found for energies 2 MeV, 80 MeV and 300 MeV. The most beneficial materials seem to be Au and Pt, followed by Gd and Ag. However, the enhancement is only partially due to **Auger electron cascades**. Even though cascades can comprise many electrons, most significant dose contributions stem from single Auger electrons. TRAX allows to obtain detailed information about produced Auger electrons in all considered materials. Quantitative and qualitative differences have been observed. While Au and Pt nanoparticles emit many Auger electrons at energies well below 100 eV, Auger electrons emitted from Gd are higher in energy but have a significantly lower yield. Moreover, for Au and Pt nanoparticles, a generally enhanced low-energy secondary electron yield causes additional dose contributions. These tentative studies show the potential to use Pt, Au, Gd and Ag nanoparticles as dose enhancing agents in ion beam radiotherapy.

---





---

## 9 Appendix

---

### 9.1 Radial dose calculations for TLDs

---

The radial dose at distances a few nanometer away from an ion track is of crucial knowledge for dosimetry using condensed phase detection systems like thermoluminescence dosimeters (TLDs). TLDs provide a high spatial resolution and do not disturb the radiation field. To obtain the efficiency of these dosimeters, the radial dose serves as an input parameter. Especially the region of a few nanometers around the ion track is of high importance as the dose response of TLDs usually saturates at doses of a few Gray up to a few thousand Gray. Therefore TLDs are susceptible to high dose levels which can be found inside the core of an ion track. TLDs respond nonlinearly due to the saturation effects. Hence, the radial dose distribution has to be known with high precision, especially for low energetic ions with high atomic numbers.

Most TLDs are based on LiF. The radial dose profiles of ions incident on LiF can therefore be used to calculate the efficiency of these detectors [Horowitz1984, Horowitz2001]. Usually, radial dose calculations are performed in water which are scaled with the density of LiF.

To obtain radial dose calculations for TLDs, without having to scale results for water, cross sections for LiF have been assessed. As cross sections for LiF itself have not been available, cross sections for Li and F have been calculated separately and combined using the Bethe summing rule:

$$\sigma(LiF) = \sigma(Li) + \sigma(F) \quad (9.1)$$

---

#### Lithium

---

Electronic excitation cross sections for lithium have been compiled from calculations using the ACE code. Ionization has been calculated using the BEB. Elastic scattering cross sections have been obtained from screened Rutherford calculations.

ACE does not only provide excitation cross sections based on distorted wave approximations, but also ionization cross sections. The total stopping power derived from a summation of contributions from ACE excitations and ionizations based on the BEB is higher than the NIST values which are supposed to be appropriate at high energies. Stopping power values considering ACE ionization cross sections are supposed to provide a better agreement. As BEB cross sections are supposed to be suitable for the ionization of electrons over a larger energy range, a possible choice of inappropriate input parameters might be assumed (B or U values) to explain deviations in the resulting stopping power.

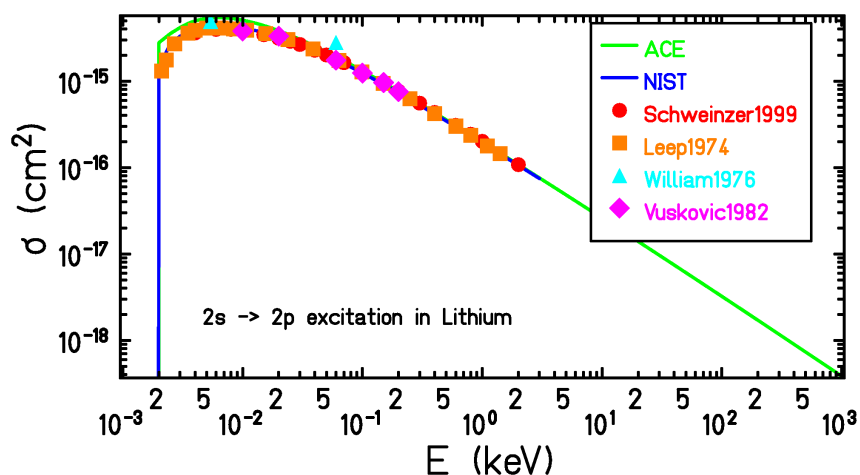


**Figure 9.1:** Cross sections for the 2s-2p electron excitation of Li. ACE calculations are compared with calculations provided on the NIST [NIST] webpage as well as existing experimental results mentioned by NIST. ACE cross sections are based on distorted wave approximations and NIST cross sections on plane wave Born approximations which have been scaled in order to be more suitable for low energies.

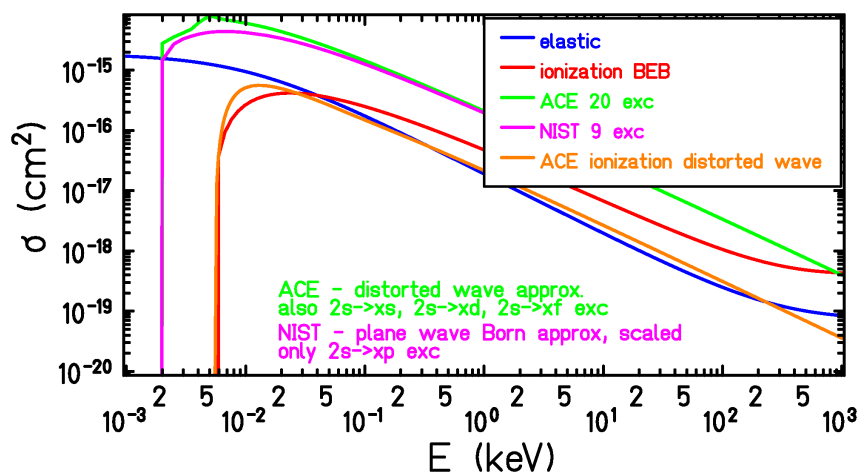


**Figure 9.2:** Complete set of cross sections for electrons on Li.

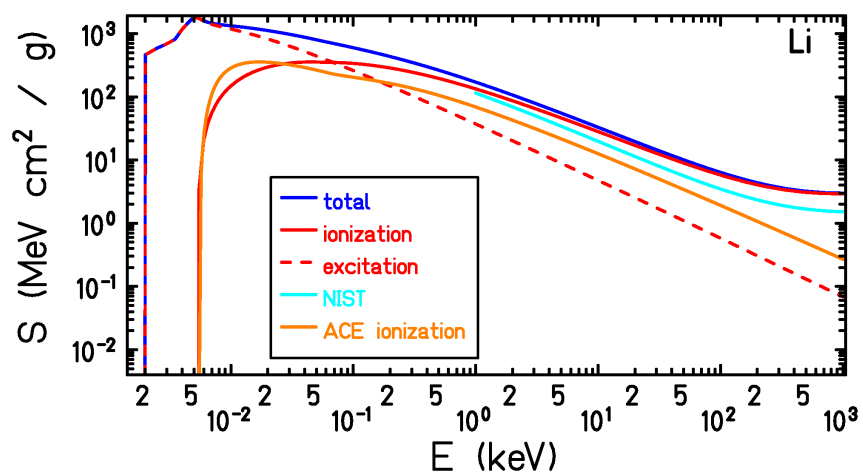


Figure 9.3: Comparison of values for stopping power of electrons on Li.

---

## 9.1.1 Fluoride

---

Electronic excitation cross sections for fluoride have been compiled from calculations using the ACE code. Ionization has been calculated using the BEB. Elastic scattering cross sections have been obtained from screened Rutherford calculations.

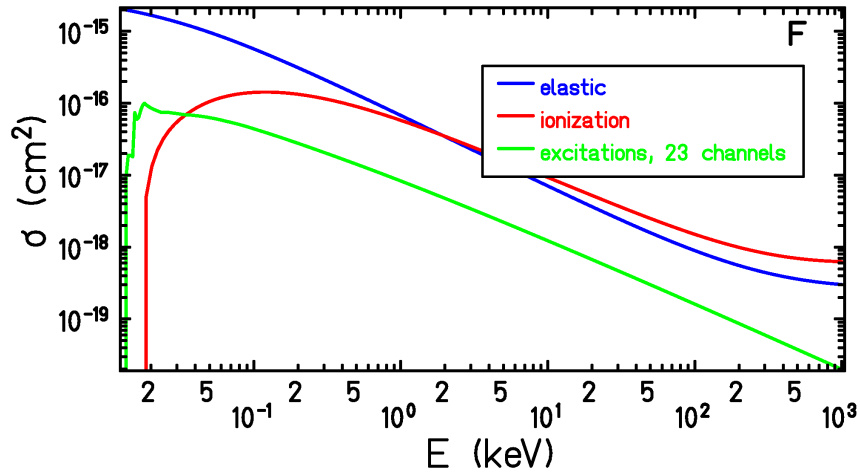


Figure 9.4: Cross sections for electrons on F

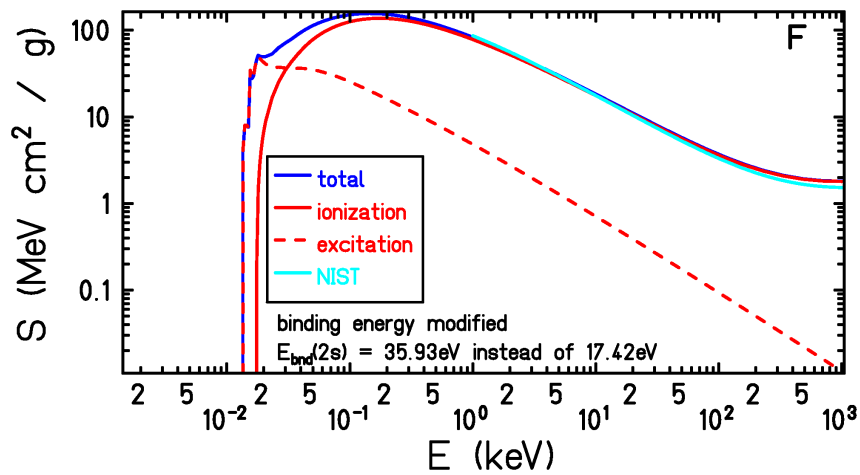


Figure 9.5: Comparison of values for stopping power of electrons on F

---

---

## 9.1.2 Lithiumfluoride

---

The cross sections for lithium and fluoride have been summed to obtain cross sections for LiF.

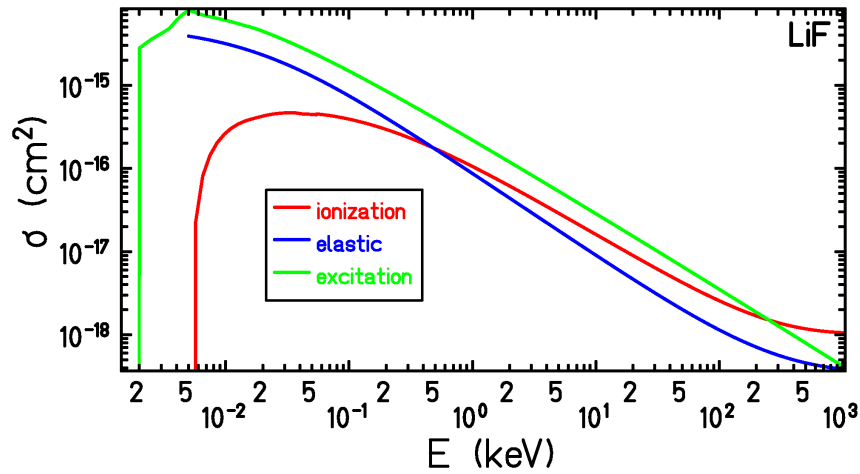


Figure 9.6: Cross sections for electrons on LiF

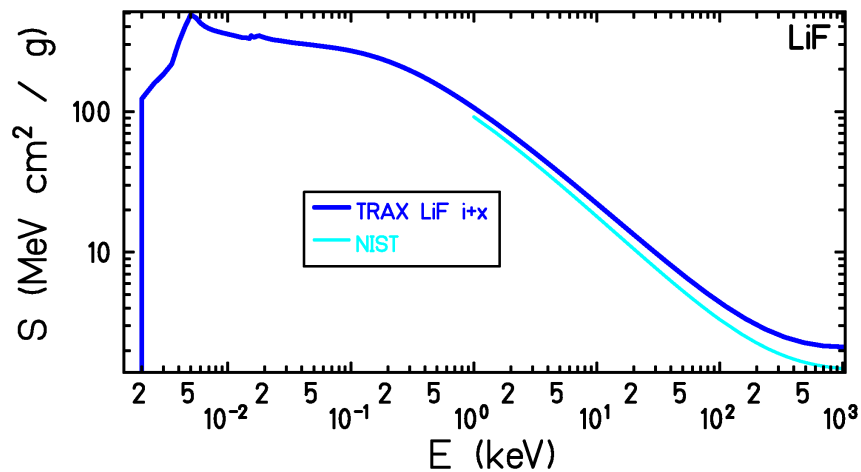


Figure 9.7: Comparison of values for stopping power of electrons on LiF. TRAX stopping powers include contributions from ionization (i) and excitation (x). In total, 43 excitation channels from Li and F are considered from ACE calculations.

---

### 9.1.3 Radial dose calculations

---

TRAX simulations have been performed to determine the radial dose of 0.65 MeV/u He ions in LiF and H<sub>2</sub>O. TRAX calculations use an electron cut-off energy of 10 eV. For the calculations in LiF, electron cross sections mentioned in this sections have been used. Cross sections for ionization by helium ions are based on BEA. To account for excitations by the helium ions, excitation cross sections for electron projectiles have been scaled. For TRAX calculations scaled from H<sub>2</sub>O, the results for the radial dose distribution have been multiplied by a factor of 2.19 to account for differences in density to LiF.

The calculations mentioned in [Horowitz2001] are based on MC calculations in LiF, where a cut-off energy of 50 eV has been used. The radial dose profile shown in comparison to TRAX calculations in Fig. 9.8 has been digitized from a plot shown in [Horowitz2001]. This radial dose profile has been calculated by a code mentioned in [Avila1996, Avila1999]. The calculations are based on the dielectric formalism to account for solid state features in LiF.

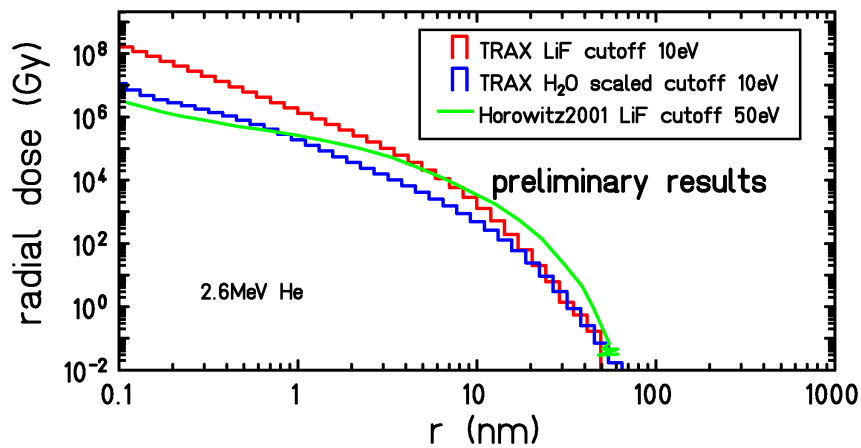


**Figure 9.8:** Comparison of radial dose distributions for 0.65 MeV/u He ions in LiF and H<sub>2</sub>O.

---

---

## 9.2 Complete sets of electron cross sections

---

Complete sets of electron cross sections are shown for carbon and gold. They show the relevance of excitation at low energies compared to ionization which becomes more important as a source of energy loss at higher energies.

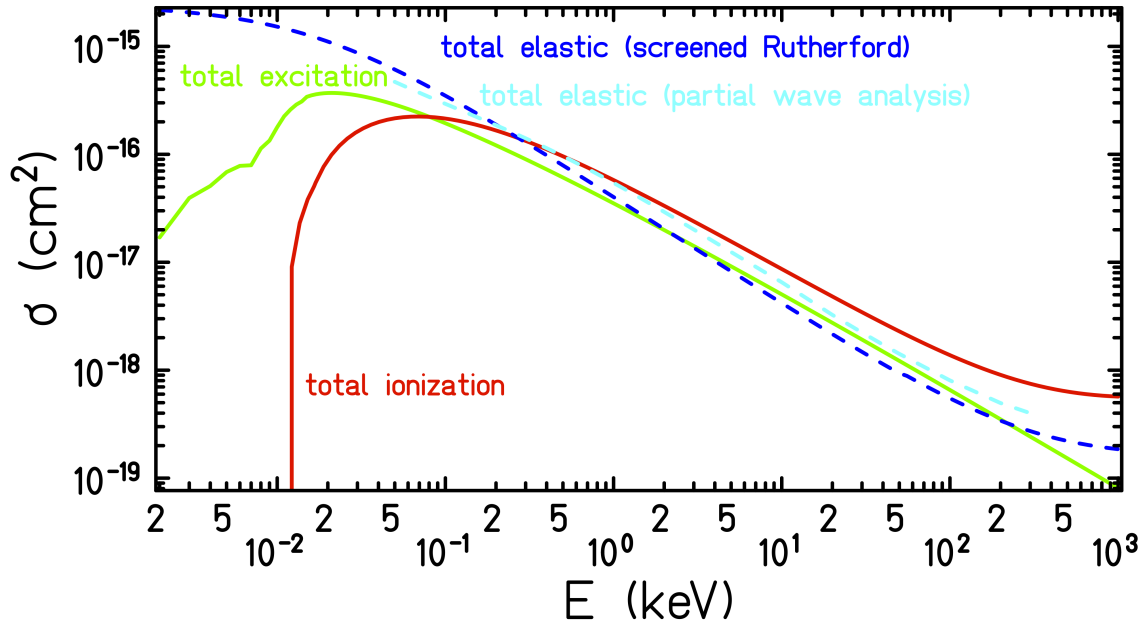


Figure 9.9: Complete set of cross sections for electrons incident on carbon.

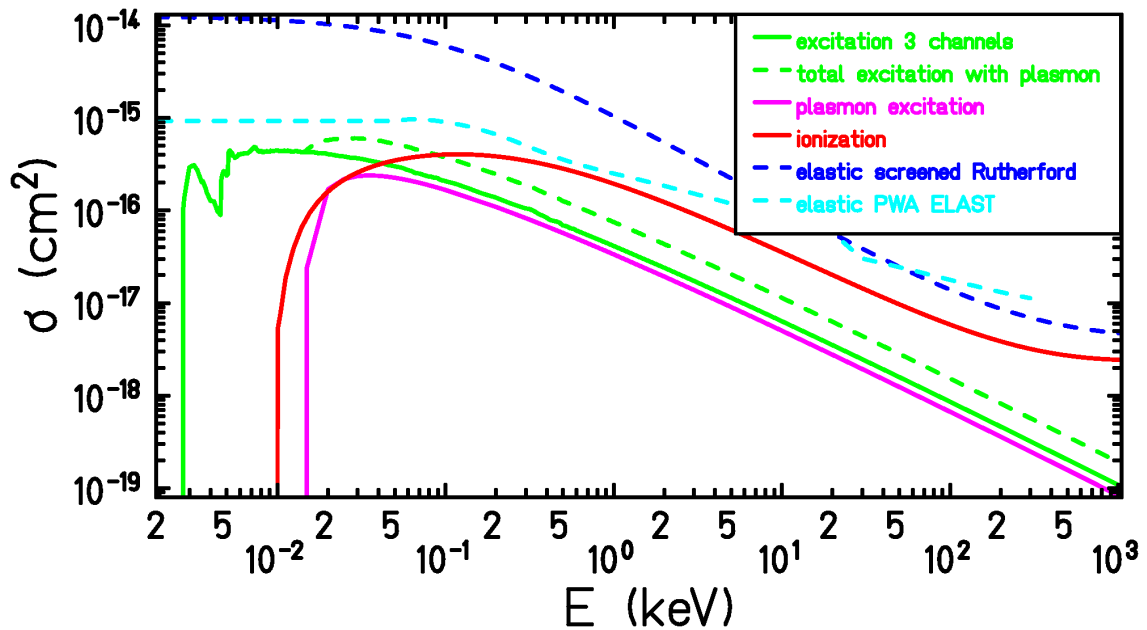


Figure 9.10: Cross sections for electrons on gold.

---





---

## Bibliography

- [AgAl2003] S. Agostinelli, J. Allison, K. Amako *et al.*, Nucl. Instrum. Meth. A **506**, (2003) 250.
- [AlWa1983] K. O. Al-Ahmad and D. E. Watt, J. Phys. D **16(11)**, (1983) 2257.
- [AMe1976] N. W. Ashcroft and N. D. Mermin, *Solid State Physics*, Saunders, (1976).
- [Avila1996] O. Avila *et al.*, Radiat. Prot. Dosim. **65**, (1996) 37-40.
- [Avila1999] O. Avila *et al.*, J. Phys. D **32**, (1999) 1175-1181.
- [Bambynek1972] W. Bambynek *et al.*, Rev. Mod. Phys. **44**, (1972) 716.
- [Barendsen1966] G. W. Barendsen *et al.* Int. J. Radiat. Biol. Relat. Stud. Phys. Chem. Med. **10**, (1966) 317.
- [Barkas1963] W. H. Barkas, Nuclear Reserach Emulsions Vol.1, Academic Press, New York, (1963).
- [Berger1963] M. J. Berger, Meth. Comp. Phys., Vol. 1, (1963) 135.
- [Berger2005] M. J. Berger *et al.*, *Stopping-Power and Range Tables for Electrons, Protons and Helium Ions*, NIST standard reference database 124, (2005).
- [BeWa1988] M. Berger and R. Wang, *Multiple scattering angular deflections and energy-loss straggling*, In: Jenkins, T.M., Nelson, W.R., Rindi, A. (Eds.), Monte Carlo Transport of Electrons and Photons, Plenum Press, New York, (1988) 21-56.
- [Bethe1930] H. A. Bethe, Ann. Phys. (Leipzig) **5**, (1930), 325-400.
- [Bethe1932] H. A. Bethe, Z. Phys. **76**, (1932) 293.
- [Bishop1963] H. E. Bishop, PhD Thesis, University of Cambridge, (1963).
- [BlGa2007] F. Blanco and G. Garcia, Physics Letters A **360(6)**, (2007) 707-712.
- [Bloch1933] F. Bloch, Ann. Phys. **16**, (1933) 285.
- [BNL] BNL National Nuclear Data Center, Sigma Database, <http://www.nndc.bnl.gov/sigma/>
- [BoVr1970] T. F. Bensen and L. Vriens, Physica **47**, (1970) 307-319
- [BoSa2002] B. Boudaiffa, P. Cloutier, D. Hunting, M. A. Huels and L. Sanche, Radiat. Res. **157(3)**, (2002) 227-234.
- [Braeuning2003] H. Bräuning, A. Bräuning-Demian, G. Bednarz, F. Bosch, X. Cai, C. Cohen, D. Dauvergne, A. Gumberidze, R. Kirsch, C. Kozhuharov *et al.*, Nucl. Instrum. Meth. B **205**, (2003) 826.
- [BrJo1983] B. H. Bransden and C. J. Joachain, *Physics of Atoms and Molecules*, (Longman, London), (1983).

- 
- [Bronstein1969] I. M. Bronstein and B. S. Fraiman, *Vtorichnaya Elektronnaya Emissiya*, Moskau, (1969) 340.
- [Brook1978] E. Brook *et al.*, *J. Phys. B* **11(17)**, (1978).
- [Browning1994] R. Browning, T. Z. Li, B. Chui, J. Ye, R. F. W. Pease *et al.*, *J. Appl. Phys.* **76**, (1994) 2016.
- [Burke1971] P. G. Burke, A. Hibbert and W. D. Robb, *J. Phys. B* **4**, (1971) 153.
- [BuDu1994] P. G. Burke, V. M. Burke and K. M. Dunseath, *J. Phys. B* **27**, (1994) 5341.
- [BuKa1967] J. J. Butt and R. Katz, *Radiat. Res.* **30**, (1967) 855.
- [Clark1988] R. E. H. Clark *et al.*, *ACE: Another Collisional Excitation Code*, Los Alamos National Laboratory, LA-11436-M, Vol. II, Manual, (1988).
- [ChSch1976] A. Chatterjee and H. J. Schaefer, *Radiat. Environ. Biophys.* **13**, (1976) 215-227.
- [ChHo1991] A. Chatterjee and W. R. Holley, *Int. J. Quant. Chem.* **39**, (1991) 709-727.
- [Chow2012] J. C. L. Chow, M. K. K. Leung and D. A. Jaffray, *Phys. Med. Biol.* **57**, (2012) 3323.
- [Cowan1981] R. D. Cowan, *Theory of Atomic Structure and Spectra*, (University of California Press, Berkeley and Los Angeles, Calif.), (1981).
- [Cucinotta1995] F. Cucinotta *et al.*, *NASA Technical Memorandum* **3497**, (1995) 1.
- [Cucinotta1998] F. Cucinotta *et al.*, *Radiat. Environ. Biophys.* **37**, (1998) 259.
- [Desclaux1977] J. P. Desclaux, *Comput. Phys. Comm.* **9**, (1977) 31; erratum, *ibid.* **13**, (1977) 71.
- [Dingfelder1998] M. Dingfelder *et al.*, *Radiat. Phys. Chem.* **53**, (1998) 1-18.
- [Dingfelder1999] M. Dingfelder, D. Hantke, M. Inokuti and H. G. Paretzke, *Radiat. Phys. Chem.* **53(1)**, (1999) 1-18.
- [Dunseath1993] K. M. Dunseath *et al.*, *JET Order No. JP2*, (1993) 11566.
- [Elsässer2008] T. Elsässer *et al.*, *New J. Phys.* **10**, (2008) 075005.
- [Elsässer2010] T. Elsässer *et al.*, *Int. J. Radiat. Oncol. Biol. Phys.* **78**, (2010) 1177-1183.
- [Fano1954] U. Fano, *Phys. Rev.* **93**, (1954) 117.
- [Fernandez1993] J. M. Fernández-Varea *et al.*, *J. Phys.: Condensed Matter* **5**, (1993) 3593-3610.
- [Fernandez1996] J. M. Fernandez-Varea, D. Liljequist, S. Csillag, R. Rdtty and F. Salvat, *Nucl. Instrum. Meth. B* **108**, (1996) 35-50.
- [Fernandez2012] J. M. Fernández-Varea *et al.*, *Int. J. Radiat. Biol.* **88(1-2)**, (2012) 66.
- [FrIn2011] Z. Francis, S. Incerti, R. Capra *et al.*, *Appl. Radiat. Isotopes* **69(1)**, (2011) 220-226.
- [FrWe1990] R. S. Freund, R. C. Wetzal *et al.*, *Phys. Rev. A* **41**, (1990) 3575.
- [Friedland2003] W. Friedland, P. Jacob, P. Bernhardt, H. G. Paretzke and M. Dingfelder, *Radiat. Res.* **159**, (2003) 401-410.
- [FuMc1973] J. B. Furness and I. E. McCarthy, *J. Phys. B: At. Mol. Phys.* **6**, (1973) 2280.
- [Ganas1981] P. S. Ganas, *Physica* **104C**, (1981) 411-415.
-

- 
- [Geant4] Geant4 Collaboration, *Physics Reference Manual*, Version: *geant4 9.5.0*, <http://geant4.cern.ch>, (2011).
- [Geiss1999] O. Geiß, M. Krämer and G. Kraft, *Nucl. Instrum. Meth. B* **142(4)**, (1999) 592-598.
- [GrSt1972] A. E. S. Green and R. S. Stolarski, *J. Atm. Terr. Phys.* **34**, (1972) 1703-1717.
- [GrWa1978] B. Grosswendt, E. Waibel, *Nucl. Instrum. Methods* **155**, (1978) 145-156.
- [Gomati1997] M. M. El Gomati and A. M. D. Assad, *Proc. 5th European Workshop on Microbeam Analysis*, (1997).
- [Gomati2008] M. M. El Gomati, C. G. H. Walker, A. M. D. Assa'd and M. Zandrakil, *Scanning* **30**, (2008) 2-15.
- [Gottschalk1993] B. Gottschalk *et al.*, *Nucl. Instrum. Meth. B* **74**, (1993) 467-490.
- [Gupta2010] M. Gupta, CERN, (2010), <http://cds.cern.ch/record/1279627/files/PH-EP-Tech-Note-2010-013.pdf>.
- [Hainfeld2004] J. F. Hainfeld, D. N. Slatkin and H. M. Smilowitz, *Phys. Med. Biol.* **49**, (2004) 309.
- [Hainfeld2008] J. F. Hainfeld, F. Dilmanian, D. N. Slatkin and H. M. Smilowitz, *J. Pharm. Pharmacol.* **60(8)**, (2008) 977.
- [HaReWa2005] D. Halliday, R. Resnick and J. Walker, *Fundamentals of Physics*, 7th Edition, Wiley International Edition, ISBN 0-471-46508-9, (2005).
- [Heinrich1966] K. F. J. Heinrich, *Proc. 4th Conf. on X-ray Optics and Microanalysis*, ed R. Castaign *et al.*, Paris, (1966) 159.
- [Highland1975] V. L. Highland, *Nucl. Instrum. Methods* **129**, (1975) 497.
- [Horowitz1984] Y. Horowitz, *Thermoluminescence and Thermoluminescent Dosimetry* vol 1 and 2 (Boca Raton, Florida: CRC Press), (1984, 2008)
- [Horowitz2001] Y. S. Horowitz *et al.*, *Nucl. Instrum. Meth. B* **184**, (2001) 85-112.
- [Hovington1996] P. Hovington *et al.*, *Scanning Microsc.* **10**, (1996) 653.
- [Hubbard1955] J. Hubbard, *Proc. Phys. Soc. (London) A* **68**, (1955) 976-986.
- [Hubbel1994] J. H. Hubbel *et al.*, *J. Phys. Chem. Ref. Data* **23(2)**, (1994) 339-364.
- [HuKü1979] H-J. Hunger, L. Küchler, *Phys. Stat. Sol. (a)* **56**, (1979) K45.
- [ICRU1984] ICRU Report **37**, *Stopping Powers for Electrons and Positrons*, Bethesda, Maryland, USA, (1984).
- [Inokuti1994] M. Inokuti (Ed.), *Advances in Atomic, Molecular, and Optical Physics* **33**, Academic Press, (1994).
- [JaSa2004] A. Jablonski, F. Salvat and C. J. Powell, *J. Phys. Chem. Ref. Data* **33**, (2004) 409.
- [JaSa2010] A. Jablonski, F. Salvat and C. J. Powell, *NIST Electron Elastic-Scattering Cross-Section Database - Version 3.2*, National Institute of Standards and Technology, Gaithersburg, MD (2010).
- [Joy1995a] D. C. Joy, *Monte Carlo Modeling for Electron Microscopy and Microanalysis*, Oxford University Press, New York, (1995).
-

- 
- [Joy1995] D. C. Joy, *A database on electron-solid interactions*, Scanning **17**, (1995) 270.
- [KiRu1994] Y.-K. Kim and E. Rudd, Phys. Rev. A **50**, (1994) 3954-3967.
- [Kim2000] Y.-K. Kim, J. P. Santos and F. Parente, Phys. Rev. A **62**, (2000) 052710.
- [KiSt2001] Y.-K. Kim and P. M. Stone, Phys. Rev. A **64**, (2001) 052707.
- [KiDe2002] Y.-K. Kim, J.-P. Desclaux, Phys. Rev. A **66**, (2002), 012708.
- [Kim2012] J.-K. Kim *et al.*, Phys. Med. Biol. **57**, (2012) 8309.
- [KyEm2013] I. Kyriakou, D. Emfietzoglou, A. Nojeh and M. Moscovitch, J. Appl. Phys. **113**, (2013) 084303 .
- [KrKrSch1992] G. Kraft, M. Krämer, M. Scholz, Radiat. Environ. Biophys. **31(3)**, (1992) 161-180.
- [KrKr1994] M. Krämer and G. Kraft, Radiat. Environ. Biophys. **33(2)**, (1994) 91-109.
- [Kraemer1995] M. Krämer, Nucl. Instrum. Methods B **105**, (1995) 14-20.
- [Kraemer2000] M. Krämer *at al.*, Phys. Med. Biol. **45**, (2000) 3299-3317.
- [KrSch2000] M. Krämer and M. Scholz, Phys. Med. Biol. **45**, (2000) 3319-3330.
- [KrDu2010] M. Krämer and M. Durante, Eur. J. Phys. D **60**, (2010) 195.
- [KoKa1968] E. J. Kobetich and R. Katz, Phys. Rev. **170**, (1968) 391-396.
- [KoKa1969] E. J. Kobetich and R. Katz, Nucl. Instrum. Methods **71**, (1969) 226.
- [Liljequist2012] D. Liljequist, T. Liamsuwan and H. Nikjoo, International Journal of Radiation Biology **88**, (2012) 29.
- [Lineva2008] N. Lineva, PhD thesis, TU Darmstadt, GSI (2008), <http://www.gsi.de/documents/DOC-2008-Aug-25-1.pdf>.
- [Lineva2009] N. Lineva *et al.*, Nucl. Instrum. Meth. B **267**, (2009) 891-895.
- [Lindhard1954] J. Lindhard, K. Dan. Vidensk. Selsk. Mat. Fys. Medd. **28(8)**, (1954) 1-57.
- [LoDu2013] J. S. Loeffler and M. Durante *Nat. Rev. Clin. Oncol.* advance online publication 21 May 2013; doi: 10.1038/nrclinonc.2013.79, (2013)
- [Luo1991] S. Luo *et al.*, Rad. Eff. Defects Solids **117**, (1991) 235.
- [LyDa1991] G. R. Lynch and O. I. Dahl, Nucl. Instrum. Meth. B **58**, (1991) 6-10.
- [MaCh1979] J. L. Magee and Chatterjee *Chemical effects in condensed systems*. In: S. Okada, M. Imamura, T. Terashina (eds), Proceedings of the 6 JCRR Congress Tokyo (1979)
- [Mann1983] J. B. Mann, Atomic Data and Nuclear Data Tables **29**, (1983), 407-452.
- [Marquardt1963] D. W. Marquardt, *An Algorithm for Least-Squares Estimation of Nonlinear Parameters*, J. Soc. Ind. Appl. Math., Vol II, no. 2, (1963) 431-441.
- [Maslov2008] M. Maslov *et al.*, Phys. Rev. A **77**, (2008) 062711.
- [McMahon2011] S. McMahon *et al.*, Nature Sci. Rep. **1**, (2011) 18.
- [Michaud2003] M. Michaud, A. Wen and L. Sanche, Radiat. Res. **159**, (2003) 3.
- [Molière1948] G. Molière, Z. Naturforsch. **3A** (1948) 78.
-

- 
- [Moore1970] C. E. Moore, *Selected Tables of Atomic Spectra (NSRDS-NBS)*, Washington Bureau of Standards, section 3, (1970).
- [Nigam1959] B. P. Nigam, M. K. Sundaresan, and T. Y. Wu, *Phys. Rev.* **115**, (1959) 491.
- [Nikjoo2006] H. Nikjoo *et al.*, *Rad. Meas.* **41**, (2006) 1052-1074.
- [NIST] <http://physics.nist.gov> NIST-ESTAR database
- [PaBe1978] H. G. Paretzke, M. J. Berger, *Stopping power and energy degradation for electrons in water vapor.*, In: J. Booz, H. G. Ebert (eds), *Proceedings of the 6th symposium on microdosimetry*. Harwood, Brussels,, (1978), 749-758.
- [Palluel1947] P. Palluel, *Compt. Rendu* **224**, (1947) 1492.
- [Paretzke1980] H. G. Paretzke, *Advances in energy deposition theory*, In: *Advances in Radiat. Protect. and Dosimetry in Medicine*, (1980).
- [Paretzke1988] H. G. Paretzke, *Simulation von Elektronen-Spuren im Energiebereich 0,01-10 keV im Wasserdampf.* **39**, GSF-Bericht 5, (1988).
- [Penn1987] D. R. Penn, *Phys. Rev. B* **35(2)**, (1987) 482-486.
- [PeCu1991] S.T. Perkins, D.E. Cullen, et al., "Tables and Graphs of Atomic Subshell and Relaxation Data Derived from the LLNL Evaluated Atomic Data Library (EADL), Z = 1 - 100", UCRL-50400, Vol. 30, Lawrence Livermore National Laboratory (1991).
- [PeCu1991a] S. T. Perkins, D. E. Cullen, and S. M. Seltzer, *Tables and Graphs of Electron-Interaction Cross Sections Derived from the LLNL Evaluated Electron Data Library (EEDL), Z = 1-100*, Lawrence Livermore National Laboratory, Livermore, CA, Vol. 31, (1991).
- [PhWe1963] J. Philibert and E. Weinryb, *Proc. 3rd Conf. on X-ray Optics and Microanalysis*, (1963) 163.
- [Polf2011] J. Polf *et al.*, *Appl. Phys. Lett.* **98**, (2011) 193702.
- [Porcel2010] E. Porcel *et al.*, *Nanotechnology* **21**, (2010) 085103.
- [Quinn1962] J. J. Quinn, *Phys. Rev.* **126**, (1962) 1453.
- [ReDr1977] L. Reimer and H. Drescher, *J. Phys. D.* **10**, (1977) 805.
- [Robar2002] J. L. Robar, S. A. Riccio and M. A. Martin, *Phys. Med. Biol.* **47**, (2002) 2433.
- [RoGe2006] H. Rothard, B. Gervais, *Mat. Fys. Medd. Dan. Vid. Selsk.* **52**, (2006) 497-524.
- [Rudd1988] M. E. Rudd, *Phys. Rev. A* **38**, (1988) 6129-6137.
- [Salvat2003] F. Salvat *et al.*, *Proceedings of a Workshop/Training Course OECD/NEA, 7-10 July (2003)*, <http://www.nea.fr/html/dbprog/peneloperef.html>
- [Salvat2008] F. Salvat *et al.*, *PENELOPE - A Code System for Monte Carlo Simulation of Electron and Photon Transport, Proceedings of a Workshop/Training Course OECD/NEA, ISBN 978-92-64-99066-1*, (2008)
- [Schardt2010] D. Schardt, T. Elsässer and D. Schultz-Ertner, *Rev. Mod. Phys.* **82(1)**, (2010) 383-426.
- [Schiewietz1992] G. Schiewietz *et al.*, *Phys. Rev. Lett.* **69**, (1992), 628.
-

- 
- [SchKr1997] M. Scholz, G. Kraft *et al.*, *Radiat. Environ. Biophys.* **36**, (1997) 59.
- [SchKr2004] M. Scholz, G. Kraft *et al.*, *Radiation Research* **161**, (2004) 612-620.
- [Shinotsuka2012] H. Shinotsuka, S. Tanuma, C. Powell and D. Penn, *Nucl. Instrum. Methods B* **270**, (2012) 75.
- [Siegbahn1975] H. Siegbahn, L. Asplund and P. Kelfve, *Chem. Phys. Lett.* **35(3)**, (1975) 330.
- [Simonetti2007] S. Simonetti, A. Juan and G. Brizuela, *Mat. Science Poland* **25(3)**, (2007).
- [Spielberger2002] B. Spielberger *et al.*, *Phys. Med. Biol.* **47(22)**, (2002) 4107-4120.
- [Sternglass1954] E. J. Sternglass, *Phys. Rev.* **95**, (1954), 345.
- [Sternheimer1952] R. M. Sternheimer, *Phys. Rev.* **88**, (1952) 851.
- [Sternheimer1982] R. M. Sternheimer *et al.*, *Phys. Rev. B* **26**, (1982) 6067.
- [StDu1997] N. Stolterfoht, R. D. DuBois and R. D. Rivarola, *Electron emission in heavy ion-atom collisions*, Cambridge University Press, Cambridge (1997).
- [SuKa2006] H. Suno and T. Kato, *Atomic Data and Nuclear Data Tables* **92**, (2006) 407.
- [DanThomas] <http://www.chembio.uoguelph.ca/educmat/atomdata/bindener/elecbind.htm>
- [Thomas1969] S. Thomas and E. B. Pattinson, *Brit. J. Appl. Phys.* **II-2**, (1969) 1539.
- [Trajmar1983] S. Trajmar, D. F. Register, A. Chutjian, *Phys. Rep* **97/5**, (1983) 219-356.
- [Uehara1993] S. Uehara, H. Nikjoo and D. T. Goodhead, *Phys. Med. Biol.* **38**, (1993) 1841-1858.
- [Uehara1992] S. Uehara, H. Nikjoo and D. T. Goodhead, *Phys. Med. Biol.* **37**, (1992) 1841.
- [Usami2007] N. Usami *et al.*, *Int. J. Radiat. Biol.* **83(9)**, (2007) 569.
- [VaNi1984] S. Valkealahti and R.M. Nieminen, *Appl. Phys. A* **35** (1984) 51.
- [Varma1989] M. N. Varma, *Nucl. Tracks Radiat. Meas.* **16(2/3)**, (1989) 135-139.
- [Varma1993] B. Varma, *Nucl. Instrum. Meth. B* **74**, (1993) 467-490.
- [Verma1977] R. L. Verma, *J. Phys. D* **10**, (1977) 1167-1173.
- [Walker1971] D. Walker, *Adv. Phys.* **20(85)**, (1971) 257.
- [Waligorski1986] M. P. R. Waligorski *et al.*, *Nucl. Tracks Radiat. Meas.* **11**, (1986) 309.
- [Waelzlein2013] C. Wälzlein, M. Krämer, E. Scifoni and M. Durante, *Appl. Radiat. Isotopes* **83**, (2014) 171-176.
- [webelements] <http://www.webelements.com>
- [Wentzel1927] G. Wentzel, *Z. Phys.* **43**, (1927) 524-530.
- [GwynWilliams] G. Williams, <http://www.jlab.org/gwyn/ElectronBindingChart-1.pdf>
- [WiBa1976] C. L. Wingate and J. W. Baum, *Radiat. Res.* **65**, (1976) 1.
- [Wittry1966] D. B. Wittry, *Proc. 4th Conf. on X-ray Optics and Microanalysis*, ed R. Castaign *et al.*, Paris, (1969) 168.
- [Zäpfel2002] T. Zäpfel *et al.*, *Nucl. Instrum. Meth. B* **193**, (2002), 651.
-

---

[Zatsarinny2008] O. Zatsarinny *et al.*, Phys. Rev. A **78**, (2008) 042713.

[Zhang1985] C. Zhang *et al.*, Radiat. Protect. Dos. **13**, (1985) 215.

---





---

## List of publications

- [Bleicher2012] M. Bleicher, L. Burigo, M. Durante, M. Herrlitz, M. Krämer, I. Mishustin, I. Müller, F. Natale, I. Pshenichnov, S. Schramm, G. Taucher-Scholz, C. Wälzlein  
*Nanolesions induced by heavy ions in human tissues: Experimental and theoretical studies*  
Beilstein Journal of Nanotechnology **3**, (2012), 556-63.
- [Kraemer2010] M. Krämer, E. Scifoni, C. Wälzlein, M. Durante  
*TRAX simulations*  
GSI Scientific Report 2010, HEALTH-40.
- [Kraemer2012] M. Krämer, E. Scifoni, C. Wälzlein, M. Durante  
*Ion beams in radiotherapy - from tracks to treatment planning*  
J. Phys. Conf. Ser. **373**, (2012) 012017.
- [Savran2010] D. Savran, K. Lindenberg, J. Glorius, B. Löher, S. Müller, N. Pietralla, L. Schnorrenberger, V. Simon, K. Sonnabend, C. Wälzlein  
*The low-energy photon tagger NEPTUN*  
Nucl. Instrum. Meth. A **613(2)**, (2010), 232-239.
- [Schnorrenberger2010] L. Schnorrenberger, K. Sonnabend, J. Glorius, B. Löher, N. Pietralla, D. Savran, V. Simon, C. Wälzlein  
*Nuclear astrophysics with tagged photons: NEPTUN @ S-DALINAC, Darmstadt*  
J. Phys. Conf. Ser. **202(1)**, (2010) 012027.
- [Sonnabend2011] K. Sonnabend, D. Savran, J. Beller, M. A. Büssing, A. Constantinescu, M. Elvers, J. Endres, M. Fritzsche, J. Glorius, J. Hasper, J. Isaak, B. Löher, S. Müller, N. Pietralla, C. Romig, A. Sauerwein, L. Schnorrenberger, C. Wälzlein, A. Zilges, M. Zweidinger  
*The Darmstadt High-Intensity Photon Setup (DHIPS) at the S-DALINAC*  
Nucl. Instrum. Meth. A **640(1)**, (2011) 6-12.
- [Waelzlein2011] C. Wälzlein, M. Krämer, E. Scifoni and M. Durante  
*TRAX Code Extensions*  
GSI Scientific Report 2011, CANCER-48.
- [Waelzlein2012] C. Wälzlein, M. Krämer, E. Scifoni and M. Durante  
*Solid target extensions in TRAX*  
GSI Scientific Report 2012, HEALTH-51.

- 
- [Waelzlein2013] C. Wälzlein, M. Krämer, E. Scifoni and M. Durante  
*Advancing the modeling in particle therapy: From track structure to treatment planning*  
Appl. Radiat. Isotopes **83**, (2014) 171-176.
- [Waelzlein2013a] C. Wälzlein, M. Krämer, E. Scifoni and M. Durante  
*Low-energy electron transport in non-uniform media*  
Nucl. Instrum. Meth. B, accepted (2013).
- [Waelzlein2013b] C. Wälzlein, M. Krämer, E. Scifoni and M. Durante  
*Simulations of dose enhancement for heavy atom nanoparticles irradiated by protons*  
submitted to Phys. Med. Biol., under revision (2013).
-

---

# Lebenslauf

## Persönliche Daten

Name	Cathrin Gabriele Wälzlein
Geburtsdatum	18.03.1986
Geburtsort	Hanau
Staatsangehörigkeit	deutsch
Familienstand	ledig

## Schulbildung

1992-1996	Hasselbachschule, Neuenhaßlau (Grundschule)
1996-2005	Kopernikusschule, Freigericht (Gymnasium mit Oberstufe)
Juni 2005	Abitur (Durchschnittsnote: 1,2)

## Hochschulausbildung

2005-2008	TU Darmstadt B.Sc. Physik (gut) <i>Erweiterung der Fokalebene des Photonentaggers NEPTUN am S-DALINAC</i>
2008-2010	TU Darmstadt M.Sc. Physik (sehr gut) <i>Bestimmung der Bevölkerungswahrscheinlichkeit von <math>^{184m}\text{Re}</math> für die Reaktion <math>^{185}\text{Re}(\gamma, n)</math></i>
seit 2010	TU Darmstadt, Promotionsstudium Stipendiatin beim Beilstein-Institut, Frankfurt Arbeitsgruppe Biophysik an der GSI



---

# Acknowledgements

I would like to thank the **Beilstein-Institute**, which has financed my project in the framework of the NanoBiC project. Without their financial support this work would not have been possible. Besides, I acknowledge the help of many people who encouraged me.

I would like to thank **Prof. Dr. Marco Durante** who has given me the opportunity to perform research in the biophysics group at GSI.

I would like to thank my supervisor **Dr. Michael Krämer** for giving me the opportunity to work on a physics research field that also allowed me to further develop my computational skills. I acknowledge his trust in me for the opportunity to represent him at an international conference and give a talk.

I would like to thank my colleague **Dr. Emanuele Scifoni** for lots of encouraging discussions and his enthusiasm.

I would like to thank my fiancé **Thomas Möller** for supporting and encouraging me in stressful times.

I would like to thank my mother **Gerti Hölzinger** for her trust in my abilities.

I would like to thank my father **Hans Wälzlein**, who passed away before I even started this thesis, for encouraging my interest in science.

I would like to thank **HGS-HIRE** for the travel support which allowed me to visit two international conferences.



---

# Erklärung zur Dissertation

Hiermit versichere ich, die vorliegende Dissertation ohne Hilfe Dritter nur mit den angegebenen Quellen und Hilfsmitteln angefertigt zu haben. Alle Stellen, die aus Quellen entnommen wurden, sind als solche kenntlich gemacht. Diese Arbeit hat in gleicher oder ähnlicher Form noch keiner Prüfungsbehörde vorgelegen.

Darmstadt, den 15.10.2013

---

(Cathrin Gabriele Wälzlein)